Orbital Evolution and Stability of Relativistic Multi-Body Systems

相対論的な多体系の軌道進化及び安定性

February 2021

Haruka SUZUKI

鈴木　遼

Orbital Evolution and Stability of Relativistic Multi-Body Systems

相対論的な多体系の軌道進化及び安定性

February 2021

Waseda University
Graduate School of Advanced Science and Engineering
Department of Pure and Applied Physics,
Research on Theoretical Astrophysics

Haruka SUZUKI

鈴木　遼

Abstract

Stellar dynamics is one of the oldest research topics of mechanics. In Newtonian mechanics, it was proved by Poincaré that systems with more than three components have no general solution. The complicated evolutions of the motion in such multi-body systems have been discussed with the analytical mechanics and the numerical simulations, and many interesting features have been explored so far.

In the 20th century, Einstein advocated general relativity, which revealed that Newtonian mechanics is just the weak-gravity limit of the theory. This means that Newtonian mechanics does not work fine for the systems with a strong gravitational field, e.g., the systems that have compact objects like black holes, neutron stars, and white dwarfs as their components in tight orbits. Stellar dynamics in such relativistic multi-body systems should be discussed with general relativity, but several interesting topics have been discussed only with Newtonian mechanics and remaining to be discussed in the relativistic regime. In order to expand such Newtonian discussions to relativistic ones, I use a post-Newtonian approximation to consider the relativistic effects as the correction terms for the Newtonian equations and calculated stellar dynamics in relativistic multi-body systems. In this thesis, I summarize two kinds of research about the von Zeipel-Lidov-Kozai (ZLK) mechanism and the Hill stability problem in a general relativistic regime.

First, I focus on the ZLK mechanism. It is one of the most interesting orbital resonances seen in hierarchical triple systems and characterized by the secular oscillations of the inner eccentricity and the relative inclination between the inner and outer orbits. The excitation of the inner eccentricity enhances the emission of the gravitational waves at the periastron point of the inner orbit. I found this enhancement of the gravitational wave emission causes the bending of the cumulative shift of the periastron time (CSPT), which can be observed if the system has a pulsar as a component of the inner binary. It has been calculated only for the isolated binary so far and is calculated for three-body systems for the first time in this research. If such an interesting evolution of the CSPT is detected through radio observation, it will be the first indirect observation of the gravitational waves from a triple system. A variety of models with a pulsar is analyzed and the parameter space where the bending of the CSPT curve can be observed on an appropriate timescale is also explored. In addition, I compare the orbital evolutions obtained by two different calculation methods: one is the direct integration of the equations of motion and the other one is the so-called double-averaging method. The latter one has been commonly used in the studies of the ZLK mechanism but some authors pointed out its accuracy problem appearing when highly eccentric orbits are calculated. Through the comparison of these two methods, I confirm the deviations between the two

methods and stress the importance of the direct integration for the studies of the ZLK mechanism.

Second, I study the relativistic effects on the stability problems focusing on Hill stability. It is the stability of a multi-body system against a close approach of one orbit to another. In Newtonian mechanics, the sufficient condition for this stability was obtained analytically only for three-body systems. I expand the sufficient condition of the Hill stability to the general relativistic regime by using the post-Newtonian approximation. In this research, as a first step, only the first-order post-Newtonian approximation is considered and several approximations are imposed for simplicity, for example, the limited configurations that the central object is much heavier than the two orbiting objects. The validity and usefulness of so-obtained approximated sufficient conditions are confirmed by numerical simulations for several models that have massive black holes as their central objects. I found that the relativistic effect makes the system more unstable than calculated in Newtonian mechanics in the sense of Hill stability as expected by the theoretical prediction. The approximated criterion will be useful to estimate the stability of the relativistic three-body systems before conducting costly numerical simulations.

Contents

Chapter 1

Introduction

The research of stellar dynamics has a long history. It started from the discovery of Kepler's laws of planetary motion in the 16th century, which were completely explained by Newtonian mechanics in the 17th century. In Newtonian mechanics, the stellar dynamics is described with the equations of motion. One can obtain general solutions of the equations of motion for two-body systems where only the gravitational force works. For systems with more than three components, however, it was proved that the equations of motion have no general solution (Poincaré, 1890) and the complicated evolutions of the motion in many-body systems have been discussed by many researchers for a long time.

Many interesting features of the evolution of the multi-body systems have been explored in Newtonian mechanics: for example, some special solutions like Lagrange collinear and equilateral triangle solutions (see e.g. Murray and Dermott (2000)) and figure-eight solutions (Moore, 1993; Chenciner and Montgomery, 2000) were obtained; various orbital resonances like the mean motion resonances (see e.g. Murray and Dermott (2000); Morbidelli (2011)) and the von Zeipel-Lidov-Kozai (ZLK) mechanism (von Zeipel, 1910; Lidov, 1962; Kozai, 1962; Naoz, 2016; Shevchenko, 2017) were also discovered; another important example is the stability problems (e.g. Marchal and Bozis (1982); Eggleton and Kiseleva (1995); Mardling and Aarseth (2001); Deck et al. (2013); Petrovich (2015)), which have been discussed by both the theoretical and numerical approaches.

In the 20th century, Einstein advocated general relativity, which revealed that Newtonian mechanics is just the weak-gravity limit of general relativity. It was confirmed that the relativistic effects appear on the orbital evolution by the observation of the periastron shift of Mercury's orbit (see e.g. Weinberg (1972); Soffel (1989); Will (2006)). Then some discussions about the stellar dynamics were expanded to take into account the relativistic effects by using so-called post-Newtonian approximations: for example, some special solutions were obtained under the first-order post-Newtonian approximation (Imai et al., 2007; Yamada and Asada, 2010; Ichita et al., 2011); the ZLK mechanism was discussed under the relativistic corrections (Blaes et al., 2002; Naoz et al., 2013b; Naoz, 2016; Shevchenko, 2017; Liu and Lai, 2017; Liu et al., 2019; Fang and Huang, 2019; Fang et al., 2019) and a new orbital resonance due to the relativistic effects was also found (Seto, 2012, 2013; Iwasa and Seto, 2017). Recently, due to the successful observations of the gravitational waves,

stellar dynamics in a strong gravitational field is attracting more and more attention from researchers.

There are many remaining subjects about the stellar dynamics of the relativistic multi-body systems. One important problem is the formulation of the evolution equations. Many studies employed the so-called double-averaging method to calculate the secular evolutions of systems (e.g. Ford et al. (2000); Blaes et al. (2002); Naoz et al. (2011, 2013b); Rafikov (2014); Liu and Lai (2017); Liu et al. (2019)), but some problems about the accuracy of this method were pointed out by several authors (Will, 2014a,b; Luo et al., 2016). Another problem is that some interesting phenomena have not been discussed in general relativity yet. Especially, the stability problems were not discussed enough in general relativity because the main target of such studies in the 20th century was the planetary systems where the gravitational field is weak enough to be treated in Newtonian mechanics.

This thesis intends to tackle these important problems and aims to contribute to understanding the dynamics of relativistic multi-body systems. In this chapter, as a preparation, I review some basic equations of the dynamics of the multi-body systems. First, I introduce some definitions and equations established in Newtonian mechanics. Then I show the formulation of the relativistic corrections by using the post-Newtonian approximations. In the last part of this chapter, I briefly introduce the main topics in this thesis.

1.1   Basic Equations of Newtonian Stellar Dynamics

The stellar dynamics have been deeply studied mainly in Newtonian mechanics. In this section, I summarize some basic definitions and equations improved to discuss stellar dynamics in Newtonian mechanics. The contents in this section are also described in detail in, for example, Murray and Dermott (2000); Morbidelli (2011); Shevchenko (2017).

1.1.1   Kepler Elements

It is well known that the relative motions in two-body systems are classified into three types: elliptic, parabolic, and hyperbolic trajectories. These trajectories are characterized by six constants called orbital elements. They correspond to six integration constants necessary to solve the equations of motion. Two elements are used to fix the orbital shape, other two elements fix the orbital plane, one determines the direction of the orbit, and the other one shows the position at an arbitrary time. In this thesis, I use the Kepler elements, which are one of the most common sets of orbital elements describing the elliptical orbits: semi-major axis a, eccentricity e, inclination i, the argument of periastron ω, the longitude of ascending node Ω, and mean anomaly M.

These elements except the mean anomaly are defined by the conserved quantities of two-body systems: the specific energy E, the specific angular momentum $\boldsymbol{h}$ and

the eccentric vector $\boldsymbol{e}$. The conserved quantities are described as

$$E = \frac{1}{2}v^2 - \frac{G(m_1 + m_2)}{r}, \tag{1.1}$$

$$\boldsymbol{h} = \boldsymbol{r} \times \boldsymbol{v}, \tag{1.2}$$

$$\boldsymbol{e} = -\frac{\boldsymbol{h} \times \boldsymbol{v}}{G(m_1 + m_2)} - \frac{\boldsymbol{r}}{r}, \tag{1.3}$$

where m_1 and m_2 are the stellar masses of star 1 and 2, respectively, and $\boldsymbol{r}$ and $\boldsymbol{v}$ are the relative motion and velocity vectors of star 2 seen from star 1. The description of the eccentric vector Eq. (1.3) can be derived by integrating the equation of motion multiplied by the specific angular momentum.

The inner product of the specific angular momentum $\boldsymbol{h}$ and the eccentric vector $\boldsymbol{e}$ is zero, which means the eccentric vector $\boldsymbol{e}$ exists on the orbital plane spanned by $\boldsymbol{r}$ and $\boldsymbol{v}$. The magnitude of the eccentric vector $e = |\boldsymbol{e}|$ is defined as the eccentricity. The square of Eq. (1.3) describes the eccentricity by E and h as

$$e^2 = 1 + \frac{2h^2 E}{G^2(m_1 + m_2)^2}. \tag{1.4}$$

The eccentricity determines the type of the trajectory of the two-body motion: the elliptic orbit has $0 \le e < 1$, the parabolic one has $e = 1$, and the hyperbolic orbit has $e > 1$.

Here I focus on elliptic orbits, i.e., $0 \le e < 1$. In this case, the magnitude of the relative position vector r can be described with the eccentricity e by calculating the inner product of $\boldsymbol{r}$ and Eq. (1.3) as

$$r = \frac{h^2}{G(m_1 + m_2)(1 + e \cos f)}, \tag{1.5}$$

where f is the angle between $\boldsymbol{r}$ and $\boldsymbol{e}$ called a true anomaly. Eq. (1.5) with $0 \le e < 1$ gives the configuration as in Fig. 1.1. One can find that r becomes a minimum when $f = 0$ in Eq. (1.5). It means that the eccentric vector is directed to the periastron point, where the distance between the two stars is closest. Star 1 is on the focus of the elliptic orbit with the semi-major axis $a = h^2/\{G(m_1 + m_2)(1 - e^2)\}$. The semi-major axis can be expressed with the specific orbital energy by using Eqs. (1.1) and (1.3) as

$$a = -\frac{G(m_1 + m_2)}{2E}. \tag{1.6}$$

The eccentricity and semi-major axis that are defined above fix the shape of the orbit. Next, I show the definitions of the two orbital elements that determine the orbital plane: the inclination i and the longitude of the ascending node Ω. The inclination i is the angle between the orbital plane and the reference plane. Defining the reference coordinates as (X, Y, Z) and the reference plane as the X-Y plane, the inclination is described as

$$\cos i = \frac{h_Z}{h}. \tag{1.7}$$
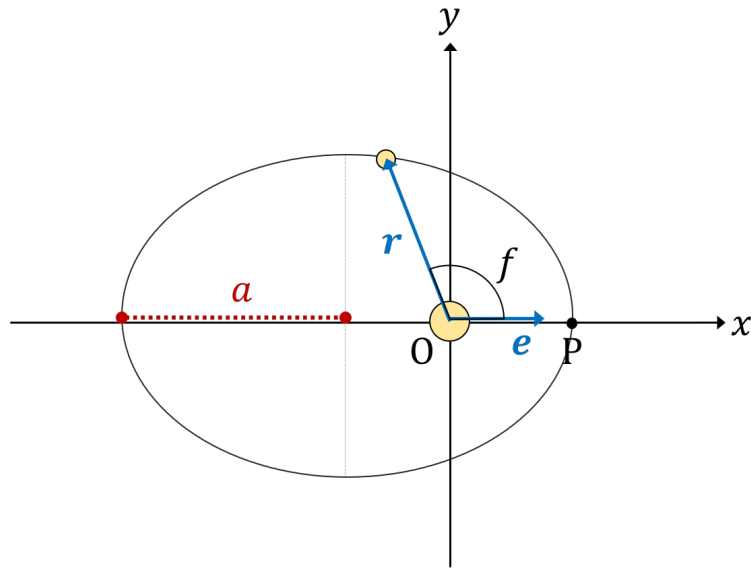
Figure 1.1: An example of the elliptical orbit. Star 1 is on the focus of the elliptic orbit. The coordinates are defined as $x = r \cos f$ and $y = \sin f$. The eccentric vector is directed to the periastron shown as the point P. Detail explanation is in the text.
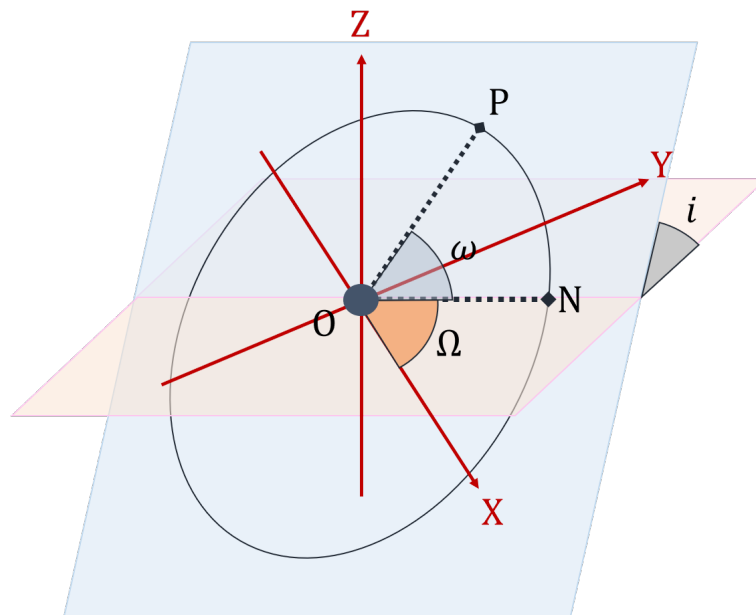
Figure 1.2: An example of the orbital configuration in a three-dimensional reference frame. The axes X, Y, and Z describe the reference coordinates whose origin O is on the star 1. The orange and blue planes are the reference and orbital planes. The orbital periastron and ascending node are described as P and N. The inclination, longitude of the ascending node, and argument of periastron are shown as i, Ω and ω. Detail explanation is in the text.

The longitude of the ascending node Ω is the angle between the X-axis and the ascending node on the reference plane. The ascending node is the point where the orbit crosses the reference plane from $Z < 0$ to $Z > 0$. The configuration is shown in Fig. 1.2. The vector from the primary star to the ascending node $\overrightarrow{ON}$ is directed to $\boldsymbol{\epsilon}_Z \times \boldsymbol{h}$, where $\boldsymbol{\epsilon}_Z$ is the unit vector in the Z-direction. With this relation, the longitude of the ascending node Ω is described as

$$\cos\Omega = \frac{(\boldsymbol{\epsilon}_Z \times \boldsymbol{h})_X}{|\boldsymbol{\epsilon}_Z \times \boldsymbol{h}|}, \tag{1.8}$$

where $(\boldsymbol{\epsilon}_Z \times \boldsymbol{h})_X$ means the X-component of the vector.

The direction of the orbit on the orbital plane is determined by the argument of periastron ω. It is defined as the angle between the directions of the ascending node $\overrightarrow{ON}$ and the periastron $\overrightarrow{OP}$ (see Fig. 1.2), so $\cos\omega = (\overrightarrow{ON}/|\overrightarrow{ON}|) \cdot (\overrightarrow{OP}/|\overrightarrow{OP}|)$. As in the Figs. 1.1 and 1.2, $\overrightarrow{OP}$ and $\overrightarrow{ON}$ can be replaced by $\boldsymbol{e}$ and $\boldsymbol{\epsilon}_Z \times \boldsymbol{h}$, respectively, and the description becomes as

$$\cos\omega = \frac{\boldsymbol{e}}{e} \cdot \frac{(\boldsymbol{\epsilon}_Z \times \boldsymbol{h})}{|\boldsymbol{\epsilon}_Z \times \boldsymbol{h}|}. \tag{1.9}$$

The remaining one element, the mean anomaly M, describes the position of the star at an arbitrary time. The mean anomaly M is proportional to time and can be described as $M = n(t - t_0)$, where $n = \sqrt{G(m_1 + m_2)/a^3}$ is the angular velocity called the mean motion, and t_0 is arbitrary time. This value is indirectly related to the true anomaly f. Here I introduce another parameter u called an eccentric anomaly. It is defined as the angle between $\overrightarrow{O'P}$ and $\overrightarrow{O'Q'}$ in Fig. 1.3. The points O' is the center of the circle osculating the elliptic orbit at the periastron and apoastron points and Q' is the position of the orbiting star projected to the circle. The coordinates of the point Q is described as

$$x = r\cos f = \frac{a(1 - e^2)\cos f}{1 + e\cos f} = -ae + a\cos u, \tag{1.10}$$

$$y = r\sin f = \frac{a(1 - e^2)\sin f}{1 + e\cos f} = a\sqrt{1 - e^2}\sin u. \tag{1.11}$$

The time derivative of u is given by $du/dt = (dr/dt)(du/dr)$. The first part dr/dt is derived by the vector product of Eq. (1.3) and $\boldsymbol{r}$ as

$$\frac{dr}{dt} = \frac{G(m_1 + m_2)e}{h}\sin f = \frac{G(m_1 + m_2)e}{h}\frac{\sqrt{1 - e^2}\sin u}{1 - e\cos u}. \tag{1.12}$$

The second part du/dr is calculated as

$$\frac{du}{dr} = \left(\frac{dr}{du}\right)^{-1} = \frac{1}{ae\sin u}. \tag{1.13}$$

By using these equations, the time derivative of u is described as

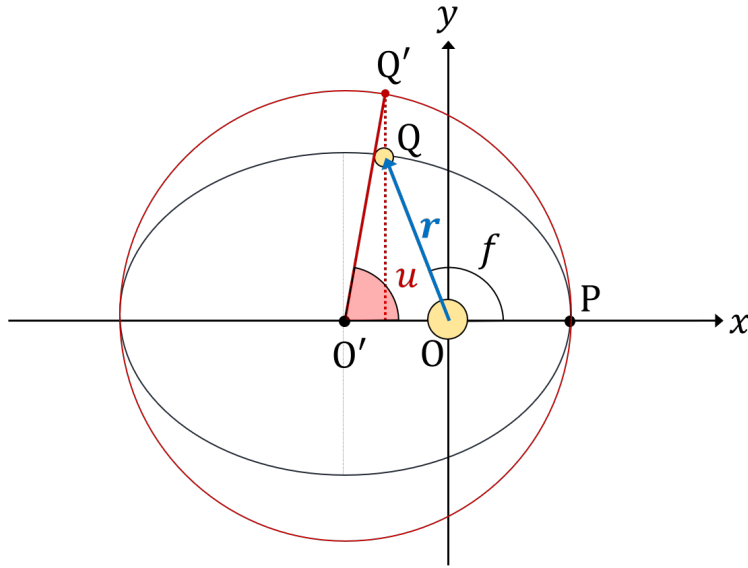$$\frac{du}{dt} = \frac{G(m_1 + m_2)}{ah}\frac{\sqrt{1 - e^2}}{1 - e\cos u} = \frac{n}{1 - e\cos u}. \tag{1.14}$$

Figure 1.3:   The definition of the eccentric anomaly u. The points O' is the center of the circle osculating the elliptic orbit at the periastron and apoastron points and Q' is the position of the orbiting star projected to the circle. Details are explained in the text.

The integration of this equation describes the mean anomaly with the eccentric anomaly u as

$$M = u - e \sin u. \tag{1.15}$$

These six orbital elements fix the relative motion of the two-body system in the elliptic orbit.

Note that the Kepler elements are related with so-called Delauney's variables, which are the canonical variables of the Hamiltonian of the two-body relative motion (see Appendix A). Delaunay's variables are classified as the action-angle variables that are used to approach the stellar dynamics from the viewpoint of Hamiltonian mechanics. I do not use the Hamiltonian approach in this thesis, but I remark that it played a quite important role in the progress of the understanding of the orbital resonances (see e.g. Arnold (1989); Murray and Dermott (2000); Morbidelli (2011)).

1.1.2   Lagrange Planetary Equations

If a system has three or more objects, the motions of the components are not exact elliptical orbits even if they are bounded in the system. However, if the forces other than two-body gravitational interaction is small enough to be treated as the perturbation, the motions can be approximated to the elliptical orbits that change their shape gradually. It is convenient to introduce *osculating orbits*, which is defined as the elliptical orbits coming in contact with the instantaneous motions. The evolutions of the motions in the perturbed systems can be intuitively understood by calculating the evolutionary equations of the osculating orbital elements instead of the equations of motion. I introduce the derivation of such evolutionary equations of the osculating orbital elements called Lagrange planetary equations.

The relative positions r_i and velocities v_i ($i = 1$ to 3) can be described as the functions of the osculating orbital elements $c_j(t)$ ($j = 1$ to 6) and the time t, that is, $r_i = r_i(c_j(t), t)$ and $v_i = v_i(c_j(t), t)$. By using these relations, the time derivative of the positions and velocities are written as

$$\frac{dr_i}{dt} = \frac{\partial r_i}{\partial t} + \sum_{j=1}^{6} \frac{\partial r_i}{\partial c_j}\frac{dc_j}{dt}, \tag{1.16}$$

$$\frac{dv_i}{dt} = \frac{\partial v_i}{\partial t} + \sum_{j=1}^{6} \frac{\partial v_i}{\partial c_j}\frac{dc_j}{dt}. \tag{1.17}$$

On the other hand, from the equations of motion, the time derivatives are written as

$$\frac{dr_i}{dt} = v_i, \tag{1.18}$$

$$\frac{dv_i}{dt} = -\frac{G(m_1 + m_2)}{r} + \frac{\partial V}{\partial r_i}, \tag{1.19}$$

where V is the potential corresponding to the perturbation like the gravitational potential from the objects orbiting distant region. These descriptions give the following equations:

$$\sum_{j=1}^{6} \frac{\partial r_i}{\partial c_j}\frac{dc_j}{dt} = 0, \tag{1.20}$$

$$\sum_{j=1}^{6} \frac{\partial v_i}{\partial c_j}\frac{dc_j}{dt} = \frac{\partial V}{\partial r_i}. \tag{1.21}$$

By multiplying $\partial r_i/\partial c_l$ and $\partial v_i/\partial c_l$ ($l = 1$ to 6) to the former and latter equations, respectively, subtracting the latter from former ones, and then summing them up about i, I obtain

$$\sum_{j=1}^{6} [c_l, c_j]\frac{dc_j}{dt} = \frac{\partial V}{\partial c_l}, \tag{1.22}$$

where $[c_l, c_j]$ is Lagrange brackets, which is defined as

$$[c_l, c_j] \equiv \sum_{i=1}^{3} \left(\frac{\partial r_i}{\partial c_l}\frac{\partial v_i}{\partial c_j} - \frac{\partial r_i}{\partial c_j}\frac{\partial v_i}{\partial c_l} \right). \tag{1.23}$$

By using the definition of the Kepler elements in §1.1.1, the Lagrange brackets are

calculated as

$$[M, a] = \frac{1}{2}an, \tag{1.24}$$

$$[a, \Omega] = -\frac{1}{2}an\sqrt{1 - e^2}\cos i, \tag{1.25}$$

$$[a, \omega] = -\frac{1}{2}an, \tag{1.26}$$

$$[e, \Omega] = \frac{a^2 ne}{\sqrt{1 - e^2}}\cos i, \tag{1.27}$$

$$[e, \omega] = \frac{a^2 ne}{\sqrt{1 - e^2}}, \tag{1.28}$$

$$[\Omega, i] = -a^2 n\sqrt{a - e^2}\sin i. \tag{1.29}$$

The Lagrange brackets other than the above six just vanish. The Lagrange planetary equations for the Kepler elements are derived by substituting the Lagrange brackets into Eq. (1.22) and multiplying the inverse matrix:

$$\frac{da}{dt} = \frac{2}{an}\frac{\partial V}{\partial M}, \tag{1.30}$$

$$\frac{de}{dt} = \frac{1 - e^2}{a^2 ne}\frac{\partial V}{\partial M} - \frac{\sqrt{1 - e^2}}{a^2 ne}\frac{\partial V}{\partial \omega}, \tag{1.31}$$

$$\frac{di}{dt} = \frac{\cot i}{a^2 n\sqrt{1 - e^2}}\frac{\partial V}{\partial \omega} - \frac{1}{a^2 n\sqrt{1 - e^2}\sin i}\frac{\partial V}{\partial \Omega}, \tag{1.32}$$

$$\frac{d\omega}{dt} = \frac{\sqrt{1 - e^2}}{a^2 ne}\frac{\partial V}{\partial e} - \frac{\cot i}{a^2 n\sqrt{1 - e^2}}\frac{\partial V}{\partial i}, \tag{1.33}$$

$$\frac{d\Omega}{dt} = \frac{1}{a^2 n\sqrt{1 - e^2}\sin i}\frac{\partial V}{\partial i}, \tag{1.34}$$

$$\frac{dM}{dt} = -\frac{2}{an}\frac{\partial V}{\partial a} - \frac{1 - e^2}{a^2 ne}\frac{\partial V}{\partial e}. \tag{1.35}$$

1.1.3   Double-Averaging Method

In the systems where the forces other than two-body gravitational force is small enough to be treated as the perturbation, some interesting behaviors in the orbital evolutions are obtained on a secular timescale much longer than the orbital periods. In order to extract such secular evolutions from the Lagrange planetary equations, it is convenient to take the average of the equations over all the orbital periods in the system. This method is commonly used to calculate the orbital evolutions of the multi-body systems where the interaction between the orbiting objects can be treated as the perturbation: one example is hierarchical triple systems, where the third body is orbiting far from the inner binary; another example is the planetary-like systems, where the masses of the orbiting objects are much smaller than that of the central object.

Here I introduce the basic equations of the double-averaging method derived for so-called restricted triple systems. This is a kind of hierarchical triple systems that have one test particle as a component of its inner binary. A schematic picture of
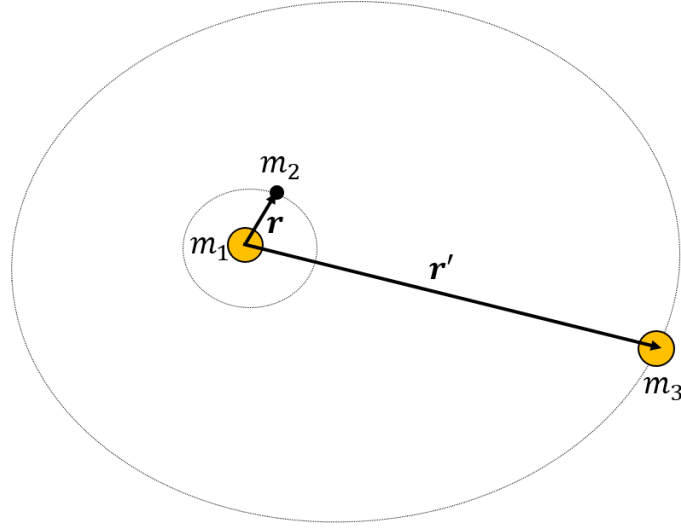
Figure 1.4: A schematic picture of a restricted triple system. The relative position vectors from star 1 to 2 and 1 to 3 are described as $\boldsymbol{r}$ and $\boldsymbol{r}'$, respectively. The outer distance r' is assumed to be much longer than the inner one r. The masses of the three stars as m_i ($i = 1$ to 3) and m_2 is assumed to be much smaller than the other masses.

the system is in Fig. 1.4. The masses of the stars are denoted as m_i ($i = 1$ to 3) and the relative motion of the inner and outer orbits are described as $\boldsymbol{r}$ and $\boldsymbol{r}'$, respectively. In the restricted triple system, I assume $r \ll r'$ and $m_2 \ll m_1, m_3$. With these assumptions, the gravitational force from the inner to outer orbits is negligibly small, which means the outer orbit is almost unchanged. Therefore, I focus on the evolution of the inner orbit in this subsection. Note that the double-averaging method for the hierarchical triple system with massive m_2 was given in Naoz et al. (2013a), where several different evolutions from the restricted triple systems are observed. This point is discussed again in Chapter 2.

The equations of motion of the relative position $\boldsymbol{r}$ are written as

$$\frac{d^2\boldsymbol{r}}{dt^2} = -G(m_1 + m_2)\frac{\boldsymbol{r}}{r^3} - Gm_3 \left(\frac{\boldsymbol{r} - \boldsymbol{r}'}{|\boldsymbol{r} - \boldsymbol{r}'|^3} + \frac{\boldsymbol{r}'}{r'^3} \right). \tag{1.36}$$

The latter term in Eq. (1.36) can be described with a potential V as $\partial V/\partial \boldsymbol{r}$, where the potential V is defined as

$$V \equiv Gm_3 \left(\frac{1}{|\boldsymbol{r} - \boldsymbol{r}'|} - \frac{\boldsymbol{r} \cdot \boldsymbol{r}'}{r'^3} \right). \tag{1.37}$$

This potential V is sometimes called the perturbation function. When the angle between $\boldsymbol{r}$ and $\boldsymbol{r}'$ is defined as S, $1/|\boldsymbol{r} - \boldsymbol{r}'|$ in the potential is rewritten as

$$\frac{1}{|\boldsymbol{r} - \boldsymbol{r}'|} = \frac{1}{r'} \left\{ 1 + \left(\frac{r}{r'} \right)^2 - 2\frac{r}{r'} \cos S \right\}^{-\frac{1}{2}}. \tag{1.38}$$

The right-hand side of this equation corresponds to the generating function of the Legendre polynomial $P_n(\cos S)$, which is expanded with the Legendre polynomials

as

$$\frac{1}{|\boldsymbol{r} - \boldsymbol{r'}|} = \frac{1}{r'} \sum_{n=0}^{\infty} \mathrm{P}_n(\cos S) \left(\frac{r}{r'}\right)^n, \tag{1.39}$$

where the Legendre polynomial is defined as

$$\mathrm{P}_n(x) \equiv \frac{1}{2^n n!} \frac{d^n}{dx^n} (x^2 - 1)^n. \tag{1.40}$$

By substituting Eqs. (1.39) and (1.40) into Eq. (1.37), the perturbation function is rewritten as

$$V = Gm_3 \frac{1}{r'} \left\{ 1 - \left(-\frac{1}{2} + \frac{3}{2}\cos^2 S\right) \left(\frac{r}{r'}\right)^2 \right\} + \mathcal{O}\left(\left(\frac{r}{r'}\right)^3\right). \tag{1.41}$$

I explicitly write down the expansion up to quadrupole order. I neglect higher-order terms in this section. Note that some secular behaviors appear in the calculation with the double-averaging method only when the higher-order terms are considered, for example, orbital flip in the ZLK mechanism (Naoz, 2016). We revisit this point in Chapter 2.

The perturbation function V can be divided into two parts: one is the periodic part V_p, which changes on inner and outer periods, and the other one is the secular part V_s, which changes on a secular timescale. In order to extract V_s from V, the average of V over the inner and outer periods are calculated. The orbital average is calculated as

$$\frac{1}{P} \int_0^P dt = \frac{1}{2\pi} \int_0^{2\pi} dM, \tag{1.42}$$

where P is the orbital period. I describe this orbital average as $\langle \ \rangle_{M_\mathrm{in}}$ and $\langle \ \rangle_{M_\mathrm{out}}$ for the inner and outer orbits. The subscripts in and out mean the orbital elements of the inner and outer orbits, respectively. The secular potential V_s is calculated as

$$
\begin{aligned}
V_\mathrm{s} &= \langle\langle V \rangle_{M_\mathrm{in}}\rangle_{M_\mathrm{out}} \\
&= \frac{Gm_3 a_\mathrm{in}^2}{a_\mathrm{out}^3} \Bigg[-\frac{1}{2} \left\langle \left(\frac{r}{a_\mathrm{in}}\right)^2 \right\rangle_{M_\mathrm{in}} \left\langle \left(\frac{a_\mathrm{out}}{r'}\right)^3 \right\rangle_{M_\mathrm{out}} \\
&\quad + \frac{3}{2} \left\langle \left(\frac{r}{a_\mathrm{in}}\right)^2 \left\langle \left(\frac{a_\mathrm{out}}{r'}\right)^3 \cos^2 S \right\rangle_{M_\mathrm{out}} \right\rangle_{M_\mathrm{in}} \Bigg].
\end{aligned}
\tag{1.43}
$$

In this calculation, the orbital elements except the mean anomalies are assumed not to change for one orbital cycle. The distances r and r' are described with orbital elements by using Eqs. (1.10) and (1.11). The eccentric anomaly is related to the mean anomaly as Eq. (1.15), which is used to calculate the orbital average as in Eq. (1.42).

The angle S in Eq. (1.43) can be rewritten with the orbital elements by using spherical trigonometry. In spherical trigonometry, the angle on a sphere is defined by the inner product of the normal vectors of two planes on both sides of the angle. For example, in Fig. 1.5, the angle α on a unit sphere is defined as
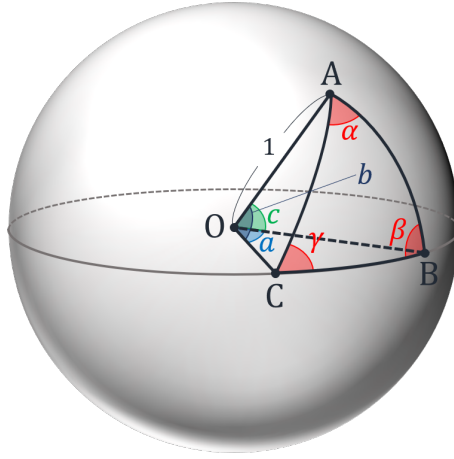
Figure 1.5: A unit sphere to explain spherical trigonometry. The angles α, β, and γ are on the spherical plane. The angles between OB and OC, OC and OA, and OA and OB are defined as a, b and c, respectively.

$$\cos \alpha \equiv \frac{\overrightarrow{OA} \times \overrightarrow{OC}}{\left| \overrightarrow{OA} \times \overrightarrow{OC} \right|} \cdot \frac{\overrightarrow{OA} \times \overrightarrow{OB}}{\left| \overrightarrow{OA} \times \overrightarrow{OB} \right|} \tag{1.44}$$

By using the angles a, b and c in Fig. 1.5, the denominator and numerator on the right-hand side of this equation can be calculated as

$$\left| \overrightarrow{OA} \times \overrightarrow{OB} \right| = \left| \overrightarrow{OA} \right| \left| \overrightarrow{OB} \right| \sin c = \sin c, \tag{1.45}$$

$$\left| \overrightarrow{OA} \times \overrightarrow{OC} \right| = \left| \overrightarrow{OA} \right| \left| \overrightarrow{OC} \right| \sin b = \sin b, \tag{1.46}$$

$$
\begin{aligned}
\left(\overrightarrow{OA} \times \overrightarrow{OC} \right) \cdot \left(\overrightarrow{OA} \times \overrightarrow{OB} \right) &= \left\{ \left(\overrightarrow{OA} \times \overrightarrow{OC} \right) \times \overrightarrow{OA} \right\} \cdot \overrightarrow{OB} \\
&= \left\{ \left(\overrightarrow{OA} \cdot \overrightarrow{OA} \right) \overrightarrow{OC} - \left(\overrightarrow{OC} \cdot \overrightarrow{OA} \right) \overrightarrow{OA} \right\} \cdot \overrightarrow{OB} \\
&= \cos a - \cos b \cos c. \tag{1.47}
\end{aligned}
$$

These definitions and relations give the cosine theory of the spherical trigonometric as

$$\cos \alpha = \frac{\cos a - \cos b \cos c}{\sin b \sin c}, \tag{1.48}$$

$$\cos \beta = \frac{\cos b - \cos c \cos a}{\sin c \sin a}, \tag{1.49}$$

$$\cos \gamma = \frac{\cos c - \cos a \cos b}{\sin a \sin b}. \tag{1.50}$$

This cosine theory can be applied to the restricted triple system. From the schematic picture is in Fig. 1.6, the relative inclination between inner and outer orbits I can be written with the other angles as

$$\cos I = \frac{\cos S - \cos \left(f_{\text{out}} - \Omega_{\text{in}} \right) \cos \left(\omega_{\text{in}} + f_{\text{in}} \right)}{\sin \left(f_{\text{out}} - \Omega_{\text{in}} \right) \sin \left(\omega_{\text{in}} + f_{\text{in}} \right)}, \tag{1.51}$$
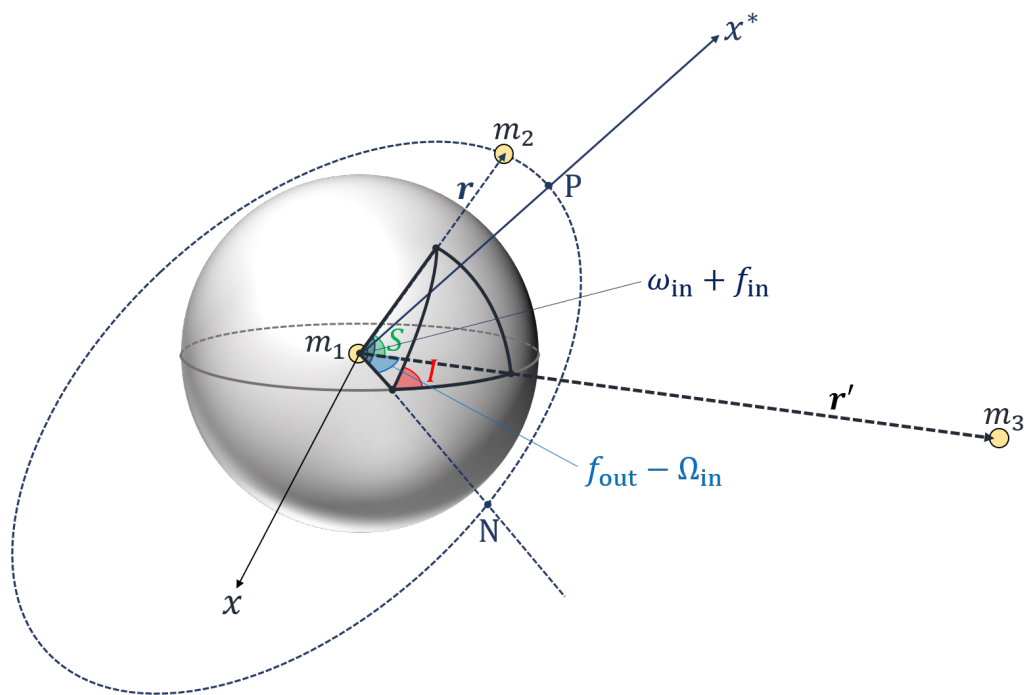
Figure 1.6:   A schematic picture of the configuration of a restricted triple system. A unit sphere is also drawn to apply the spherical trigonometric to the system. The angles used in the cosine theorem are written with some orbital elements defined in subsection 1.1.1. The elliptic shape drawn with a dashed line corresponds to the inner orbit. The points P and N are the orbital periastron and the ascending node. The x- and x^*-axes are directed to the periastron points of outer and inner orbit, respectively. The outer orbital plane is defined as the reference plane and assumed not to change due to small gravitational force from the inner orbit.

and this gives the description of the angle S as

$$\cos S = \cos I \sin\left(f_{\text{out}} - \Omega_{\text{in}}\right) \sin\left(\omega_{\text{in}} + f_{\text{in}}\right) + \cos\left(f_{\text{out}} - \Omega_{\text{in}}\right) \cos\left(\omega_{\text{in}} + f_{\text{in}}\right). \quad (1.52)$$

Note that in Fig. 1.6, the reference plane (x-y plane) is defined as the outer orbital plane because the effect of gravitational force from the inner orbit to the outer one is negligible in the restricted triple system and the outer orbital plane does not move in the orbital evolution. In such configuration, the relative inclination I just corresponds to the inner inclination i_{in}. In general, the relative inclination is written with the inclinations and the longitudes of ascending nodes as

$$\cos I = \cos i_{\text{in}} \cos i_{\text{out}} + \sin i_{\text{in}} \sin i_{\text{out}} \cos\left(\Omega_{\text{in}} - \Omega_{\text{out}}\right). \quad (1.53)$$

Now Eq. (1.43) can be calculated by using Eqs. (1.10), (1.11), (1.15), and (1.52) as

$$V_{\text{s}} = \frac{Gm_3 a_{\text{in}}^2}{a_{\text{out}}{}^3 (1 - e_{\text{out}}^2)^{\frac{3}{2}}} \left[\frac{1}{8}\left(1 + \frac{3}{2}e_{\text{in}}^2\right)\left(3\cos^2 I - 1\right) + \frac{15}{16}e_{\text{in}}^2 \cos 2\omega_{\text{in}} \sin^2 I \right]. \quad (1.54)$$

When V in the Lagrange planetary equations (1.30)-(1.35) is replaced by V_{s}, the equations for secular evolution are derived as

$$\frac{da_{\text{in}}}{dt} = 0, \quad (1.55)$$

$$\frac{de_{\text{in}}}{dt} = -\frac{\sqrt{1 - e_{\text{in}}^2}}{a_{\text{in}}^2 n_{\text{in}} e_{\text{in}}}\frac{\partial V_{\text{s}}}{\partial \omega_{\text{in}}}, \quad (1.56)$$

$$\frac{dI}{dt} = \frac{\cot I}{a_{\text{in}}^2 n_{\text{in}} \sqrt{1 - e_{\text{in}}^2}}\frac{\partial V_{\text{s}}}{\partial \omega_{\text{in}}} \quad (1.57)$$

$$\frac{d\omega_{\text{in}}}{dt} = \frac{\sqrt{1 - e_{\text{in}}^2}}{a_{\text{in}}^2 n_{\text{in}} e_{\text{in}}}\frac{\partial V_{\text{s}}}{\partial e_{\text{in}}} - \frac{\cot I}{a_{\text{in}}^2 n_{\text{in}} \sqrt{1 - e_{\text{in}}^2}}\frac{\partial V_{\text{s}}}{\partial I}, \quad (1.58)$$

$$\frac{d\Omega_{\text{in}}}{dt} = \frac{1}{a_{\text{in}}^2 n_{\text{in}} \sqrt{1 - e_{\text{in}}^2} \sin I}\frac{\partial V_{\text{s}}}{\partial I}. \quad (1.59)$$

Interestingly, from Eq. (1.55), one can find that the inner semi-major axis does not evolve on a secular timescale for the restricted triple systems.

1.2 Post-Newtonian Approximation

The Newtonian basic equations introduced in § 1.1 work well in planetary systems or star-planet-satellite systems. However, if some objects are orbiting in the vicinity of a star, sometimes the gravitational field is strong enough that the effects of the general relativity can be seen in their orbital evolutions. For example, it is well known that the orbit of Mercury shows the shift of its periastron on a secular timescale, which is explained by general relativity (see e.g. Weinberg (1972); Soffel (1989); Will (2006)).

When multi-body systems have compact objects like black holes, neutron stars, or white dwarfs as their components interacting with the separations short enough,

their orbital evolutions should be calculated with general relativity because the gravitational field in such systems can be much stronger than that in the orbit of Mercury. Although one may think such relativistic multi-body systems may be quite rare, there is indeed an observed example: the PSR J0337+1715 system is a relativistic three-body system composed of a millisecond pulsar and two white dwarfs orbiting around it (Ransom et al., 2014). More relativistic multi-body systems with massive black holes are also expected to be observed by future satellite-borne gravitational-wave detectors like Laser Interferometer Space Antenna (LISA) (Hoang et al., 2019; Randall and Xianyu, 2019; Deme et al., 2020; Gupta et al., 2020) or with radio observations of pulsars (Suzuki et al., 2019, 2021), which I discuss in Chapter 2. Hence, it is important to calculate the evolutions of relativistic multi-body systems with general relativity taken into account.

In most relativistic systems except binaries just before the merger, the gravitational field cannot be treated in the Newtonian limit but is weak enough that the relativistic effects can be treated as some correction terms to Newtonian mechanics instead of calculating the full Einstein equations. I use the post-Newtonian (PN) approximation to consider the relativistic effects as the correction terms to Newtonian equations of motion in this thesis. In the PN approximation, the metric is expanded with $(v/c)^2$, where c and v are the speed of light and that of the component, respectively. This approximation can be applied only for the systems whose typical speed is much smaller than the speed of light c. I mainly use the first-order post-Newtonian (1PN) approximation in this thesis, that is, the expansion up to the fourth-order of v/c is considered. In this section, I introduce the derivation of the 1PN equations of motion called Einstein-Infeld-Hoffmann equations and discuss how to consider the relativistic corrections for the orbital evolutionary equations. Some of the higher-order PN effects are also discussed in chapters 2 and 3, later.

The notation of the general relativity in this thesis follows Weinberg (1972). Alphabetical subscripts like i, j, and k are used as the label of spatial coordinates (x, y, z) that run from 1 to 3 or used as the number of the objects in the system. On the other hand, subscripts written in Greek alphabets like μ, ν, and λ are always used as the label of four-dimensional coordinates (ct, x, y, z), and run from 0 to 3. The sign of the Minkowski metric η is $(- + + +)$ and the Einstein equations are described as $G_{\mu\nu} = -(8\pi G/c^4)T_{\mu\nu}$.

1.2.1   Einstein-Infeld-Hoffmann Equations

In the PN approximation, the relativistic effects are treated as the correction terms to the Newtonian equations of motion. The acceleration $d^2x^i/(dt^2)$ is described with the proper time τ as

$$\frac{d^2x^i}{dt^2} = \left(\frac{d\tau}{dt}\right)^2 \frac{d^2x^i}{d\tau^2} - \left(\frac{d\tau}{dt}\right)^3 \frac{d^2t}{d\tau^2}\frac{dx^i}{d\tau}. \tag{1.60}$$

The second derivatives of x^i and t by τ in this description are given by the geodesic equations, which describe the motion of the free-falling particle in the general relativity:

$$\frac{d^2x^\mu}{d\tau^2} + \Gamma^\mu_{\nu\lambda}\frac{dx^\nu}{d\tau}\frac{dx^\lambda}{d\tau} = 0, \tag{1.61}$$

where $\Gamma^{\mu}_{\nu\lambda}$ is the affine connection, which is described with the metric $g_{\mu\nu}$ as

$$\Gamma^{\mu}_{\nu\lambda} = \frac{1}{2} g^{\mu\sigma} \left(\frac{\partial g_{\sigma\nu}}{\partial x^{\lambda}} + \frac{\partial g_{\sigma\lambda}}{\partial x^{\nu}} - \frac{\partial g_{\nu\lambda}}{\partial x^{\sigma}} \right). \tag{1.62}$$

By substituting Eq.(1.61) to Eq. (1.60), the acceleration is described as

$$\begin{aligned}
\frac{d^2 x^i}{dt^2} &= -c^2 \Gamma^i_{00} - 2c\Gamma^i_{0j} \frac{dx^j}{dt} - \Gamma^i_{jk} \frac{dx^j}{dt} \frac{dx^k}{dt} \\
&+ \left[c\Gamma^0_{00} + 2\Gamma^0_{0j} \frac{dx^j}{dt} + \frac{1}{c} \Gamma^0_{jk} \frac{dx^j}{dt} \frac{dx^k}{dt} \right] \frac{dx^i}{dt}.
\end{aligned} \tag{1.63}$$

The Newtonian limit is calculated when the perturbed Minkowski metric $g_{\mu\nu} = \eta_{\mu\nu} + h_{\mu\nu}$ ($|h| \ll 1$) is used in Eq. (1.62) and the second- and higher-order terms of h in Eq. (1.63) is neglected. The Newtonian equations of motion obtained as this limit are

$$\frac{d^2 x^i}{dt^2} = \frac{1}{2} c^2 \eta^{\mu i} \frac{\partial h_{00}}{\partial x^{\mu}} = \frac{1}{2} c^2 \frac{\partial h_{00}}{\partial x^i}. \tag{1.64}$$

This means that h_{00} should be described with the Newtonian gravitational potential ϕ as $h_{00} = -2\phi/c^2$. Since $\phi \sim v^2$ from the Newtonian virial theorem, the Newtonian equations of motion is proportional to $(v/c)^2$. For the 1PN approximation, therefore, the terms up to $(v/c)^4$-order should be included in the equations of motion.

The procedure to obtain the 1PN equations of motion requires three steps: first, the metric $g_{\mu\nu}$ are expanded with v/c as $g_{\mu\nu} = \overset{0}{g}_{\mu\nu} + \overset{1}{g}_{\mu\nu} + \cdots$, where $\overset{N}{g}_{\mu\nu}$ means N-th order term, and then the affine connections $\Gamma^{\mu}_{\nu\lambda}$ and the Ricci tensor $R_{\mu\nu}$ are also expanded and described with the expanded terms of the metric $\overset{N}{g}_{\mu\nu}$; second, the Einstein equations are solved and each $\overset{N}{g}_{\mu\nu}$ is described with the components of the energy-momentum tensor; third, each expanded component of the energy-momentum tensor is explicitly written with the masses, positions, and velocities of N-body components assuming all components are the point particles. I explain these three steps subsequently and derive the 1PN equations of motion called Einstein-Infeld-Hoffmann equations. The equations were originally derived in Einstein et al. (1938) and note that it could be derived from the Lagrangian given by Lorentz and Droste (1917). The derivation processes were later explained in detail in several references (see e.g. Weinberg (1972); Misner et al. (1973); Landau and Lifschits (1975)).

Expansion of $g_{\mu\nu}$, $\Gamma^{\mu}_{\nu\lambda}$ and $R_{\mu\nu}$

As in the Newtonian limit case, the metric is considered as the perturbed Minkowski metric, that is, $g_{\mu\nu} = \eta_{\mu\nu} + h_{\mu\nu}$ ($|h| \ll 1$). All of the higher-order terms of v/c are in $h_{\mu\nu}$.

In order to expand each component of $g_{\mu\nu}$, here time-reversal transformation $t \to -t$ is considered since v/c is antisymmetric with respect to the transformation. The coordinates and the metric after the transformation are denoted as x'^{μ} and $g'_{\mu\nu}$, respectively. The transformation of the metric can be calculated as

$$g'_{\mu\nu} = g_{\lambda\sigma} \frac{\partial x^{\lambda}}{\partial x'^{\mu}} \frac{\partial x^{\sigma}}{\partial x'^{\nu}}, \tag{1.65}$$

and each component of $g'_{\mu\nu}$ is obtained as

$$
\begin{align}
g'_{00} &= g_{00}, & (1.66)\\
g'_{i0} &= -g_{i0}, & (1.67)\\
g'_{ij} &= g_{ij}. & (1.68)
\end{align}
$$

This means that the $i0$-component of $g_{\mu\nu}$ is antisymmetric with respect to the time-reversal transformation, that is, has odd-order terms of v/c, and, on the other hand, the 00- and ij-components are symmetric and have even-order terms of v/c. Hence the components of the metric are expanded with N-th order term $\overset{N}{g}_{\mu\nu}$ as

$$
\begin{align}
g_{00} &= -1 + \overset{2}{g}_{00} + \overset{4}{g}_{00} + \dots, & (1.69)\\
g_{i0} &= \overset{3}{g}_{i0} + \overset{5}{g}_{i0} + \dots, & (1.70)\\
g_{ij} &= \delta_{ij} + \overset{2}{g}_{ij} + \overset{4}{g}_{ij} + \dots, & (1.71)
\end{align}
$$

and the components of the inverse metric are also obtained as

$$
\begin{align}
g^{00} &= -1 + \overset{2}{g}{}^{00} + \overset{4}{g}{}^{00} + \dots, & (1.72)\\
g^{i0} &= \overset{3}{g}{}^{i0} + \overset{5}{g}{}^{i0} + \dots, & (1.73)\\
g^{ij} &= \delta^{ij} + \overset{2}{g}{}^{ij} + \overset{4}{g}{}^{ij} + \dots. & (1.74)
\end{align}
$$

By substituting these expansions into the relation between the metric and the inverse metric $g^{\mu\lambda}g_{\lambda\nu} = \delta^{\mu}{}_{\nu}$, we obtain

$$
\begin{align}
\overset{3}{g}{}^{i0} &= \overset{3}{g}_{i0}, & (1.75)\\
\overset{2}{g}{}^{00} &= -\overset{2}{g}_{00}, & (1.76)\\
\overset{2}{g}{}^{ij} &= -\overset{2}{g}_{ij}. & (1.77)
\end{align}
$$

The affine connection $\Gamma^{\mu}_{\nu\lambda}$ can be described with $\overset{N}{g}_{\mu\nu}$ by substituting the expansion of the metric into Eq. (1.62). I denote the $(v/c)^N r^{-1}$ order term of $\Gamma^{\mu}_{\nu\lambda}$ as $\overset{N}{\Gamma}^{\mu}_{\nu\lambda}$. In order to include up to $(v/c)^4$-order terms into the right-hand-side of the Eq. (1.63), the affine connections should be expanded as

$$
\begin{align}
\Gamma^{i}_{00} &= \overset{2}{\Gamma}{}^{i}_{00} + \overset{4}{\Gamma}{}^{i}_{00}, & (1.78)\\
\Gamma^{i}_{0j} &= \overset{3}{\Gamma}{}^{i}_{0j}, & (1.79)\\
\Gamma^{i}_{jk} &= \overset{2}{\Gamma}{}^{i}_{jk}, & (1.80)\\
\Gamma^{0}_{00} &= \overset{3}{\Gamma}{}^{0}_{00}, & (1.81)\\
\Gamma^{0}_{0j} &= \overset{2}{\Gamma}{}^{0}_{0i}, & (1.82)\\
\Gamma^{0}_{jk} &= \overset{1}{\Gamma}{}^{0}_{ij}. & (1.83)
\end{align}
$$

All terms with order higher than those written above are neglected because they correspond to higher-order PN terms. Each component in the expansions are described with $\overset{N}{g}_{\mu\nu}$ as

$$\overset{2}{\Gamma}{}^i_{00} = -\frac{1}{2}\frac{\partial \overset{2}{g}_{00}}{\partial x^i}, \tag{1.84}$$

$$\overset{4}{\Gamma}{}^i_{00} = -\frac{1}{2}\frac{\partial \overset{4}{g}_{00}}{\partial x^i} + \frac{1}{c}\frac{\partial \overset{3}{g}_{i0}}{\partial t} + \frac{1}{2}\overset{2}{g}_{ij}\frac{\partial \overset{2}{g}_{00}}{\partial x^j}, \tag{1.85}$$

$$\overset{3}{\Gamma}{}^i_{0j} = \frac{1}{2}\left(\frac{1}{c}\frac{\partial \overset{2}{g}_{ij}}{\partial t} + \frac{\partial \overset{3}{g}_{i0}}{\partial x^j} - \frac{\partial \overset{3}{g}_{j0}}{\partial x^i}\right), \tag{1.86}$$

$$\overset{2}{\Gamma}{}^i_{jk} = \frac{1}{2}\left(\frac{\partial \overset{2}{g}_{ik}}{\partial x^j} + \frac{\partial \overset{2}{g}_{ij}}{\partial x^k} - \frac{\partial \overset{2}{g}_{jk}}{\partial x^i}\right), \tag{1.87}$$

$$\overset{3}{\Gamma}{}^0_{00} = -\frac{1}{2c}\frac{\partial \overset{2}{g}_{00}}{\partial t}, \tag{1.88}$$

$$\overset{2}{\Gamma}{}^0_{0i} = -\frac{1}{2}\frac{\partial \overset{2}{g}_{00}}{\partial x^i}, \tag{1.89}$$

$$\overset{1}{\Gamma}{}^0_{ij} = 0. \tag{1.90}$$

The Ricci tensor $R_{\mu\nu}$ is described with the affine connections as

$$R_{\mu\nu} = R^\lambda_{\mu\lambda\nu} \tag{1.91}$$

$$= \frac{\partial \Gamma^\lambda_{\mu\lambda}}{\partial x^\nu} - \frac{\partial \Gamma^\lambda_{\mu\nu}}{\partial x^\lambda} + \Gamma^\eta_{\mu\lambda}\Gamma^\lambda_{\nu\eta} - \Gamma^\eta_{\mu\nu}\Gamma^\lambda_{\eta\lambda}. \tag{1.92}$$

By substituting the expansions of the affine connections into the above description, the Ricci tensor is expanded as

$$R_{00} = \overset{2}{R}_{00} + \overset{4}{R}_{00}, \tag{1.93}$$

$$R_{i0} = \overset{3}{R}_{i0}, \tag{1.94}$$

$$R_{ij} = \overset{2}{R}_{ij}, \tag{1.95}$$

where $\overset{N}{R}_{\mu\nu}$ is $(v/c)^N r^{-2}$ order component of the Ricci tensor, which is described with $\overset{N}{g}_{\mu\nu}$ as

$$\overset{2}{R}_{00} = \frac{1}{2}\nabla^2 \overset{2}{g}_{00}, \tag{1.96}$$

$$\begin{aligned}
\overset{4}{R}_{00} &= \frac{1}{2c^2}\frac{\partial^2 \overset{2}{g}_{ii}}{\partial t^2} - \frac{1}{c}\frac{\partial^2 \overset{3}{g}_{i0}}{\partial x^i \partial t} + \frac{1}{2}\nabla^2 \overset{4}{g}_{00} - \frac{1}{2}\overset{2}{g}_{ij}\frac{\partial^2 \overset{2}{g}_{00}}{\partial x^i \partial x^j} \\
&\quad - \frac{1}{2}\frac{\partial \overset{2}{g}_{ij}}{\partial x^j}\frac{\partial \overset{2}{g}_{00}}{\partial x^i} + \frac{1}{4}\frac{\partial \overset{2}{g}_{00}}{\partial x^i}\frac{\partial \overset{2}{g}_{00}}{\partial x^i} + \frac{1}{4}\frac{\partial \overset{2}{g}_{00}}{\partial x^i}\frac{\partial \overset{2}{g}_{jj}}{\partial x^i},
\end{aligned} \tag{1.97}$$

$$\overset{3}{R}_{i0} = \frac{1}{2c}\frac{\partial^2 \overset{2}{g}_{jj}}{\partial x^i \partial t} - \frac{1}{2}\frac{\partial^2 \overset{3}{g}_{j0}}{\partial x^i \partial x^j} - \frac{1}{2c}\frac{\partial^2 \overset{2}{g}_{ij}}{\partial x^i \partial t} + \frac{1}{2}\nabla^2 \overset{3}{g}_{i0}, \tag{1.98}$$

$$\overset{2}{R}_{ij} = -\frac{1}{2}\frac{\partial^2 \overset{2}{g}_{00}}{\partial x^i \partial x^j} + \frac{1}{2}\frac{\partial^2 \overset{2}{g}_{kk}}{\partial x^i \partial x^j} - \frac{1}{2}\frac{\partial^2 \overset{2}{g}_{jk}}{\partial x^i \partial x^k} - \frac{1}{2}\frac{\partial^2 \overset{2}{g}_{ik}}{\partial x^j \partial x^k} + \frac{1}{2}\nabla^2 \overset{2}{g}_{ij}. \tag{1.99}$$

These components can be described more simply when the gauge condition is fixed as the harmonic coordinate condition, that is, $g^{\mu\nu}\Gamma^\lambda_{\mu\nu} = 0$. This condition imposes additional equations of expanded components as

$$\frac{1}{2c}\frac{\partial \overset{2}{g}_{00}}{\partial t} - \frac{\partial \overset{3}{g}_{0i}}{\partial x^i} + \frac{1}{2c}\frac{\partial \overset{2}{g}_{ii}}{\partial t} = 0, \tag{1.100}$$

$$\frac{1}{2}\frac{\partial \overset{2}{g}_{00}}{\partial x^i} + \frac{\partial \overset{2}{g}_{ij}}{\partial x^j} - \frac{1}{2}\frac{\partial \overset{2}{g}_{jj}}{\partial x^i} = 0. \tag{1.101}$$

The partial derivative of these equations by t and x^k give three equations that make the descriptions of the components of the Ricci tensor simpler:

$$\frac{1}{2c}\frac{\partial^2 \overset{2}{g}_{00}}{\partial t^2} - \frac{\partial^2 \overset{3}{g}_{0i}}{\partial t \partial x^i} + \frac{1}{2c}\frac{\partial^2 \overset{2}{g}_{ii}}{\partial t^2} = 0, \tag{1.102}$$

$$-\frac{1}{c}\frac{\partial^2 \overset{2}{g}_{ij}}{\partial t \partial x^i} - \frac{\partial^2 \overset{3}{g}_{0i}}{\partial x^i \partial x^j} + \frac{1}{c}\frac{\partial^2 \overset{2}{g}_{ii}}{\partial t \partial x^j} = 0, \tag{1.103}$$

$$\frac{\partial^2 \overset{2}{g}_{ij}}{\partial x^j \partial x^k} + \frac{\partial^2 \overset{2}{g}_{kj}}{\partial x^i \partial x^j} + \frac{\partial^2 \overset{2}{g}_{00}}{\partial x^j \partial x^k} + \frac{\partial^2 \overset{2}{g}_{jj}}{\partial x^i \partial x^k} = 0. \tag{1.104}$$

The expanded components of the Ricci tensor are hence obtained by substituting the above three equations into Eqs. (1.96) to (1.99) as

$$\overset{2}{R}_{00} = \frac{1}{2}\nabla^2 \overset{2}{g}_{00}, \tag{1.105}$$

$$\overset{4}{R}_{00} = \frac{1}{2}\nabla^2 \overset{4}{g}_{00} - \frac{1}{2c^2}\frac{\partial^2 \overset{2}{g}_{00}}{\partial t^2} - \frac{1}{2}\overset{2}{g}_{ij}\frac{\partial^2 \overset{2}{g}_{00}}{\partial x^i \partial x^j} + \frac{1}{2}\left(\nabla \overset{2}{g}_{00}\right)^2, \tag{1.106}$$

$$\overset{3}{R}_{i0} = \frac{1}{2}\nabla^2 \overset{3}{g}_{i0}, \tag{1.107}$$

$$\overset{2}{R}_{ij} = \frac{1}{2}\nabla^2 \overset{2}{g}_{ij}. \tag{1.108}$$

Solving the Einstein equations

First, the Einstein equations $G_{\mu\nu} = -(8\pi G/c^4)T_{\mu\nu}$ are rewritten in another form for convenience. The Einstein tensor $G_{\mu\nu}$ is defined as

$$G_{\mu\nu} = R_{\mu\nu} - \frac{1}{2}g_{\mu\nu}R, \tag{1.109}$$

where $R \equiv R^\mu{}_\mu$ is the Ricci scalar. By substituting this definition, the Einstein equations are rewritten as

$$R_{\mu\nu} - \frac{1}{2}g_{\mu\nu}R = -\frac{8\pi G}{c^4}T_{\mu\nu}. \tag{1.110}$$

When the tensor contraction of these equations and $g^{\lambda\mu}$ are calculated, we obtain

$$R^{\lambda}{}_{\nu} - \frac{1}{2}\delta^{\lambda}{}_{\nu}R = -\frac{8\pi G}{c^4}T^{\lambda}{}_{\nu}. \tag{1.111}$$

If the superscript λ is set as ν and the tensor contraction is calculated, the Ricci scalar R can be described with the trace of the energy-momentum tensor $T \equiv T^{\nu}{}_{\nu}$ as

$$R = \frac{8\pi G}{c^4}T. \tag{1.112}$$

The Einstein equation (1.110) is rewritten with this description as

$$R_{\mu\nu} = -\frac{8\pi G}{c^4}\left(T_{\mu\nu} - \frac{1}{2}g_{\mu\nu}T\right). \tag{1.113}$$

The tensor in the brackets on the right-hand side is hereafter denoted as $S_{\mu\nu}$.

In order to solve these equations for each expanded components in Eqs. (1.105) to (1.108), the expansion of $S_{\mu\nu}$ on the right-hand side is required. The energy-momentum tensor $T^{\mu\nu}$ can be expanded with $(v/c)^2$ by considering the physical value which each component of the tensor corresponds to: T^{00}, T^{i0}, and T^{ij} correspond to the energy density, the momentum density, and the momentum flux, respectively. Each component is expanded as

$$T^{00} = \overset{0}{T}{}^{00} + \overset{2}{T}{}^{00} + \ldots, \tag{1.114}$$

$$T^{i0} = \overset{1}{T}{}^{i0} + \overset{3}{T}{}^{i0} + \ldots, \tag{1.115}$$

$$T^{ij} = \overset{2}{T}{}^{ij} + \overset{4}{T}{}^{ij} + \ldots, \tag{1.116}$$

where $\overset{N}{T}{}^{\mu\nu}$ means $(v/c)^{N-2}mv^2r^{-3}$-order term. The expanded components of $S_{\mu\nu}$ are calculated with these expansions as

$$\overset{0}{S}_{00} = \frac{1}{2}\overset{0}{T}{}^{00}, \tag{1.117}$$

$$\overset{2}{S}_{00} = \frac{1}{2}\left(\overset{2}{T}{}^{00} - \overset{2}{g}_{00}\overset{0}{T}{}^{00} + \overset{2}{T}{}^{ii}\right), \tag{1.118}$$

$$\overset{1}{S}_{i0} = -\overset{1}{T}{}^{i0}, \tag{1.119}$$

$$\overset{0}{S}_{ij} = \frac{1}{2}\delta_{ij}\overset{0}{T}{}^{00}. \tag{1.120}$$

Note that the components with an order higher than those shown above are needed only when the higher-order PN approximation effects are considered. The Einstein equations for the expanded components are obtained therefore as

$$\overset{2}{R}_{00} = -\frac{8\pi G}{c^4}\overset{0}{S}_{00}, \tag{1.121}$$

$$\overset{2}{R}_{ij} = -\frac{8\pi G}{c^4}\overset{0}{S}_{ij}, \tag{1.122}$$

$$\overset{3}{R}_{i0} = -\frac{8\pi G}{c^4}\overset{1}{S}_{i0}, \tag{1.123}$$

$$\overset{4}{R}_{00} = -\frac{8\pi G}{c^4}\overset{2}{S}_{00}. \tag{1.124}$$

By substituting Eqs. (1.105) and (1.117) into Eq. (1.121), the differential equations for $\overset{2}{g}_{00}$ is obtained as

$$\nabla^2 \overset{2}{g}_{00} = -\frac{8\pi G}{c^4} \overset{0}{T}^{00}. \tag{1.125}$$

The metric component $\overset{2}{g}_{00}$ can be described with Newtonian gravitational potential ϕ as

$$\overset{2}{g}_{00} = -\frac{2\phi}{c^2}, \tag{1.126}$$

where the potential ϕ is defined in the below equation:

$$\nabla^2 \phi = \frac{4\pi G}{c^2} \overset{0}{T}^{00}. \tag{1.127}$$

This differential equation has the solution that becomes zero at infinity as

$$\phi\left(\boldsymbol{r}, t\right) = -\frac{G}{c^2} \int d^3 \boldsymbol{r}' \frac{\overset{0}{T}^{00}\left(\boldsymbol{r}', t\right)}{\left|\boldsymbol{r} - \boldsymbol{r}'\right|}, \tag{1.128}$$

where $\boldsymbol{r}$ is the 3-dimensional coordinates described as a vector.

From Eq. (1.122), the differential equations for $\overset{2}{g}_{ij}$ is obtained in a similar form as

$$\nabla^2 \overset{2}{g}_{ij} = -\frac{8\pi G}{c^4} \delta_{ij} \overset{0}{T}^{00}, \tag{1.129}$$

and the solution is obtained as

$$\overset{2}{g}_{ij} = -\frac{2\delta_{ij}\phi}{c^2}. \tag{1.130}$$

As for $\overset{3}{g}_{i0}$, the differential equation is obtained by substituting Eqs. (1.107) and (1.119) into Eq. (1.123) as

$$\nabla^2 \overset{3}{g}_{i0} = \frac{16\pi G}{c^4} \overset{1}{T}^{i0}. \tag{1.131}$$

Here another potential called vector potential $\boldsymbol{\zeta}$ is defined as

$$\nabla^2 \zeta_i = \frac{16\pi G}{c^2} \overset{1}{T}^{i0}, \tag{1.132}$$

and this equation is solved as

$$\zeta_i\left(\boldsymbol{r}, t\right) = -\frac{4G}{c^2} \int d^3 \boldsymbol{r}' \frac{\overset{1}{T}^{i0}\left(\boldsymbol{r}', t\right)}{\left|\boldsymbol{r} - \boldsymbol{r}'\right|}. \tag{1.133}$$

The metric component $\overset{3}{g}_{i0}$ is therefore described with $\boldsymbol{\zeta}$ as

$$\overset{3}{g}_{i0} = \frac{\zeta_i}{c^2}. \tag{1.134}$$

The differential equation about $\overset{4}{g}_{00}$ is obtained by substituting Eqs. (1.106) and (1.118) into Eq. (1.124) and by using Eqs. (1.126) and (1.130):

$$\nabla^2 \overset{4}{g}_{00} = -\frac{2}{c^4}\nabla^2\phi^2 - \frac{2}{c^2}\left[\frac{1}{c^2}\frac{\partial^2\phi}{\partial t^2} + \frac{4\pi G}{c^2}\left(\overset{2}{T}{}^{00} + \overset{2}{T}{}^{ii}\right)\right]. \tag{1.135}$$

The terms in the square brackets on the right-hand side are replaced with so-called second potential, which is defined as

$$\nabla^2\Psi = \frac{1}{c^2}\frac{\partial^2\phi}{\partial t^2} + \frac{4\pi G}{c^2}\left(\overset{2}{T}{}^{00} + \overset{2}{T}{}^{ii}\right). \tag{1.136}$$

The solution of this differential equation that becomes zero at infinity is

$$\Psi(\boldsymbol{r},t) = -\int \frac{d^3\boldsymbol{r}'}{|\boldsymbol{r}-\boldsymbol{r}'|}\left[\frac{1}{4\pi c^2}\frac{\partial^2\phi(\boldsymbol{r},t)}{\partial t^2} + \frac{G}{c^2}\overset{2}{T}{}^{00}(\boldsymbol{r},t) + \frac{G}{c^2}\overset{2}{T}{}^{ii}(\boldsymbol{r},t)\right]. \tag{1.137}$$

Hence the metric component $\overset{4}{g}_{00}$ is described as

$$\overset{4}{g}_{00} = -\frac{2\phi^2}{c^4} - \frac{2\Psi}{c^2}. \tag{1.138}$$

The energy-momentum tensor

Now all the expanded components of the metric needed to obtain 1PN equations of motion are described with the expanded components of the energy-momentum tensor. Next, the expanded components of the energy-momentum tensor are described as the functions of masses, positions, and velocities of the N-body point particles. In general relativity, the energy-momentum tensor is given as

$$T^{\mu\nu}(\boldsymbol{r},t) = g^{-\frac{1}{2}}(\boldsymbol{r},t)\sum_n m_n \frac{dx_n^\mu(t)}{dt}\frac{dx_n^\nu(t)}{dt}\left(\frac{d\tau_n}{dt}\right)^{-1}\delta^3(\boldsymbol{r}-\boldsymbol{r}_n(t)), \tag{1.139}$$

where m_n, x_n^μ, and τ_n are the mass, the 4-dimensional coordinates, and the proper time of the n-th particle, respectively, and $g = -\det g_{\mu\nu}$ is the determinant of the metric. From the definition of the proper time, $d\tau^2 = -c^{-2}g_{\mu\nu}dx^\mu dx^\nu$, the time derivative of the proper time is calculated as

$$\frac{d\tau}{dt} = \left[-g_{00} - 2g_{i0}\left(\frac{v^i}{c}\right) - g_{ij}\left(\frac{v^i}{c}\right)\left(\frac{v^j}{c}\right)\right]^{\frac{1}{2}}, \tag{1.140}$$

where v^i denotes the velocity. When all the obtained components of $g_{\mu\nu}$ (Eqs. (1.69) to (1.71), (1.126), (1.130), (1.131) and (1.138)) are substituted into the right-hand side, it becomes

$$\frac{d\tau}{dt} = \left[1 + \frac{1}{c^2}(2\phi - v^2) + \frac{2}{c^2}\left\{\frac{\phi^2}{c^2} + \Psi - \boldsymbol{\zeta}\cdot\left(\frac{\boldsymbol{v}}{c}\right) + \phi\left(\frac{v}{c}\right)^2\right\}\right]^{\frac{1}{2}}. \tag{1.141}$$

From this description, $(d\tau_n/dt)^{-1}$ in Eq.(1.139) is calculated as

$$\left(\frac{d\tau_n}{dt}\right)^{-1} = 1 - \frac{\phi}{c^2} + \frac{1}{2}\left(\frac{v}{c}\right)^2 + \mathcal{O}\left(\left(\frac{v}{c}\right)^4\right). \tag{1.142}$$

Note that the higher-order terms are neglected here because they are not needed to calculate the energy-momentum tensor up to the second order. The determinant of the metric g expanded as $g = 1 + \overset{2}{g} + \overset{4}{g} + \ldots$ and the terms up to second order are needed now. The second-order term $\overset{2}{g}$ is calculated as $\overset{2}{g} = -4\phi/c^2$, and g is described as

$$g = 1 - \frac{4\phi}{c^2} + \mathcal{O}\left(\left(\frac{v}{c}\right)^4\right). \tag{1.143}$$

By substituting Eqs. (1.142) and (1.143) into Eq. (1.139), each expanded component of the energy-momentum tensor is obtained as

$$\overset{0}{T}{}^{00} = \sum_n m_n c^2 \delta^3\left(\boldsymbol{r} - \boldsymbol{r}_n(t)\right), \tag{1.144}$$

$$\overset{2}{T}{}^{00} = \sum_n m_n c^2 \left(\frac{\phi_n}{c^2} + \frac{1}{2}\left(\frac{v_n}{c}\right)^2\right)\delta^3\left(\boldsymbol{r} - \boldsymbol{r}_n(t)\right), \tag{1.145}$$

$$\overset{1}{T}{}^{i0} = \sum_n m_n c^2 \frac{v_n^i}{c}\delta^3\left(\boldsymbol{r} - \boldsymbol{r}_n(t)\right), \tag{1.146}$$

$$\overset{2}{T}{}^{ij} = \sum_n m_n c^2 \frac{v_n^i}{c}\frac{v_n^j}{c}\delta^3\left(\boldsymbol{r} - \boldsymbol{r}_n(t)\right). \tag{1.147}$$

The equations of motion

By substituting Eqs. (1.126), (1.130), (1.131) and (1.138)) into Eqs. (1.84) to (1.90), the affine connections required to obtain the equations of motion are described with the potentials as

$$\overset{2}{\Gamma}{}^i_{00} = \frac{1}{c^2}\frac{\partial\phi}{\partial x^i}, \tag{1.148}$$

$$\overset{4}{\Gamma}{}^i_{00} = \frac{\partial}{\partial x^i}\left(\frac{2\phi^2}{c^4} + \frac{\Psi}{c^2}\right) + \frac{1}{c^3}\frac{\partial\zeta_i}{\partial t}, \tag{1.149}$$

$$\overset{3}{\Gamma}{}^i_{0j} = \frac{1}{2c^2}\left(\frac{\partial\zeta_i}{\partial x^j} - \frac{\partial\zeta_j}{\partial x^i}\right) - \frac{\delta_{ij}}{c^3}\frac{\partial\phi}{\partial t}, \tag{1.150}$$

$$\overset{2}{\Gamma}{}^i_{jk} = -\frac{\delta_{ik}}{c^2}\frac{\partial\phi}{\partial x^j} - \frac{\delta_{ij}}{c^2}\frac{\partial\phi}{\partial x^k} + \frac{\delta_{jk}}{c^2}\frac{\partial\phi}{\partial x^i}, \tag{1.151}$$

$$\overset{3}{\Gamma}{}^0_{00} = \frac{1}{c^3}\frac{\partial\phi}{\partial t}, \tag{1.152}$$

$$\overset{2}{\Gamma}{}^0_{0i} = \frac{1}{c^2}\frac{\partial\phi}{\partial x^i}, \tag{1.153}$$

$$\overset{1}{\Gamma}{}^0_{ij} = 0. \tag{1.154}$$

The equations of motion are described with the potentials by using the above descriptions in Eq. (1.63) as

$$\begin{aligned}
\frac{d\boldsymbol{v}}{dt} &= -\nabla\left(\phi + \frac{2\phi^2}{c^2} + \Psi\right) - \frac{1}{c}\frac{\partial\boldsymbol{\zeta}}{\partial t} + \frac{\boldsymbol{v}}{c}\times(\nabla\times\boldsymbol{\zeta}) \\
&\quad + 3\frac{\boldsymbol{v}}{c}\frac{\partial\phi}{\partial t} + 4\frac{\boldsymbol{v}}{c}\left(\frac{\boldsymbol{v}}{c}\cdot\nabla\phi\right) - \left(\frac{v}{c}\right)^2\nabla\phi.
\end{aligned} \tag{1.155}$$

The potentials are written in Eqs. (1.128), (1.133) and (1.137) as the functions of the components of the energy-momentum tensor, which are calculated for N-body systems in Eqs. (1.144) to (1.147). By substituting latter equations into former ones, the potentials are calculated as

$$\phi\left(\boldsymbol{r}, t\right) = -G \sum_n \frac{m_n}{\left|\boldsymbol{r} - \boldsymbol{r}_n(t)\right|}, \tag{1.156}$$

$$\boldsymbol{\zeta}\left(\boldsymbol{r}, t\right) = -\frac{4G}{c} \sum_n \frac{m_n \boldsymbol{v}_n}{\left|\boldsymbol{r} - \boldsymbol{r}_n(t)\right|}, \tag{1.157}$$

$$\Psi\left(\boldsymbol{r}, t\right) = -G \sum_n \frac{m_n}{\left|\boldsymbol{r} - \boldsymbol{r}_n(t)\right|}\left[-\frac{1}{2}\left\{ \frac{\boldsymbol{r} - \boldsymbol{r}_n(t)}{\left|\boldsymbol{r} - \boldsymbol{r}_n(t)\right|} \cdot \left(\frac{\boldsymbol{v}_n}{c}\right)\right\}^2 \right.$$
$$\left. + 2\left(\frac{v_n}{c}\right)^2 + \frac{\phi_n}{c^2} - \frac{1}{2c^2}(\boldsymbol{r} - \boldsymbol{r}_n(t)) \cdot \frac{d\boldsymbol{v}_n}{dt} \right]. \tag{1.158}$$

Finally, the 1PN equations of motion called Einstein-Infeld-Hoffmann (EIH) equations are obtained by calculating Eq. (1.155) by using Eqs. (1.156) to (1.158) and neglecting higher-order terms as

$$\frac{\mathrm{d}\boldsymbol{v}_k}{\mathrm{d}t} = -G \sum_{n \neq k} m_n \frac{\boldsymbol{r}_k - \boldsymbol{r}_n}{\left|\boldsymbol{r}_k - \boldsymbol{r}_n\right|^3}\left[1 - 4\frac{G}{c^2} \sum_{n' \neq k} \frac{m_{n'}}{\left|\boldsymbol{r}_k - \boldsymbol{r}_{n'}\right|} \right.$$
$$- \frac{G}{c^2} \sum_{n' \neq n} \frac{m_{n'}}{\left|\boldsymbol{r}_n - \boldsymbol{r}_{n'}\right|}\left\{ 1 - \frac{(\boldsymbol{r}_k - \boldsymbol{r}_n) \cdot (\boldsymbol{r}_n - \boldsymbol{r}_{n'})}{2\left|\boldsymbol{r}_n - \boldsymbol{r}_{n'}\right|^2} \right\}$$
$$+ \left(\frac{\left|\boldsymbol{v}_k\right|}{c}\right)^2 + 2\left(\frac{\left|\boldsymbol{v}_n\right|}{c}\right)^2 - 4\frac{\boldsymbol{v}_k \cdot \boldsymbol{v}_n}{c^2} - \frac{3}{2}\left\{ \frac{(\boldsymbol{r}_k - \boldsymbol{r}_n)}{\left|\boldsymbol{r}_k - \boldsymbol{r}_n\right|} \cdot \frac{\boldsymbol{v}_n}{c} \right\}^2 \right]$$
$$- \frac{G}{c^2} \sum_{n \neq k} \frac{m_n(\boldsymbol{v}_k - \boldsymbol{v}_n)}{\left|\boldsymbol{r}_k - \boldsymbol{r}_n\right|^3}(\boldsymbol{r}_k - \boldsymbol{r}_n) \cdot (3\boldsymbol{v}_n - 4\boldsymbol{v}_k)$$
$$- \frac{7}{2}\frac{G^2}{c^2} \sum_{n \neq k} \frac{m_n}{\left|\boldsymbol{r}_k - \boldsymbol{r}_n\right|} \sum_{n' \neq n} \frac{m_{n'}(\boldsymbol{r}_n - \boldsymbol{r}_{n'})}{\left|\boldsymbol{r}_n - \boldsymbol{r}_{n'}\right|^3}, \tag{1.159}$$

where the subscript k means the k-th object in an N-body system. In this thesis, I use these equations of motion to calculate orbital evolutions of the relativistic multi-body systems.

The 1PN Hamiltonian $\mathcal{H}_{1\mathrm{PN}}$ and the 1PN linear momentum $\boldsymbol{P}$ for a general N-body system can be obtained from these equations of motion as

$$\mathcal{H}_{1\mathrm{PN}} = \frac{1}{2} \sum_j m_j\left(v_j^2 - \sum_{i \neq j} \frac{Gm_i}{r_{ij}} \right)$$
$$+ \frac{1}{c^2} \sum_j m_j\left[\frac{3}{8}v_j^4 + \frac{3}{2}v_j^2 \sum_{i \neq j} \frac{Gm_i}{r_{ij}} + \frac{1}{2} \sum_{i \neq j} \sum_{k \neq j} \frac{G^2 m_i m_k}{r_{ij} r_{jk}} \right.$$
$$\left. - \frac{1}{4} \sum_{i \neq j} \frac{Gm_i}{r_{ij}}\{7\boldsymbol{v}_i \cdot \boldsymbol{v}_j + (\boldsymbol{v}_i \cdot \boldsymbol{n}_{ji})(\boldsymbol{v}_j \cdot \boldsymbol{n}_{ji})\} \right], \tag{1.160}$$

$$\boldsymbol{P}_j = m_j \boldsymbol{v}_j + \left[\frac{1}{2c^2} m_j \boldsymbol{v}_j \left(v_j^2 - \sum_{i \neq j} \frac{Gm_i}{r_{ij}} \right) - \frac{G}{2c^2} \sum_{i \neq j} \frac{m_i m_j}{r_{ij}} (\boldsymbol{v}_j \cdot \boldsymbol{n}_{ji}) \boldsymbol{n}_{ji} \right], \quad (1.161)$$

where $r_{ij} \equiv |\boldsymbol{r}_j - \boldsymbol{r}_i|$ and $\boldsymbol{n}_{ji}$ is the unit vector whose direction is the same as that of $\boldsymbol{r}_i - \boldsymbol{r}_j$.

1.2.2 Post-Newtonian Corrections to Double-Averaging Method

As in the Newtonian stellar dynamics, the double-averaging method is commonly used to discuss secular dynamics of relativistic N-body systems (e.g. Blaes et al. (2002); Naoz et al. (2013b); Rafikov (2014); Liu and Lai (2017)). The relativistic effects are usually included as some PN correction terms that are added to the Newtonian equations. Here I introduce several discussions about the PN corrections to the double-averaging method.

For restricted triple systems, the simplest 1PN correction term is obtained by considering the 1PN Hamiltonian of the relative motion of the inner binary and neglecting 1PN effects coming from the outer orbit (see e.g. Migaszewski and Goździewski (2011)). The 1PN specific Hamiltonian for the relative motion $\boldsymbol{r} = \boldsymbol{r}_2 - \boldsymbol{r}_1$ was originally obtained by Richardson and Kelly (1988) from the N-body Hamiltonian Eq. (1.160) as

$$\mathcal{H}_{\text{rel}} = \frac{1}{2} \boldsymbol{p} \cdot \boldsymbol{p} - \frac{G(m_1 + m_i)}{r} - \frac{1}{c^2} \left[\sigma_0 (\boldsymbol{p} \cdot \boldsymbol{p})^2 + \frac{\sigma_1}{r} \boldsymbol{p} \cdot \boldsymbol{p} + \frac{\sigma_2}{r^2} + \frac{\sigma_3}{r^3} (\boldsymbol{r} \cdot \boldsymbol{p})^2 \right], \quad (1.162)$$

where $\boldsymbol{p}$ is the specific linear momentum for the relative motion, which is defined as

$$\boldsymbol{p} = \boldsymbol{v} + \frac{1}{c^2} \left[4\sigma_0 v^2 \boldsymbol{v} + \frac{2\sigma_1}{r} \boldsymbol{v} + \frac{2\sigma_3}{r^3} (\boldsymbol{r} \cdot \boldsymbol{v}) \boldsymbol{r} \right]. \quad (1.163)$$

The coefficients are given as

$$\sigma_0 = \frac{1 - 3\chi}{8}, \quad (1.164)$$

$$\sigma_1 = \frac{G(m_1 + m_i)(3 + \chi)}{2}, \quad (1.165)$$

$$\sigma_2 = -\frac{G^2 (m_1 + m_i)^2}{2}, \quad (1.166)$$

$$\sigma_3 = \frac{G(m_1 + m_i)\chi}{2}, \quad (1.167)$$

$$\chi = \frac{m_1 m_i}{(m_1 + m_i)^2}. \quad (1.168)$$

By calculating the orbital average of the 1PN term in Eq. (1.162), the 1PN correction term for the secular potential is obtained as

$$V^{(\text{1PN})} = \frac{3 G^2 (m_1 + m_2)^2}{c^2 a_{\text{in}}^2 \sqrt{1 - e_{\text{in}}^2}} + \text{const.}, \quad (1.169)$$

and the 1PN orbital evolution can be calculated by replacing V_{s} in Eqs. (1.55) to (1.59) by $V_{\mathrm{s}}^{(1\mathrm{PN})} = V_{\mathrm{s}} + V^{(1\mathrm{PN})}$. The additional term in the Lagrange planetary equations appears only in the equation for ω_{in}:

$$
\begin{aligned}
\frac{d\omega_{\mathrm{in}}}{dt} &= \frac{\sqrt{1-e_{\mathrm{in}}^2}}{a_{\mathrm{in}}^2 n_{\mathrm{in}} e_{\mathrm{in}}} \frac{\partial V_{\mathrm{s}}^{(1\mathrm{PN})}}{\partial e_{\mathrm{in}}} - \frac{\cot I}{a_{\mathrm{in}}^2 n_{\mathrm{in}} \sqrt{1-e_{\mathrm{in}}^2}} \frac{\partial V_{\mathrm{s}}^{(1\mathrm{PN})}}{\partial I} \\
&= \frac{\sqrt{1-e_{\mathrm{in}}^2}}{a_{\mathrm{in}}^2 n_{\mathrm{in}} e_{\mathrm{in}}} \frac{\partial V_s}{\partial e_{\mathrm{in}}} - \frac{\cot I}{a_{\mathrm{in}}^2 n_{\mathrm{in}} \sqrt{1-e_{\mathrm{in}}^2}} \frac{\partial V_s}{\partial I} + \frac{\sqrt{1-e_{\mathrm{in}}^2}}{a_{\mathrm{in}}^2 n_{\mathrm{in}} e_{\mathrm{in}}} \frac{\partial V^{(1\mathrm{PN})}}{\partial e_{\mathrm{in}}}.
\end{aligned} \quad (1.170)
$$

The last term in the second line of the above equation corresponds to the periastron shift, which is one of the most famous relativistic effects confirmed by the observation.

This 1PN correction is very simple and easy to calculate, but Will (2014a,b) pointed out that this method may violate the energy conservation in a long-term calculation. The averaged specific energy of the inner orbit is described as

$$
\langle E_{\mathrm{in}} \rangle = -\frac{G(m_1 + m_2)}{2 a_{\mathrm{in}}} - \left(V_{\mathrm{s}} + V^{(1\mathrm{PN})} \right). \quad (1.171)
$$

In a restricted triple system, the outer orbital energy is assumed not to change, that is, from the energy conservation, the inner orbital energy should be conserved. From Eqs. (1.54) and (1.169), the averaged inner-orbital energy depends on the semi-major axis a_{in}, the eccentricity e_{in}, the argument of periastron ω_{in}, and the relative inclination I. Will (2014b) calculated the variation of each element while an inner orbital cycle as

$$
\int_0^{P_{\mathrm{in}}} \frac{da_{\mathrm{in}}}{dt} dt = 0, \quad (1.172)
$$

$$
\int_0^{P_{\mathrm{in}}} \frac{de_{\mathrm{in}}}{dt} dt = \frac{15\pi}{2} \frac{m_3}{m_2} \left(\frac{a_{\mathrm{in}}}{a_{\mathrm{out}}} \right)^3 e_{\mathrm{in}} (1-e_{\mathrm{in}}^2)^{\frac{1}{2}} \sin^2 I \sin \omega_{\mathrm{in}} \cos \omega_{\mathrm{in}} \quad (1.173)
$$

$$
\int_0^{P_{\mathrm{in}}} \frac{dI}{dt} dt = -\frac{15\pi}{2} \frac{m_3}{m_2} \left(\frac{a_{\mathrm{in}}}{a_{\mathrm{out}}} \right)^3 \sin I \cos I \sin \omega_{\mathrm{in}} \cos \omega_{\mathrm{in}} \quad (1.174)
$$

$$
\begin{aligned}
\int_0^{P_{\mathrm{in}}} \frac{d\omega_{\mathrm{in}}}{dt} dt &= \frac{6\pi G m_2}{c^2 a (1-e_{\mathrm{in}}^2)} + \frac{3\pi}{2} \frac{m_3}{m_2} \left(\frac{a_{\mathrm{in}}}{a_{\mathrm{out}}} \right)^3 e_{\mathrm{in}} (1-e_{\mathrm{in}}^2)^{-\frac{1}{2}} \\
&\quad \times \left\{ 5\cos^2 I \sin^2 \omega_{\mathrm{in}} + (1-e_{\mathrm{in}}^2)\left(5\cos^2 \omega_{\mathrm{in}} - 3 \right) \right\}.
\end{aligned} \quad (1.175)
$$

From Eq. (1.172), one finds that the semi-major axis a_{in} does not vary on a secular timescale as in the Newtonian calculation. In Eqs. (1.173) and (1.174), the variations of the eccentricity e_{in} and the relative inclination I are proportional to the third order of $a_{\mathrm{in}}/a_{\mathrm{out}}$. However, the first term of Eq. (1.175) is a_{in}^{-1} order and much larger than the other terms, which contradicts the energy conservation. Will (2014a) claimed that this contradiction is caused by the lack of the "cross terms" between the multipole expansion shown in Eq. (1.39) and the post-Newtonian expansions. The differential equations for the secular evolution of the orbital elements with the cross terms were obtained in Naoz et al. (2013b) and Will (2014b) by calculating the multipole expansion in the EIH equations for a three-body system.

Even when the double-averaging method with the cross terms is used, the calculation may not be adequate. Some researchers stressed that the orbital evolutions calculated by the double-averaging method sometimes show deviation from that obtained from the direct integration of the equations of motion especially when the excitation of the orbital eccentricity occurs (Antonini and Perets, 2012; Luo et al., 2016; Antonini et al., 2016). This may be caused by the short distance at the periastron of the highly eccentric orbit, where the higher-order terms in the multipole expansion neglected in the double-averaging method sometimes become important (Antonini et al., 2016). This deviation appears even when the multipole expansion includes up to octupole-order terms (Luo et al., 2016). Will (2017) calculated the multipole expansion up to hexadecapole order and showed that even such higher-order effects could not be neglected in the orbital evolution with the excitation of the eccentricity. In this thesis, in order to avoid this difficulty, I calculated the direct integration of the EIH equations (1.159) in the numerical simulations. I discuss this problem again in Chapter 2.

The higher-order PN effects have also been considered in the double-averaging method. The most important effect is the gravitational radiation, which corresponds to the 2.5th PN order terms. This effect is usually included as the energy dissipation from the inner or outer binary orbit (see e.g. Blaes et al. (2002); Liu and Lai (2017)). Another PN effect that has lately focused on is the spin-orbit coupling called the Lense-Thirring effect (Fang and Huang, 2019; Fang et al., 2019; Liu et al., 2019). It corresponds to the 1.5th order PN terms derived from the two-body interaction (Barker and O'Connell, 1975). These higher-order PN effects are mainly treated not in the direct integration but the double-averaging method because they affect the orbital evolution on a secular timescale and take too much computational cost for the direct simulation. In this thesis, I do not compute these higher-order effects with the direct integration for the reason mentioned above, but in later chapters, discuss whether these effects are important or not by comparing their timescales.

1.3   Main topics in this thesis

This thesis intends to extend the discussions of multi-body dynamics that have been done in Newtonian mechanics into the general relativistic regime and aims to contribute to understanding more about the dynamics of relativistic multi-body systems. The two subjects are treated as the main topics of this thesis.

First, in Chapter 2, I focus on the ZLK mechanism, which is one of the most interesting orbital resonances seen in hierarchical triple systems. It is characterized by the secular oscillations of the inner eccentricity and the relative inclination between the inner and outer orbits. Recently, the gravitational wave (GW) signal emitted from the triple system with the ZLK mechanism has been actively investigated. I also focus on the GW emission caused by the ZLK mechanism but from a different perspective that the observation of the radio signal from a pulsar in the inner binary of the hierarchical triple system. The excitation of the inner eccentricity due to the ZLK mechanism enhances the GW emission and causes interesting evolution of the cumulative shift of the periastron time (CSPT), which can be observed through the radio signals from the pulsar. The orbital evolutions and the CSPT curves of a

variety of models with a pulsar are calculated. I compare the two simulation results obtained from the double-averaging method and direct integration to confirm how the results obtained from the former method can deviate from that obtained from the latter one, which is one of the main problems of the studies about the relativistic multi-body systems. I also investigate the parameter space of the models where the interesting feature in the CSPT curve can be observed on an appropriate timescale.

Second, I show the research of the relativistic effects on the Hill stability problem. The Hill stability is the stability problem of the multi-body systems against a close approach of one orbit to another. It has been hitherto studied mainly in Newtonian mechanics and few kinds of research have been devoted to a systematic examination of this stability problem, despite the recent increase of the attention to the relativistic multi-body systems. In Chapter 3, first I review the Newtonian studies of the Hill stability and expand the discussion to the general relativistic regime by using the 1PN approximation. The approximated sufficient condition for the 1PN stability is derived analytically by assuming limited configurations of three-body systems. The validity and usefulness of the approximated sufficient condition are confirmed by the 1PN numerical simulations for models with supermassive or intermediate-mass black holes as their central objects. I found that the 1PN effect makes the system more unstable than calculated in Newtonian mechanics in the sense of the Hill stability as expected by the theoretical prediction.

After the two main topics, I conclude this thesis in Chapter 4.

Chapter 2

von Zeipel-Lidov-Kozai Mechanism

2.1   Purpose

The von Zeipel-Lidov-Kozai (ZLK) mechanism is one of the most remarkable orbital resonances that occur in three-body systems. It has been called the "Kozai-Lidov" or "Lidov-Kozai" mechanism since the pioneer papers (Kozai, 1962; Lidov, 1962) were published. Recently, however, Ito and Ohtsuka (2019) found that the framework of the fundamental formulation of this mechanism had been already done by von Zeipel (1910), and the newly-proposed prefix "von Zeipel-Lidov-Kozai" started to be used. This mechanism is seen in hierarchical triple systems and characterized by the secular oscillations of the inner eccentricity and the relative inclination. These values evolve exchanging their values with each other, that is, when the eccentricity excites, the inclination decreases, and vice versa, on a timescale much longer than both the inner and outer-orbital periods.

The eccentricity excitation caused by the ZLK mechanism is thought to be quite important for various astrophysical phenomena. In a highly eccentric orbit, the distance between two stars at the orbital periastron point is much shorter than the orbital semi-major axis, and gravitational interactions between two stars become much stronger at this point. For example, the high eccentricity enhances the emission of the gravitational waves (GW), which may promote the merger of the compact binaries within the Hubble time (Blaes et al., 2002; Miller and Hamilton, 2002; Thompson, 2011; Antonini et al., 2017; Silsbee and Tremaine, 2017; Liu and Lai, 2017, 2018; Hoang et al., 2018; Randall and Xianyu, 2018; Fragione and Loeb, 2019). Another important gravitational interaction is the tidal force that causes the deformation of stars. Some researchers discussed the possibility of the tidal disruptions of stars around supermassive black holes due to the strong tidal force enhanced by the ZLK mechanism (Ivanov et al., 2005; Chen et al., 2009, 2011; Wegg and Bode, 2011; Li et al., 2015; Fragione and Leigh, 2018). The enhanced tidal force also causes the energy dissipation inside the star called tidal dissipation. The tidal dissipation enhanced by the ZLK mechanism is one of the candidates of the formation processes of the hot and warm Jupiters (Naoz et al., 2011, 2012; Petrovich, 2015; Frewen and Hansen, 2015; Anderson et al., 2016; Petrovich and Tremaine, 2016; Antonini1 et al.,

2016; Grishin et al., 2018) and the ultra-short-period planets (Oberst et al., 2017; Nielsen et al., 2020). Recently, the ZLK mechanism in four-body systems has been also considered as the sources of the above astrophysical phenomena (Hamers and Lai, 2017; Hamers and Safarzadeh, 2020; O'Connor et al., 2020).

From the context of the relativistic multi-body systems, the GW emission from the hierarchical triple systems with the ZLK mechanism has attracted the attention of researchers. Recently, not only the merger phase but also the regular orbiting phase is discussed as the candidate of the source of the observable GW (Hoang et al., 2019; Randall and Xianyu, 2019; Deme et al., 2020; Gupta et al., 2020). I also focus on the GW emission effects in the regular orbiting phase of the hierarchical triple systems but discuss the possibility of the indirect observation through the radio signal from the pulsars.

The radio observation that indirectly gives the information of the GW emission was done for the PSR B1913+16 system called the Hulse-Taylor binary. The Hulse-Taylor binary is one of the most famous binary pulsars, whose semi-major axis and the eccentricity are short and large enough that the orbit shrinks due to the GW emission (Hulse and Taylor, 1975; Taylor et al., 1976). The shrinking orbit decreases its orbital period. The decrease of the period clearly appeared in the cumulative shift of the periastron time (CSPT), which was observed over 30 yrs for the Hulse-Taylor binary (Weisberg and Taylor, 2005). The observed CSPT curve was explained quite well by the theoretical calculation of the GW emission effect in the general relativity and it was the first indirect evidence of the existence of the GW (Weisberg et al., 2010).

In this chapter, I focus on the evolution of the CSPT curve from the binary pulsar in a hierarchical triple system and discuss how the ZLK effect appears on the curve. If a deviation from the curve of the isolated binary is detected through the radio observation, it will be the first indirect observation of GW from a triple system. I also investigate the accuracy problem of the double-averaging method seen in the studies of the ZLK mechanism (explained in §1.2.2) by comparing the two simulation results obtained from the double-averaging method and direct integration.

In this chapter, first, the basic equations of the ZLK mechanism are introduced in both the Newtonian and 1PN calculations in §2.2. Second, in §2.3, I explain the formulation to calculate the CSPT in the hierarchical triple systems and show an example by using the parameters of an observed binary pulsar. I subsequently introduce various models with a pulsar as a component of the inner binary and discuss the parameter space where the effect of the ZLK mechanism appears on the CSPT curve on an appropriate timescale. In §2.4, first I show the orbital evolutions of the models and investigate the accuracy problem of the double-averaging method and 1PN effects on the ZLK mechanism, and then show the CSPT curves for various models. I summarize this chapter in §2.5.

2.2 Basic Equations of ZLK Mechanism

In this section, I review the basic equations of the ZLK mechanism obtained by the double-averaging method. Here I use the double-averaging method for the restricted triple systems introduced in §1.1.3 to grasp the main features of the ZLK mecha-

nism intuitively. First I show several Newtonian basic analyses with quadrupole approximation and briefly introduce some discussions about the effects of massive components and higher-order terms. Then the basic equations of the 1PN effect on the ZLK mechanism are introduced by using the simplest 1PN correction shown in §1.2.2. The main contents in this section follow Suzuki et al. (2021).

2.2.1 Newtonian Analysis

First I summarize important characteristics of the Newtonian ZLK mechanism. In this subsection, I mainly assume the restricted hierarchical triple system, where one of the components of the inner binary is treated as a test particle. I remark that the ZLK mechanism is seen not only in the restricted systems but also in the hierarchical triple systems with massive binary components. Although there exist some effects of the massive components on the ZLK mechanics as discussed in the last part of this subsection, the simple formulation obtained in the restricted hierarchical triple system is useful to understand the ZLK mechanics intuitively.

Here I mainly use the double-averaging method with quadrupole approximation introduced in §1.1.3. The effects of the higher-order terms in the multipole expansion are also discussed in the last part of this subsection.

Basic Equations in Quadrupole Approximation

First I show the basic equations of the ZLK mechanism obtained in the double-averaging method with quadrupole approximation for restricted triple systems. As in the discussions in §1.1.3, the reference plane is defined as the outer-orbital plane. Since the orbital elements of the outer orbit are assumed to be conserved in restricted triple systems, the outer inclination i_{out} vanishes and the relative inclination I just corresponds to the inner inclination i_{in}. The secular time evolutions of the osculating orbital elements of the inner orbit are described by the Lagrange planetary equations given in Eqs. (1.55) to (1.59).

The secular potential V_{s} given in Eq. (1.54) is divided into two components V_0 and v_{s} defined as

$$V_0 \equiv \frac{Gm_3 a_{\text{in}}^2}{16 a_{\text{out}}^3 (1 - e_{\text{out}}^2)^{3/2}}, \tag{2.1}$$

$$v_{\text{s}} \equiv (2 + 3e_{\text{in}}^2)(3\cos^2 I - 1) + 15 e_{\text{in}}^2 \cos 2\omega_{\text{in}} \sin^2 I. \tag{2.2}$$

The former component V_0 determines the magnitude of the secular potential. It does not change over time because the components in Eq. (2.1) are conserved in the double-averaging method as discussed in §1.1.3. The secular potential V_{s} is the conserved quantity and, therefore, the dimensionless part v_{s} should be also conserved.

For simplicity, here I introduce additional three dimensionless parameters:

$$\eta \equiv \sqrt{1 - e_{\text{in}}^2}, \tag{2.3}$$

$$\mu \equiv \cos I, \tag{2.4}$$

$$\tau \equiv \frac{V_0}{n_{\text{in}} a_{\text{in}}^2} t. \tag{2.5}$$

The dimensionless timescale τ is measured by the typical timescale of quadrupole interactions $n_{\mathrm{in}} a_{\mathrm{in}}^2 / V_0$ (see Eqs. (1.55) to (1.59)). The Lagrange equations for the eccentricity, the inclination, and the argument of periastron in Eqs. (1.56), (1.57) and (1.58) are rewritten with these dimensionless parameters as

$$\frac{d\eta}{d\tau} = \frac{\partial v_{\mathrm{s}}}{\partial \omega_{\mathrm{in}}}, \tag{2.6}$$

$$\frac{1}{\mu} \frac{d\mu}{d\tau} = -\frac{1}{\eta} \frac{\partial v_{\mathrm{s}}}{\partial \omega_{\mathrm{in}}}, \tag{2.7}$$

$$\frac{d\omega}{d\tau} = -\frac{\partial v_{\mathrm{s}}}{\partial \eta} + \frac{\mu}{\eta} \frac{\partial v_{\mathrm{s}}}{\partial \mu}. \tag{2.8}$$

From the above basic equations, the following two quantities are proved to be conserved:

$$\theta \equiv \eta\mu, \tag{2.9}$$

$$C_{\mathrm{ZLK}} \equiv (1-\eta^2)\left[1 - \frac{5}{2}(1-\mu^2)\sin^2 \omega_{\mathrm{in}}\right]. \tag{2.10}$$

The former quantity θ corresponds to the z-component of the angular momentum of the inner orbit and the latter one C_{ZLK} is obtained from the dimensionless potential v_{s}. From the three equations and the two conserved quantities, the evolutionary equation for η can be described with η itself and the two conserved quantities as

$$\frac{d\eta}{d\tau} = s\frac{12\sqrt{2}}{\eta}\sqrt{f(\eta)g(\eta)}, \tag{2.11}$$

where $s = -1$ for $\sin\omega\cos\omega > 0$ and $s = +1$ for $\sin\omega\cos\omega < 0$. The functions in the square root are defined as follows:

$$f(\eta) \equiv 1 - \eta^2 - C_{\mathrm{ZLK}}, \tag{2.12}$$

$$g(\eta) \equiv -5\theta^2 + (5\theta^2 + 3 + 2C_{\mathrm{ZLK}})\eta^2 - 3\eta^4. \tag{2.13}$$

Oscillations of Eccentricity and Inclination

The ZLK mechanism is characterized by the secular oscillation of the eccentricity and inclination, that is, the oscillation of η and μ. Due to the existence of the conserved value θ shown in Eq. (2.9), when one of η and μ evolves, the other one also evolves exchanging their values with each other to conserve the value of θ. I call the secular oscillations as "ZLK oscillation" in this thesis. If the ZLK oscillation occurs, η becomes maximum or minimum values when $d\eta/d\tau$ vanishes. From the evolutionary equation of η, Eq. (2.11), it occurs when $f(\eta)$ or $g(\eta)$ becomes zero. Since the value of $f(\eta)$ can be zero only when $C_{\mathrm{ZLK}} \geq 0$ for $0 < \eta \leq 1$, the ZLK oscillation is classified into the following two types: one is called *rotation* type, where $C_{\mathrm{ZLK}} \geq 0$, and the other is *libration* type, which has $C_{\mathrm{ZLK}} < 0$. The names of these two types come from the behaviors of the argument of periastron ω_{in} in these two types of the ZLK oscillation, which is explained in this subsection later.

The value of $f(\eta)$ become zero for

$$\eta = \eta_0 \equiv \sqrt{1 - C_{\mathrm{ZLK}}},\tag{2.14}$$

while $g(\eta)$ vanishes for

$$\eta = \eta_\pm \equiv \sqrt{\frac{5\theta^2 + 2C_{\mathrm{ZLK}} + 3 \pm \sqrt{(5\theta^2 + 2C_{\mathrm{ZLK}} - 3)^2 + 24C_{\mathrm{ZLK}}}}{6}}.\tag{2.15}$$

By considering the conditions $f(\eta)g(\eta) \geq 0$ for $0 < \eta \leq 1$, the range of η for each type of the ZLK oscillation is obtained as

$$\eta_- \leq \eta \leq \eta_0 \quad \text{for} \quad \text{rotation type} \,(C_{\mathrm{ZLK}} \geq 0),$$
$$\eta_- \leq \eta \leq \eta_+ \quad \text{for} \quad \text{libration type} \,(C_{\mathrm{ZLK}} < 0).$$

The above conditions for η give both the minimum and maximum values of the inner eccentricity $e_{\min}$ and $e_{\max}$. For rotation type $(C_{\mathrm{ZLK}} \geq 0)$, they are obtained as

$$e_{\min} = \sqrt{C_{\mathrm{ZLK}}},\tag{2.16}$$

$$e_{\max} = \sqrt{\frac{4C_{\mathrm{ZLK}}}{5\theta^2 + 2C_{\mathrm{ZLK}} - 3 + \sqrt{(5\theta^2 + 2C_{\mathrm{ZLK}} - 3)^2 + 24C_{\mathrm{ZLK}}}}},\tag{2.17}$$

while for libration type $(C_{\mathrm{ZLK}} < 0)$,

$$e_{\min} = \sqrt{\frac{4C_{\mathrm{ZLK}}}{5\theta^2 + 2C_{\mathrm{ZLK}} - 3 - \sqrt{(5\theta^2 + 2C_{\mathrm{ZLK}} - 3)^2 + 24C_{\mathrm{ZLK}}}}},\tag{2.18}$$

$$e_{\max} = \sqrt{\frac{4C_{\mathrm{ZLK}}}{5\theta^2 + 2C_{\mathrm{ZLK}} - 3 + \sqrt{(5\theta^2 + 2C_{\mathrm{ZLK}} - 3)^2 + 24C_{\mathrm{ZLK}}}}}.\tag{2.19}$$

By fixing θ^2 within $0 \leq \theta^2 \leq 1$, the maximum and minimum eccentricities of the ZLK oscillation Eqs. (2.16) to (2.19) can be calculated as the functions of C_{ZLK}. In Fig. 2.1, some examples of $e_{\min}$ and $e_{\max}$ for four different θ^2 are shown. One can find that the libration type of the ZLK oscillation does not appear when θ^2 becomes larger than the critical value, $\theta^2 = 0.6$. For the rotation types, on the other hand, θ^2 could reach almost unity but the oscillation amplitude becomes smaller and smaller as θ^2 becomes larger.

The constraints on the conserved quantities to have both the minimum and maximum values shown above are obtained from the condition $e_{\min} \leq e_{\max}$. For rotation type $(C_{\mathrm{ZLK}} \geq 0)$, the constraint for the ZLK oscillation is

$$\theta^2 \leq -C_{\mathrm{ZLK}} + 1,\tag{2.20}$$

and for libration type, it is obtained as

$$\theta^2 \leq \frac{1}{5}(-2C_{\mathrm{ZLK}} + 3 - 2\sqrt{-6C_{\mathrm{ZLK}}}).\tag{2.21}$$
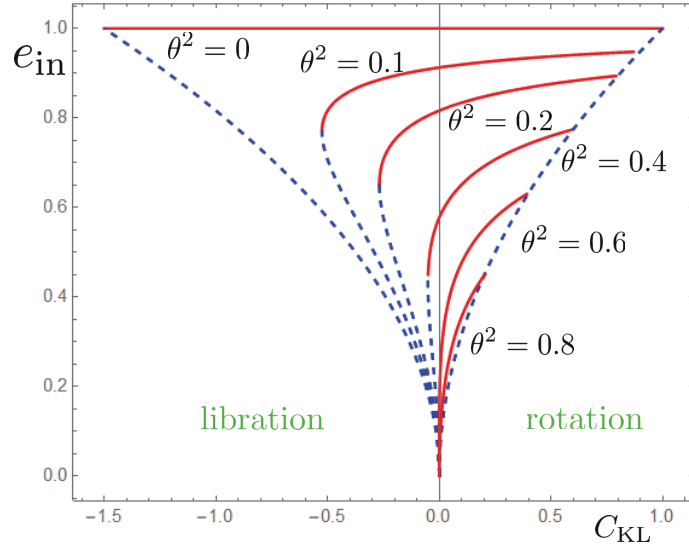
Figure 2.1:   Some examples of the maximum and minimum values of eccentricity in terms of C_{ZLK}. Note that C_{ZLK} defined in the text is denoted as C_{KL} in the figure. The red solid and blue dotted curves are the maximum and minimum values of the eccentricity, respectively. The four different $\theta^2 = 0.01, 0.2, 0.4, 0.6$, and 0.8 are chosen as the examples.
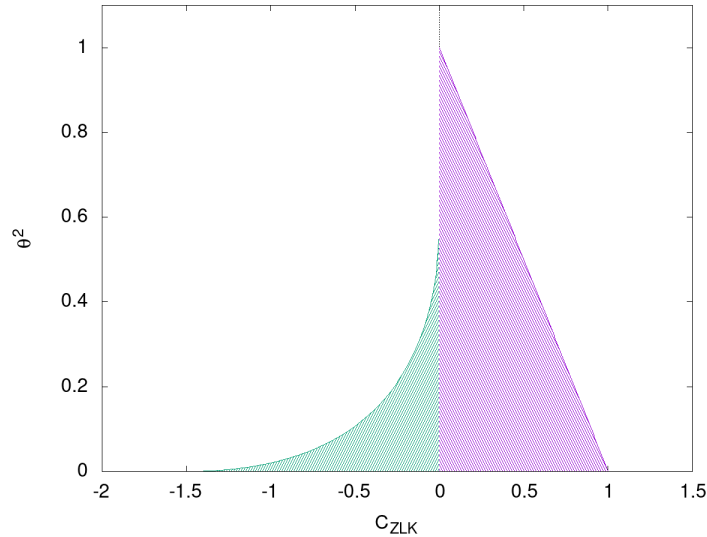

Figure 2.2:   The constraints on the two conserved values θ and C_{ZLK} where the ZLK mechanism occurs. The purple and green regions correspond to the parameter ranges for the rotation and libration types of the ZLK oscillation, respectively. Each parameter range is given in Eqs. (2.20) and (2.21). The same figure with different notation is in e.g. Antognini (2015).

The ranges of the conserved values where the ZLK oscillation is obtained are depicted in Fig. 2.2. The purple and green areas in the figure correspond to the parameter ranges for the rotation and libration types, which are described in Eqs (2.20) and (2.21), respectively. The same figure as Fig. 2.2 with a bit different notations is seen in e.g. Antognini (2015). On the boundary between the regions for rotation and libration types, one can find that the critical value of the libration type of θ^2 is 0.6, which is consistent with the results seen in Fig. 2.1. When the initial orbit is almost circular, Eq. (2.21) with $C_{ZLK} \approx 0$ and $\theta^2 = 0.6$ gives the well-known initial inclination range for the ZLK oscillation as

$$|\cos I_0| \leq \sqrt{\frac{3}{5}}, \tag{2.22}$$

where I_0 is the initial relative inclination.

The timescale of the ZLK oscillation (hereafter called ZLK timescale) T_{ZLK} is defined twice of the time for which the eccentricity changes from the minimum to the maximum values (Antognini, 2015). It is evaluated as

$$T_{ZLK} = \frac{n_{in}a_{in}^2}{V_0}(2\tau_{ZLK}), \tag{2.23}$$

where

$$\tau_{ZLK} = \int_{\eta_{\min}}^{\eta_{\max}} \left(\frac{d\eta}{d\tau}\right)^{-1} d\eta. \tag{2.24}$$

Since the order of τ_{ZLK} is about unity, the typical timescale of quadrupole interactions $n_{in}a_{in}^2/V_0$ can be used for a rough estimation of the ZLK timescale. It is calculated as

$$\tau_{ZLK} = \begin{cases} \dfrac{1}{12\sqrt{6(\eta_0^2-\eta_-^2)}} K\left(\sqrt{\dfrac{\eta_+^2-\eta_-^2}{\eta_0^2-\eta_-^2}}\right) & \text{for} \quad \text{rotation} \\[4ex] \dfrac{1}{12\sqrt{6(\eta_+^2-\eta_-^2)}} K\left(\sqrt{\dfrac{\eta_0^2-\eta_-^2}{\eta_+^2-\eta_-^2}}\right) & \text{for} \quad \text{libration}, \end{cases}$$

where $K(k)$ is the complete elliptic integral of the first kind with the modulus k. Fig. 2.3 shows τ_{KL} calculated as the function of θ^2 by fixing C_{ZLK} for several values.

Rotation and Libration of Argument of Periastron

The two types of the ZLK oscillations introduced in the former discussion are characterized by the behavior of the argument of periastron. It is clearly seen when the contours of C_{ZLK} are plotted as functions of ω_{in} and η^2 by fixing θ^2 in Eq. (2.10). One example with $\theta^2 = 0.250$ is plotted in Fig. 2.4. The contours correspond to the evolution curves of the eccentricity e_{in} and ω_{in} for given C_{ZLK}. One finds that there are some closed curves at the center of this plane, which means that the argument of periastron ω_{in} oscillates around 90° on these curves. Such behavior is called as libration of the periastron. These curves have $C_{ZLK} < 0$, which is classified as the libration type of the ZLK oscillation. On the other hand, the curves with
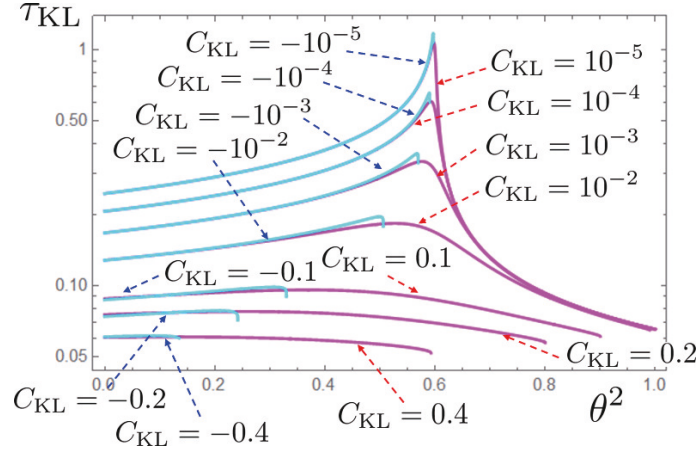
Figure 2.3: The dimensionless ZLK timescale τ_{ZLK} in terms of θ^2 is calculated by fixing C_{ZLK} for several values. Note that C_{ZLK} defined in the text is denoted as C_{KL} in the figure. The cyan and magenta curves correspond τ_{ZLK} calculated for the libration and rotation types of the ZLK oscillation, respectively.
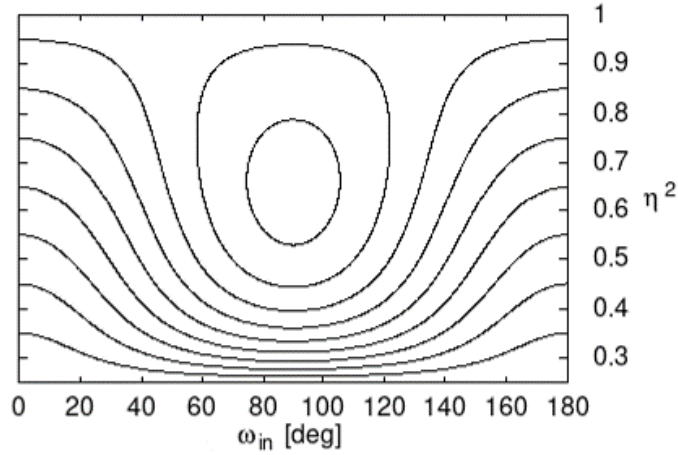

Figure 2.4: The contours of C_{ZLK} on ω_{in}-η^2 plane are plotted by fixing $\theta^2 = 0.250$. The contours are depicted every 0.1 for the range of $-0.15 \leq C_{\mathrm{ZLK}} \leq 0.75$. The libration type with $C_{\mathrm{ZLK}} < 0$ corresponds to the closed cycles at the center, while the lines of the rotation type go through the whole range of ω_{in}.
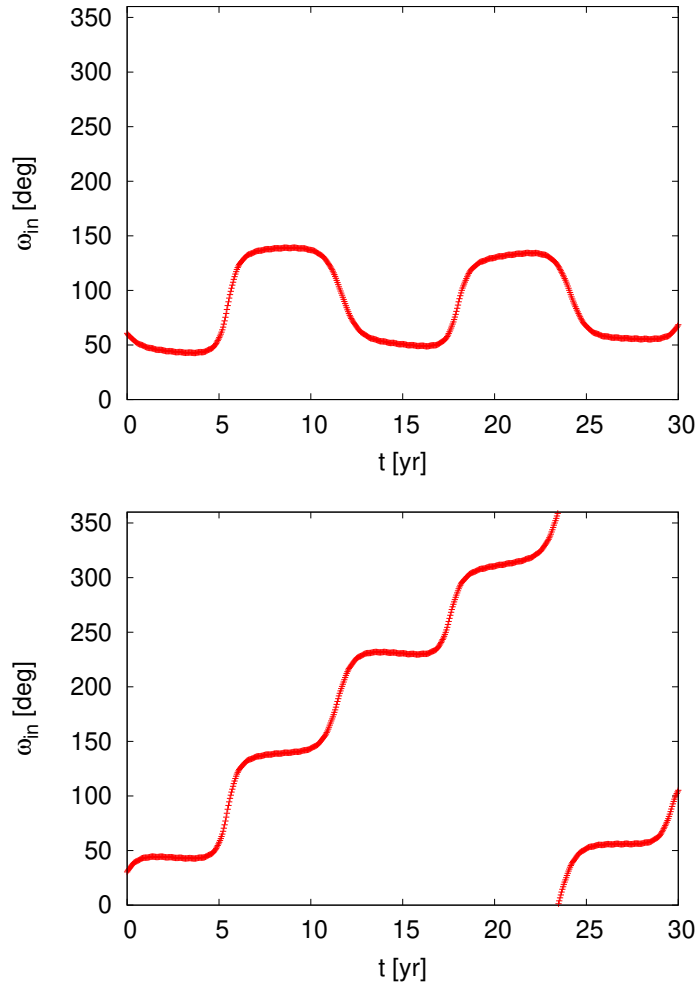
Figure 2.5:   Examples of the evolutions of the argument of periastron ω_{in} in libration (top panel) and rotation (bottom panel) types of ZLK oscillations. In these evolutions, $\theta^2 = 0.250$ for both types, and $C_{\mathrm{ZLK}} = -3.18 \times 10^{-5}$ for libration type, while for rotation type, it is 6.20×10^{-5}.

$C_{\mathrm{ZLK}} \geq 0$ are not closed and ω_{in} can go through the whole range on the curves. This means that the periastron point does not oscillate but rather rotates in the orbital evolution. Therefore, the ZLK oscillation with $C_{\mathrm{ZLK}} \geq 0$ is called the rotation type.

I show examples of the evolutions of the argument of periastron ω_{in} in the libration and rotation types of the ZLK oscillations in Fig. 2.5. The upper and lower panels show the evolutions of ω_{in} in the libration and rotation types, respectively. Both the libration and rotation behaviors of the periastron are clearly seen in the figure. The value of θ^2 is fixed as 0.250 for both types as in Fig. 2.4, and C_{ZLK} is set as -3.18×10^{-5} for libration type, while for rotation type, it is 6.20×10^{-5}. The examples calculated for Fig. 2.5 are the ICL and ICR types of the PNN model, which are defined in §2.3.3. See the subsection to check the detailed initial parameters of these calculations.

Effects of Massive Components and Higher-Order Terms

The above discussions assume one of the components of the inner binary is a test particle, that is, $m_2 \ll m_1, m_3$. Naoz et al. (2013a) pointed out that the secular potential $V_{\rm s}$ should be modified to consider the effect of massive m_2 and the deviation from the test-particle limit appears in the ZLK oscillations if the modified potential is used for the systems with $m_2 \sim m_1, m_3$. The effects of such "relaxing" of the test particle approximation were also discussed recently by Hamers (2021). The modified secular potential $V_{\rm s}^{\rm (m)}$ is described as

$$
\begin{aligned}
V_{\rm s}^{\rm (m)} &= \frac{V_0}{8} \Big[(1 + 3\cos(2i_{\rm out})) \big\{ (2 + 3e_{\rm in}^2)(1 + 3\cos(2i_{\rm in})) \\
&\quad + 30e_{\rm in}^2 \cos(2\omega_{\rm in}) \sin^2 i_{\rm in} \big\} + 3\cos(2\Delta\Omega) \big\{ 10e_{\rm in}^2 \cos(2\omega_{\rm in}) \\
&\quad \times (3 + \cos 2i_{\rm in}) + 4(2 + 3e_{\rm in}^2)\sin^2 i_{\rm in} \big\} \sin^2 i_{\rm in} \\
&\quad + 12\big\{ 2 + 3e_{\rm in}^2 - 5e_{\rm in}^2 \cos(2\omega_{\rm in}) \big\} \cos(\Delta\Omega) \sin(2i_{\rm in}) \sin(2i_{\rm out}) \\
&\quad + 120e_{\rm in}^2 \sin i_{\rm in} \sin(2i_{\rm out}) \sin(2\omega_{\rm in}) \sin(\Delta\Omega) \\
&\quad - 120e_{\rm in}^2 \cos i_{\rm in} \sin^2 i_{\rm out} \sin(2\omega_{\rm in}) \sin(2\Delta\Omega) \Big],
\end{aligned}
\tag{2.25}
$$

where $\Delta\Omega = \Omega_{\rm out} - \Omega_{\rm in}$ is the difference of the inner and outer longitudes of ascending node. Due to the additional terms depending on $\Delta\Omega$, the conserved quantities for the test-particle limit θ^2 and $C_{\rm ZLK}$ are no longer conserved. This means that the inner- and outer-orbital angular momenta are exchanging with each other because of the effect of the massive components in the inner binary. The amplitude and timescale of the ZLK oscillation are sensitive to the angular momentum of the inner orbit and sometimes large deviation from the test-particle limit appears as in Fig. 4 of Naoz et al. (2013a). In this chapter, the effects of the massive inner components are discussed in §2.4.

Even in the test-particle limit, the higher-order terms of the multipole expansion that are neglected in the above discussions sometimes give important effects on the ZLK oscillation. In Eq. (1.41), I explicitly wrote the expansion just up to quadrupole order. When the octupole order terms are also considered and the average is calculated, the secular potential becomes $V_{\rm s}^{\rm (oct)} = V_{\rm s} + V^{\rm (oct)}$, where

$$
\begin{aligned}
V^{\rm (oct)} &= \frac{15}{64} \frac{Gm_3(m_1 - m_2)a_{\rm in}^3}{(m_1 + m_2)a_{\rm out}^4(1 - e_{\rm out}^2)^{\frac{5}{2}}} e_{\rm in} e_{\rm out} \\
&\quad \times \Bigg[\Big\{ 4 + 3e_{\rm in}^2 - \frac{5}{2}\big(2 + 5e_{\rm in}^2 - 7e_{\rm in}^2 \cos(2\omega_{\rm in})\big) \sin^2 I \Big\} \\
&\quad \times \big(-\cos\omega_{\rm in}\cos\omega_{\rm out} - \cos I \sin\omega_{\rm in}\sin\omega_{\rm out} \big) \\
&\quad + 10(1 - e_{\rm in}^2)\cos I \sin^2 I \sin\omega_{\rm in}\sin\omega_{\rm out} \Bigg].
\end{aligned}
\tag{2.26}
$$

The octupole contribution $V^{\rm (oct)}$ depends on $e_{\rm out}$ and $\omega_{\rm out}$, which causes the exchange of the angular momenta between the inner and outer orbits. Due to the exchange of the angular momenta, in some limited configuration, the relative inclination I can evolve across $90°$, which is the boundary of prograde and retrograde orbits (see e.g.

Fig. 5 of Naoz (2016)). The evolution of I over the 90° boundary is called orbital flip. The ZLK mechanism that can make orbital flip is called the eccentric ZLK mechanism (Naoz, 2016) and it might work for the formation of exoplanets with retrograde orbits (Naoz et al., 2011, 2012). Recently, the effects of much higher-order terms have also been discussed as pointed out in §1.2.2. The effects of such higher-order terms are also discussed in §2.4 in this chapter.

2.2.2 1PN Corrections

Next, I summarize the effects of the 1PN corrections on the ZLK mechanism. For simplicity, here I use the simplest 1PN correction to the double-averaging method with the quadrupole approximation for the restricted triple systems, which is explained in §1.2.2. I remark that there are some discussions about the accuracy of the 1PN double-averaging method as introduced in the subsection. In §2.4, I revisit this point comparing the results obtained from direct integration and the basic features obtained in this subsection.

The simplest 1PN correction for the double-averaging method is obtained by just replacing $V_{\rm s}$ with $V_{\rm s}^{\rm (1PN)}$ as shown in §1.2.2. As in the Newtonian discussion, the secular potential is divided into the dimensionful part V_0 given in Eq. (2.1) and the dimensionless part $v_{\rm s}^{\rm (1PN)}$ defined as

$$v_{\rm s}^{\rm (1PN)} \equiv v_{\rm s} + 12 \frac{\epsilon^{\rm (1PN)}}{\eta}, \tag{2.27}$$

where $\epsilon^{\rm (1PN)}$ is a dimensionless parameter of the 1PN correction defined as

$$\epsilon^{\rm (1PN)} \equiv 4 \frac{r_{\rm g,in}}{a_{\rm in}} \frac{m_1 + m_2}{m_3} \left(\frac{a_{\rm out}}{a_{\rm in}} \right)^3 (1 - e_{\rm out}^2)^{\frac{3}{2}}. \tag{2.28}$$

The distance $r_{\rm g,in} \equiv G(m_1 + m_2)/c^2$ in the above description is a gravitational scale of the total mass of the inner binary. By replacing $v_{\rm s}$ in basic equations Eqs. (2.6) to (2.8) with $v_{\rm s}^{\rm (1PN)}$, one can find the two conserved quantities θ and $C_{\rm ZLK}^{\rm (1PN)}$ as in the Newtonian analysis: θ is the same as the Newtonian definition in Eq. (2.9) while $C_{\rm ZLK}^{\rm (1PN)}$ is defined with 1PN correction as

$$C_{\rm ZLK}^{\rm (1PN)} \equiv C_{\rm ZLK}(\eta, \mu, \omega) + \epsilon^{\rm (1PN)} \left(\frac{1 - \eta}{\eta} \right). \tag{2.29}$$

Note that $C_{\rm ZLK}(\eta, \mu, \omega)$ is not conserved with the 1PN correction. The three basic equations and the existence of two conserved quantities give a single evolutionary equation for η as

$$\frac{d\eta}{d\tau} = -\frac{12\sqrt{2}}{\eta} \sqrt{f^{\rm (1PN)}(\eta) g^{\rm (1PN)}(\eta)}, \tag{2.30}$$

where

$$f^{\rm (1PN)} = 1 - \eta^2 - C_{\rm ZLK}^{\rm (1PN)} + \epsilon^{\rm (1PN)} \left(\frac{1 - \eta}{\eta} \right), \tag{2.31}$$

$$g^{\rm (1PN)} = -5\theta^2 + \left(5\theta^2 + 3 + 2C_{\rm ZLK}^{\rm (1PN)} \right) \eta^2 - 3\eta^4 - 2\epsilon^{\rm (1PN)}\eta (1 - \eta). \tag{2.32}$$
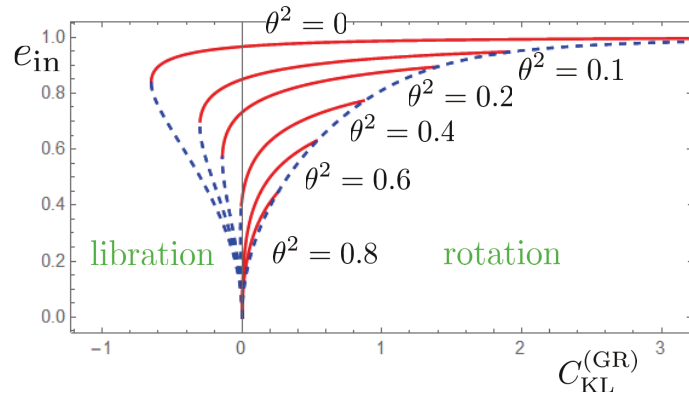
Figure 2.6:   The maximum and minimum eccentricities of the ZLK oscillation calculated with the 1PN correction. Note that $C_{\mathrm{ZLK}}^{(1\mathrm{PN})}$ defined in the text is denoted as $C_{\mathrm{KL}}^{(\mathrm{GR})}$ in the figure. The libration region exists only for $\theta^2 < (3 - \epsilon^{(1\mathrm{PN})})/5$. The value of $\epsilon^{(1\mathrm{PN})}$ is fixed as 0.484, the value of one of the PNIB model shown in §2.3.3.

If the ZLK oscillation occurs, when the time derivative of η vanishes, the value of η becomes maximum or minimum. Hence maximum and minimum eccentricities can be investigated by looking for η that makes $f^{(1\mathrm{PN})}$ or $g^{(1\mathrm{PN})}$ vanish under the conditions $f^{(1\mathrm{PN})}g^{(1\mathrm{PN})} \geq 0$ and $0 < \eta \leq 1$. It can be proved that the cubic equation $\eta f^{(1\mathrm{PN})} = 0$ has one root only when $C_{\mathrm{ZLK}}^{(\overline{1\mathrm{PN}})} \geq 0$. Therefore, just as in the Newtonian case, the 1PN ZLK oscillation is classified into the following two types: one is the rotation type with $C_{\mathrm{ZLK}}^{(1\mathrm{PN})} \geq 0$ and the other is the libration type with $C_{\mathrm{ZLK}}^{(1\mathrm{PN})} < 0$.

As in the Newtonian discussion, the maximum and minimum eccentricities can be calculated when the two conserved quantities θ and $C_{\mathrm{ZLK}}^{(1\mathrm{PN})}$, and the 1PN parameter $\epsilon^{(1\mathrm{PN})}$ are fixed. Fig. 2.6 shows the maximum and minimum eccentricities as the functions of $C_{\mathrm{ZLK}}^{(1\mathrm{PN})}$ by fixing $\epsilon^{(1\mathrm{PN})} = 0.484$ and θ for several values. The value of $\epsilon^{(1\mathrm{PN})} = 0.484$ is obtained for the PNIB model, one of the models explained in §2.3.3. The libration region exists only for $\theta^2 < (3 - \epsilon^{(1\mathrm{PN})})/5$ in this figure. The shape of the curves in Figs. 2.1 and 2.6 are similar but the parameter region of the two conserved quantities where the ZLK oscillation occurs is different. In order to clarify this point, in Fig. 2.7, the maximum and minimum eccentricities with $\theta^2 = 0.1$ calculated in the Newtonian and 1PN formulae are compared. The 1PN parameter $\epsilon^{(1\mathrm{PN})}$ is fixed as 0.484. One finds that, in the libration type, the 1PN effect suppresses the ZLK oscillation, that is, the parameter region of $C_{\mathrm{ZLK}}^{(1\mathrm{PN})}$ where the oscillation occurs is reduced and the oscillation amplitude becomes smaller for the given value of $C_{\mathrm{ZLK}}^{(1\mathrm{PN})}$. For the rotation type, on the other hand, the parameter region of $C_{\mathrm{ZLK}}^{(1\mathrm{PN})}$ increases, and the amplitude of the eccentricity does not always become smaller for given $C_{\mathrm{ZLK}}^{(1\mathrm{PN})}$.

The suppression of the ZLK oscillation for the libration type has been discussed by several authors (e.g. Blaes et al. (2002); Anderson et al. (2017)) and they found the critical value of the 1PN parameter $\epsilon_{\mathrm{cr}}^{(1\mathrm{PN})} = 3(1 - e_{\mathrm{in}}^2)^{3/2}$ with which the maximum and minimum eccentricities of the inner orbit become equal. When the 1PN parameter $\epsilon^{(1\mathrm{PN})}$ is larger than the critical value, the libration type of the ZLK oscillation does not occur. The condition for the stable ZLK oscillations ($\epsilon^{(1\mathrm{PN})} < \epsilon_{\mathrm{cr}}^{(1\mathrm{PN})}$)
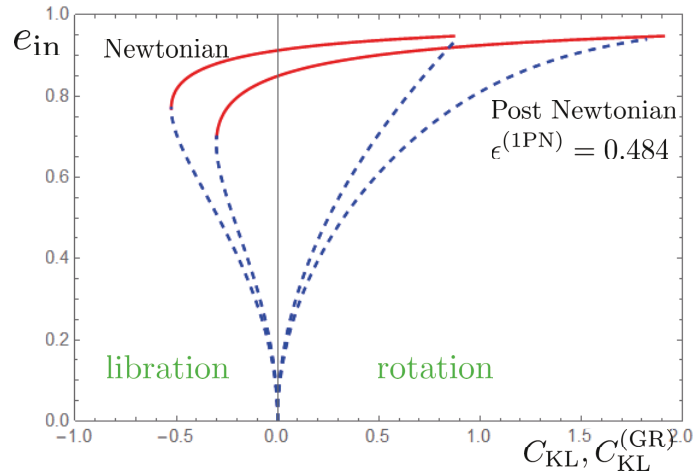
Figure 2.7:   Comparison between the Newtonian and 1PN results with $\epsilon^{(\mathrm{1PN})} = 0.484$. Here θ^2 is fixed as 0.1. Note that C_{ZLK} and $C_{\mathrm{ZLK}}^{(\mathrm{1PN})}$ defined in the text are denoted as C_{KL} and $C_{\mathrm{KL}}^{(\mathrm{GR})}$ in the figure, respectively.

is rewritten with orbital parameters as

$$\frac{r_{\mathrm{g,in}}}{a_{\mathrm{in}}} \frac{m_1 + m_2}{m_3} \left(\frac{a_{\mathrm{out}}}{a_{\mathrm{in}}} \right)^3 \frac{(1 - e_{\mathrm{out}}^2)^{3/2}}{(1 - e_{\mathrm{in}}^2)^{3/2}} < \frac{3}{4}. \tag{2.33}$$

The ZLK timescale with the 1PN correction can be evaluated in the same way as the Newtonian one. The 1PN ZLK timescales are almost the same as the Newtonian ones but can be slightly different. The small difference complicatedly depends on the parameters of the system, so I avoid explaining in detail here but discuss later in §2.4 with the simulation results.

2.3   Application to Pulsar Observation

I focus on the GW emission effects on the CSPT of the inner binary of the hierarchical triple system where the ZLK mechanism occurs. The CSPT is observable if the system has a pulsar as a component of the inner binary. In this chapter, hence, I calculate orbital evolutions and the CSPT numerically for such triple systems and discuss how the ZLK effects are observed in the CSPT curves.

In this section, first I explain the numerical method to calculate the orbital evolutions and the basic equations to calculate the CSPT. Then I show an example by using the parameters of an observed binary pulsar. Subsequently, various models with a pulsar as a component of the inner binary are introduced and the parameter space for observability is discussed.

2.3.1   Method

Numerical Simulation of Orbital Evolution

In this chapter, the method to calculate the orbital motion of the relativistic hierarchical triple systems considering the 1PN effects is explained. As mentioned in
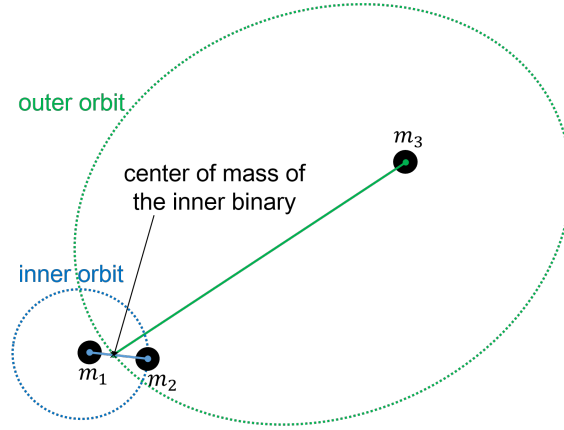
Figure 2.8:   The schematic picture of a hierarchical triple system. The orbit of star 2 (whose mass is m_2) around star 1 (whose mass is m_1) is denoted as inner orbit and the trajectory of the center of mass of the inner binary around the third star (whose mass is m_3) is the outer orbit. The outer semi-major axis a_{out} is assumed to be much larger than the inner one a_{in}.

§1.2.2, I directly integrate the equations of motion Eq. (1.159) to avoid the difficulty of the double-averaging method. Here I explain how the initial coordinates are made from orbital parameters, how the equations of motion are integrated, and how the obtained results are analyzed.

First, I introduce the process to obtain the initial coordinates from the values of orbital elements. The models in this research were characterized by the Kepler elements introduced in §1.1.1 for the inner and outer orbits. As for the outer orbit, the center of mass of the inner binary rotating around the third body is pursued as in the schematic picture in Fig. 2.8. In order to calculate the equations of motion, the orbital elements should be transformed to the Cartesian coordinates of the constituent bodies. As a first step, the eccentric anomaly u is obtained from the mean anomaly M by solving Eq. (1.15) with the Newton-Raphson method. Then the true anomaly f is obtained by using the relations in Eqs. (1.10) and (1.11). The polar coordinates of an orbiting body measured from its companion are described in terms of the true anomaly and other orbital elements as

$$r = \frac{a(1-e^2)}{1-e\cos f}, \tag{2.34}$$

$$\psi = \Omega + \arctan\{\tan(\omega + f)\cos i)\}, \tag{2.35}$$

$$\theta = \arccos\{\sin(\omega + f)\sin i\}. \tag{2.36}$$

The origin of these coordinates is on the companion of the orbiting object: in the hierarchical triple system in Fig. 2.8, the origin is on star 1 and the orbiting object is star 2 for the inner orbit, while, for the outer orbit, the origin is at the position of the third body and orbiting object is the center of mass of the inner binary. The time derivatives of the polar coordinates are obtained as

$$\dot{r} = g_r \dot{f}, \tag{2.37}$$

$$\dot{\theta} = g_\theta \dot{f}, \tag{2.38}$$

$$\dot{\psi} = g_\psi \dot{f}, \tag{2.39}$$

where g_r, g_θ, g_ψ, and $\dot{f}$ are described as

$$g_r = \frac{a(1-e^2)e\sin f}{(1+e\cos f)^2}, \tag{2.40}$$

$$g_\theta = -\frac{1}{\sin\theta}\cos\left(\omega+f\right)\sin i, \tag{2.41}$$

$$g_\psi = \cos^2(\psi-\Omega)\frac{\cos i}{\cos^2(\omega+f)}, \tag{2.42}$$

$$\dot{f} = \sqrt{Gm'\left(\frac{2}{r}-\frac{1}{a}\right)\frac{1}{g_r^2+(rg_\theta)^2+(r\sin\theta g_\psi)^2}} . \tag{2.43}$$

The mass m' is the total mass of the binary, that is, in the hierarchical triple system, $m' = m_1 + m_2$ for the inner orbit while $m' = (m_1 + m_2) + m_3$ for the outer orbit. These positions and velocities in the polar coordinates are transformed to be written in the Cartesian coordinates. The origins of the coordinates for both the inner and outer orbits are shifted to the center of mass of the entire system, and the coordinates are rotated to set the x-y plane as the initial outer-orbital plane. The integration of the equations of motion uses the initial conditions so obtained in the Cartesian coordinates.

The equations of motion are integrated by using the sixth order implicit Runge-Kutta method. The implicit Runge-Kutta method is one of the symplectic methods, in which the conservation of Hamiltonian is guaranteed. When applied to $dx/dt = f(t, x)$, it advances the time step from n to $n+1$ according to the following equations:

$$\xi_i = x_n + h\sum_{j=1}^{s} A_{ij}f(\tilde{t}_n^j, \xi_j), \tag{2.44}$$

$$x_{n+1} = y_n + h\sum_{i=1}^{s} B_i f(\tilde{t}_n^i + C_j h, \xi_i). \tag{2.45}$$

In the above equations, x_n and x_{n+1} are the values of the solution at the n- and $(n+1)$-th time steps, respectively. The positive value h is the corresponding time interval and ξ_i ($i = 1, ..., s$) is the value of x at the i-th intermediate time $\tilde{t}_n^i = t_n + C_i h$. The implicit-Runge-Kutta method is specified by the number of stages s and the coefficients A_{ij}, B_i, and C_i are given according to s. Here I use the three-stage and sixth-order accurate scheme, which is also referred to as the Kuntzmann & Butcher method (Butcher, 1964). The coefficients used in the scheme are described as

$$A = \begin{pmatrix} \frac{5}{36} & \frac{2}{9}-\frac{\sqrt{15}}{15} & \frac{5}{36}-\frac{\sqrt{15}}{30} \\ \frac{5}{36}+\frac{\sqrt{15}}{24} & \frac{2}{9} & \frac{5}{36}-\frac{\sqrt{15}}{24} \\ \frac{5}{36}+\frac{\sqrt{15}}{30} & \frac{2}{9}+\frac{\sqrt{15}}{15} & \frac{5}{36} \end{pmatrix}, \tag{2.46}$$

$$B = \begin{pmatrix} \frac{5}{18} & \frac{4}{9} & \frac{5}{18} \end{pmatrix}, \tag{2.47}$$

$$C = \left(\frac{1}{2} - \frac{\sqrt{15}}{10} \quad \frac{1}{2} \quad \frac{1}{2} + \frac{\sqrt{15}}{10} \right). \tag{2.48}$$

In this research, both the Newtonian and 1PN equations of motion are numerically integrated and the results are compared. Note that the back reaction of the GW emission to the orbital evolution corresponding to the 2.5PN terms is neglected in the integration of the equations of motion because the effects of back reaction on a few ZLK timescales are negligibly small. It is important that the GW emission effects are so small that cannot be seen in the orbital evolution but could be observed in the CSPT. I revisit this point in the explanation of the calculation of the CSPT soon.

The position and velocities obtained at each timestep is again transformed to the osculating orbital elements to analyze the results. The semi-major axis a, eccentricity e, inclination i, and longitude of ascending node Ω are calculated by using Eqs. (1.6), (1.4), (1.7), and (1.8), respectively. The relative inclination I at each timestep is also calculated by substituting i and Ω in Eq. (1.53). The argument of periastron ω defined in Eq. (1.9) is calculated by following two steps: first, the true anomaly f is calculated by using Eq. (1.5) as

$$f = \arccos \left(\frac{a(1 - e^2) - r}{er} \right); \tag{2.49}$$

secondly, the angle of the planet measured from the ascending node θ is calculated as

$$\theta = \arccos \left(\frac{x \cos \Omega + y \sin \Omega}{|\boldsymbol{r}|} \right); \tag{2.50}$$

finally, the argument of periastron ω is obtained by calculating the difference of these arguments as

$$\omega = \theta - f. \tag{2.51}$$

Due to the effect of the third body, the trajectory of the inner orbit is not exactly a closed ellipse, that is, the osculating orbital elements fluctuate with small amplitudes. This small oscillation with the period of the inner orbit is not essential but seems to be rather artificial. Hence, in this research, an average of these elements for each inner cycle is calculated to extract the effective values of the inner orbital elements at each cycle. Hereafter the averaged elements are described with a bar, e.g., $\bar{a}_{\text{in}}$ and $\bar{e}_{\text{in}}$. Those effective inner orbital elements evolve on a secular timescale due to the effect of the third body.

Cumulative Shift of Periastron Time

If the inner orbit is close enough, its orbital energy is gradually extracted by the GW emission. When the orbital energy is dissipated, the orbit shrinks and then the orbital period is shortened. Peters and Mathews (1963) derived a well-known

formula of the period change for each orbital cycle as

$$\dot{P}_{\text{in}} = -\frac{192\pi}{5} \left(\frac{P_{\text{in}}}{2\pi}\right)^{-\frac{5}{3}} \frac{G^2 m_1 m_2}{c^5} \{G(m_1 + m_2)\}^{-\frac{1}{3}}$$
$$\times \frac{1}{(1 - \bar{e}_{\text{in}}^2)^{\frac{7}{2}}} \left(1 + \frac{73}{24}\bar{e}_{\text{in}}^2 + \frac{37}{96}\bar{e}_{\text{in}}^4\right), \tag{2.52}$$

where P_{in} is the orbital period of the inner binary described as

$$P_{\text{in}} = 2\pi \sqrt{\frac{\bar{a}_{\text{in}}^3}{G(m_1 + m_2)}}. \tag{2.53}$$

In this estimation, the orbital elements are assumed to be constant for one orbital cycle, that is, the back reaction of the GW emission is assumed to be negligibly small on such a short timescale. Therefore, the averaged orbital elements are used in the above formula to reflect the effective shape of the orbit for one cycle. On a few ZLK timescales, if the system is an isolated binary without the third body, changes in orbital elements due to the GW emission are small enough to assume that $\dot{P}_{\text{in}}$ is constant. If the ZLK mechanism occurs because of the existence of the third body, however, the secular evolution of the eccentricity cannot be neglected on a few ZLK timescales and $\dot{P}_{\text{in}}$ changes with time.

Since the period change due to the GW emission is quite small and difficult to observe directly, it is convenient to introduce a new variable called the cumulative shift of periastron time (CSPT). In observation, this value can be obtained through radio signals from a binary pulsar just as the observation of the Hulse-Taylor binary (Weisberg and Taylor, 2005). In this research, the analysis of the CSPT that has been done for isolated binary pulsars is expanded for hierarchical triple systems whose inner binaries contain a pulsar. The CSPT is defined as the accumulation of the shift of the periastron passage timing, that is, the CSPT of the inner binary of the hierarchical triple system, Δ_P, is given as

$$\Delta_P(T_N) = T_N - P_{\text{in}}(0)N, \tag{2.54}$$

where T_N is the N-th periastron passage time and $P_{\text{in}}(0)$ is the initial value of the inner orbital period. From the definition of T_N, N can be described as

$$N = \int_0^{T_N} \frac{1}{P_{\text{in}}(t)} \mathrm{d}t, \tag{2.55}$$

where $P_{\text{in}}(t)$ is the orbital period at time t, which is gradually shortened by the GW emission as

$$P_{\text{in}}(t) = P_{\text{in}}(0) + \int_0^t \dot{P}_{\text{in}}(t') \mathrm{d}t'. \tag{2.56}$$

By substituting Eqs. (2.55) and (2.56) into Eq. (2.54), the CSPT Δ_P is described as

$$\begin{aligned} \Delta_P(T_N) &= T_N - \int_0^{T_N} \mathrm{d}t \frac{P_{\text{in}}(0)}{P_{\text{in}}(0) + \int_0^t \dot{P}_{\text{in}}(t')\mathrm{d}t'} \\ &= \int_0^{T_N} \mathrm{d}t \frac{\int_0^t \dot{P}_{\text{in}}(t')\mathrm{d}t'}{P_{\text{in}}(0) + \int_0^t \dot{P}_{\text{in}}(t')\mathrm{d}t'}. \end{aligned} \tag{2.57}$$

The period change due to the GW emission is usually quite small for binary pulsars and one can expect the following condition:

$$\left| \int_0^t \dot{P}_{\text{in}}(t') \mathrm{d}t' \right| \ll P_{\text{in}}(0). \tag{2.58}$$

In fact, for the Hulse-Taylor binary pulsar (Weisberg and Taylor, 2005), the binary period P_b and the period change rate $\dot{P}_b$ is given as

$$
\begin{aligned}
P_{\text{b}} &= 0.32299 \text{ day}, \tag{2.59}\\
\dot{P}_{\text{b}} &= -2.4184 \times 10^{-12} \text{ s/s}, \tag{2.60}
\end{aligned}
$$

which means that the condition given in Eq. (2.58) is true if $t \ll 3.7 \times 10^8$ yrs. In this research, just a few ZLK timescales are calculated and the timescale satisfies $T_N \ll 10^8$ yrs. This is nothing but the reason why I do not consider 2.5PN terms in the equations of motion. Hence Δ_P is approximated as

$$\Delta_P(T_N) \approx \frac{1}{P_{\text{in}}(0)} \int_0^{T_N} \mathrm{d}t \int_0^t \mathrm{d}t' \dot{P}_{\text{in}}(t'). \tag{2.61}$$

Here I remark that if $\dot{P}_{\text{in}}(t)$ is assumed to be almost constant, that is, $\dot{P}_{\text{in}}(t) \approx \dot{P}_{\text{in}}(0)$, Δ_P is described as

$$\Delta_P(T_N) \approx \frac{\dot{P}_{\text{in}}(0)}{2P_{\text{in}}(0)} T_N^2, \tag{2.62}$$

which corresponds to the formula used for the Hulse-Taylor binary in Weisberg and Taylor (2005). In a hierarchical triple system with the ZLK mechanism, $\dot{P}_{\text{in}}(t)$ cannot be treated as a constant and its evolution should be considered by calculating Eq. (2.61) with Eq. (2.52) instead of Eq. (2.62).

This formulation of the CSPT can be applied to a general stable three-body (or N-body) system with a binary pulsar as long as the condition Eq. (2.58) is satisfied. The CSPT is the accumulated effect and the feature makes it possible to observe it through long-term detection of radio signals from binary pulsars even for such weak GW emission that the back reaction of GW emission on the orbital elements is negligibly small. The CSPT observation from a binary pulsar in a triple system may be the precursor of the detection of GW from a triple system with the ZLK mechanism (Hoang et al., 2019; Randall and Xianyu, 2019; Deme et al., 2020; Gupta et al., 2020).

2.3.2 Example for Three-Body Model with PSR J1840-0643

In this subsection, I show an example of the calculation of the CSPT following Suzuki et al. (2019). I use the parameters of the PSR J1840-0643 system as the binary pulsar in the triple-system models. This binary pulsar was discovered in the *Einstein@Home* project. The detail about the project and the orbital parameters of the binary pulsar are given in Knispel et al. (2013).

From the observation of radio signals from binary pulsars, the constraint on the presence of a third body orbiting around the binary can be given with the

orbit	a[au]	e	i[deg]	Ω[deg]	ω[deg]	M[deg]
inner	2.17373	0	60	0	-	0
outer	20.0	0	0	0	-	20

Table 2.1: Initial orbital elements of a model with the PSR J1840-0643 system. The masses are $m_1 = 1.4\,\mathrm{M_\odot}, m_2 = 0.16\,\mathrm{M_\odot}$ and $m_3 = 30\,\mathrm{M_\odot}$, respectively. The parameters of the inner orbit are fixed by the observational data, whereas those of the outer orbit are just assumptions. The argument of periastron ω cannot be defined because the eccentricity is zero. The degree of freedom has been instead used to fix the axis of the reference frame.

Doppler shift effect. In the radio signals, the Doppler shift effect by the acceleration due to the third body degenerates with the spin-down effect of the pulsar. These effects degenerate in the characteristic age of pulsar $\tau_\nu = \nu/(2|\dot{\nu}|)$, where $\nu(t)$ is the effective spin frequency of the pulsar. The Doppler time-scale $\tau_\mathrm{D} \sim ca_\mathrm{out}^2 G^{-1} m_3^{-1}$ should be longer than the characteristic age of the pulsar τ_ν, which gives the upper limit for the mass of the third body and its distance. For the Hulse-Taylor binary pulsar, $\tau_\nu \approx 2 \times 10^7$ yrs and the presence of a third stellar-mass object within $a_\mathrm{out} < 100\,\mathrm{au}$ was ruled out by comparing τ_D and τ_ν (Smarr and Blandford, 1976). The characteristic age of the PSR J1840-0643 system is estimated as $\tau_\nu = 2.56 \times 10^6$ yrs and it seems that this system also has a strict constraint on the presence of a third body like the Hulse-Taylor binary. However, this characteristic age was evaluated in the topocentric frame by assuming that this system is an isolated binary, and when it is evaluated in the barycentric frame, the spin period seems to be increasing, which looks unphysical (Knispel et al., 2013). Hence, here I assess that this system has not yet had a strict constraint on the presence of a third body and calculate the evolution of the system by assuming the presence of the third body.

The orbital parameter of a model with PSR J1840-0643 is in Table 2.1. The parameters of the inner binary are obtained from the observed data of the PSR J1840-0643 system. The masses of the components of the inner binary are $m_1 = 1.4\,\mathrm{M_\odot}$ and $m_2 = 0.16\,\mathrm{M_\odot}$, respectively. In this model, the mass of the third body is assumed to be $m_3 = 30\,\mathrm{M_\odot}$, and the outer-orbital semi-major axis a_out and the relative inclination I are set as 20.0 au and 60°, respectively. These parameters satisfy the condition for the ZLK mechanism introduced in §2.2.

The results of the calculations of the orbital evolution and the CSPT curve for this model are shown in Figs. 2.9 and 2.10. Fig. 2.9 shows the evolutions for 100 yrs of the averaged inner eccentricity $\bar{e}_\mathrm{in}$, relative inclination $\bar{I}$, and conserved quantity of ZLK mechanism $\bar{\theta}^2$ defined in Eq. (2.9), which is referred as $\bar{\Theta}$ in the figure. In the evolutions of $\bar{e}_\mathrm{in}$ and $\bar{I}$, the two kinds of oscillations with different timescales are seen: one is the oscillation with outer-orbital orbit $P_\mathrm{out} = 15.92$ yrs, and the other is the ZLK oscillation whose timescale is about 100 yrs. The former rapid oscillation with the outer-orbital period was also found in some papers (Ivanov et al., 2005; Katz and Dong, 2012; Antognini et al., 2014; J and Wegg, 2014). In the latter ZLK oscillation, the effective eccentricity increases from 0 to about 0.6 while the effective inclination decreases from 60° to about 48°. The ZLK timescale can be roughly estimated as $T_\mathrm{ZLK} \sim n_\mathrm{in} a_\mathrm{in}^2 / V_0$ and is calculated with the parameters in Table 2.1 as
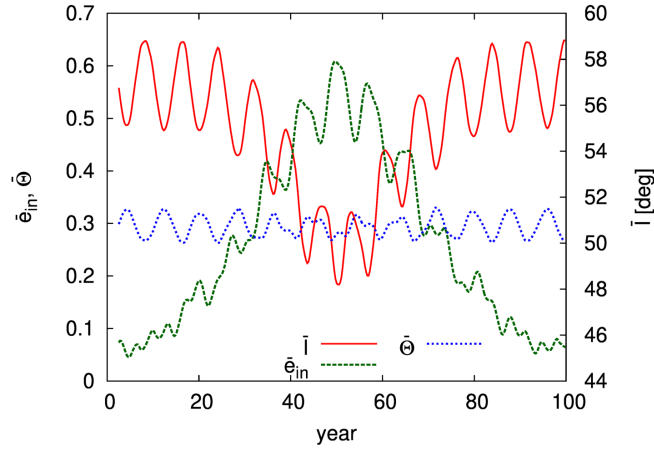
Figure 2.9:   The evolutions of the averaged inner eccentricity $\bar{e}_{\mathrm{in}}$, relative inclination $\bar{I}$ and the conserved quantity of the ZLK mechanism $\bar{\Theta} = \bar{\theta}^2$ for 100 yrs. The red, green, and blue lines describe the evolution of $\bar{e}_{\mathrm{in}}$, $\bar{I}$, and $\bar{\Theta}$, respectively.
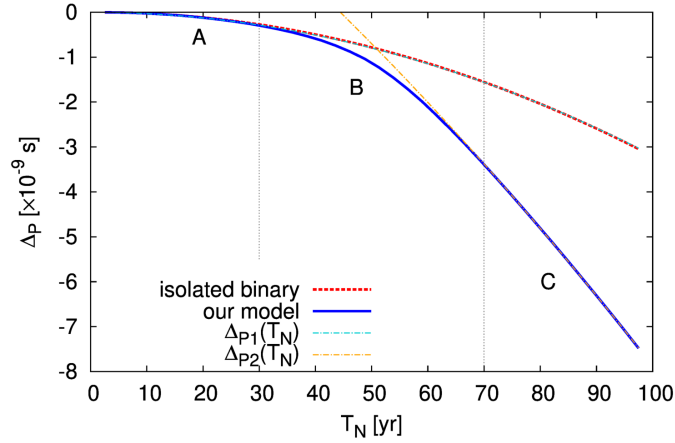

Figure 2.10:   The CSPT Δ_P is calculated for 100 yrs. The blue solid and red dotted lines are the CSPT curves for the inner binary of the three-body model and the isolated binary, respectively. The cyan and orange dashed lines correspond to quadratic functions given as $\Delta_{P1}(T_N)$ and $\Delta_{P2}(T_N)$ in the text. The blue line is initially overlapped with the red and cyan line in Period A, but show deviation in Period B, and fitted by different quadratic curve shown as the orange line in Period C. Detail explanations about the figure is in the text.

$T_{\mathrm{ZLK}} \sim 104$ yrs, which is consistent with the result of the simulation. I remark that $\bar{\Theta}$ is approximately but not exactly conserved and it shows small oscillation with the outer-orbital period P_{out} around $\bar{\Theta} = 0.3$. This may be caused by the effect of massive m_2 discussed in §2.2. The fluctuation in $\bar{\Theta}$ is consistent with the deviation from the ideal restricted triple system discussed in Naoz et al. (2013a).

Fig. 2.10 exhibits the evolution of the CSPT Δ_P for 100 yrs. The CSPT curve of the triple-system model is shown by the blue solid line, and, as a reference, that of an isolated binary without the third body calculated in the same way is also shown by the red dotted line. By using Eq. (2.62), the CSPT of the isolated binary is approximately described by the quadratic function as

$$\Delta_{P1}[\mathrm{s}] = -3.185 \times 10^{-13} \left(T_N[\mathrm{yrs}] \right)^2 , \qquad (2.63)$$

which is shown in Fig. 2.10 as a cyan dashed line. One finds that the red line for the isolated binary is completely overlapped with the cyan line in the figure. In Fig. 2.10, The CSPT curve of the triple system (blue line) coincides with that of the isolated binary (red line) initially in Period A, but it starts to deviate at $t \sim 30$ yrs and the discrepancy between these two lines becomes larger until $t \sim 60$ yrs in Period B. In Period B, the inner eccentricity is excited by the ZLK mechanism seen in Fig. 2.9. Hence the deviation in the CSPT curves is caused by the enhancement of the GW emission due to the large eccentricity obtained from the ZLK mechanism. After $t \sim 70$ yrs, in Period C, the eccentricity decreases again as seen in Fig. 2.9, and then Δ_P is approximated by another quadratic function

$$\Delta_{P2}[\mathrm{s}] = -3.185 \times 10^{-13} \left(T_N[\mathrm{yrs}] + 1.501 \times 10^2 \right)^2 + 1.206 \times 10^{-8}, \qquad (2.64)$$

whose curve is also given in the figure as an orange dashed line. As a result, I conclude that the CSPT curve bends when the eccentricity is excited by the ZLK mechanism.

If the ZLK mechanism occurs in triple systems with binary pulsars, it should be found first by the observation of the orbital elements themselves, not from the observation of the CSPT, as pointed out by (Gopakumar et al., 2009; Zwart et al., 2011). Hence the observation of the CSPT may not be quite important from the perspective of the confirmation of the presence of the third body, but it is important to discover the GW from a three-body system.

Furthermore, the feature of the CSPT curve may be useful for real pulsar observations where sometimes the observational data cannot be obtained for some years due to several reasons. For example, the data of the Hulse-Taylor binary for a decade in the 1990s was not obtained because of major upgrades of the Arecibo telescope (Hulse, 1994). If the unseen region is completely overlapped with the Period B of the ZLK oscillation, one never recognizes ZLK oscillation only from the data of the orbital elements because the high eccentricity state shown in Fig. 2.9 is completely missed. With the plot of the CSPT like Fig. 2.10, however, it can be concluded that the bending in Period B must exist from the observational data about the periastron time T_N in both Periods A and C. Then it is possible to judge whether the ZLK oscillation had happened or not by using the CSPT without the data in the highly eccentric state.

One may be worried about the spin-orbit coupling effect in 1.5PN terms (Barker and O'Connell, 1975) because the effect may change the direction of the pulsar rotation axis and the beaming direction of the pulse signal. The change of the beaming direction may cause the disappearance of the pulse signal from the radio observation. The effect of the spin-orbit coupling in the ZLK mechanism is roughly estimated by using the so-called "adiabaticity parameter" $\mathcal{A}$ (Liu and Lai, 2017, 2018). This parameter is the ratio of the ZLK timescale to the 1.5PN precession timescale and I found it is small enough for the model used in this subsection. It means that the spin of the pulsar evolves "non-adiabatically" even when the ZLK oscillation occurs, that is, the spin is parallelly transported just as Newtonian case, and then the beaming direction does not change so much. I revisit this problem for the other models and discuss more detail in §2.4.

Finally, I discuss the possible parameter range of the third body with which the bending of the CSPT curve occurs within our lifetime (about 100 yrs). In addition to the model given in Table 2.1, 19200 models are made by changing the outer semi-major axis ($10\,\mathrm{au} \leq a_{\mathrm{out}} \leq 40\,\mathrm{au}$) and the mass of the third body ($10\,\mathrm{M_\odot} \leq m_3 \leq 90\,\mathrm{M_\odot}$), and their orbital evolutions are calculated. In the evolutions of these models, the time taken to see the deviation of Δ_P from Δ_{P1}, T_{d}, is detected by using a simple criterion

$$\frac{(\Delta_P - \Delta_{P1})}{\Delta_{P1}} > 1. \tag{2.65}$$

Fig. 2.11 shows the color contour map of T_{d}. In the black region seen in the bottom-right corner of Fig. 2.11, T_{d} is longer than 100 yrs. The white dotted line shows the critical curve obtained by the theoretical estimation of the ZLK timescale. Here I used the rough estimation of the Newtonian ZLK timescale given as $T_{\mathrm{ZLK}} \sim n_{\mathrm{in}} a_{\mathrm{in}}^2 / V_0 = 100$ yrs. It is found that the dependence of T_{d} on a_{out} and m_3 are almost consistent with the critical curve estimated by the Newtonian ZLK timescale. This is because the semi-major axes of the present model are large enough that the 1PN effect is negligible. If the parameters of the third body are in the top-left white region with $a_{\mathrm{out}} < 15\,\mathrm{au}$ and $m_3 > 30\,\mathrm{M_\odot}$, the system becomes unstable. The yellow solid line is obtained from the empirical criterion for the stability of the Newtonian three-body systems given by Mardling and Aarseth (2001) as

$$\frac{a_{\mathrm{out}}}{a_{\mathrm{in}}} > \frac{2.8}{1 - e_{\mathrm{out}}} \left[\left(1 + \frac{m_3}{m_1 + m_2} \right) \frac{1 + e_{\mathrm{out}}}{(1 - e_{\mathrm{out}})^{\frac{1}{2}}} \right]^{\frac{2}{5}}. \tag{2.66}$$

From Fig. 2.11, one can find that if the parameters of the third companion are within $m_3 = 10\text{-}100\,\mathrm{M_\odot}$ and $a_{\mathrm{out}} \lesssim 40\,\mathrm{au}$, the bending of the CSPT curve may be detected within 100 yrs through the observation of radio pulse.

2.3.3   Possible Models with a Pulsar

In this section, I consider several models with a broad range of parameters. First, I classify the hierarchical triple systems with the mass ratio of their components. Then I discuss the constraints on parameters obtained from the stability condition and the observable timescale as done in the last subsection and give several models in the allowed parameter range.
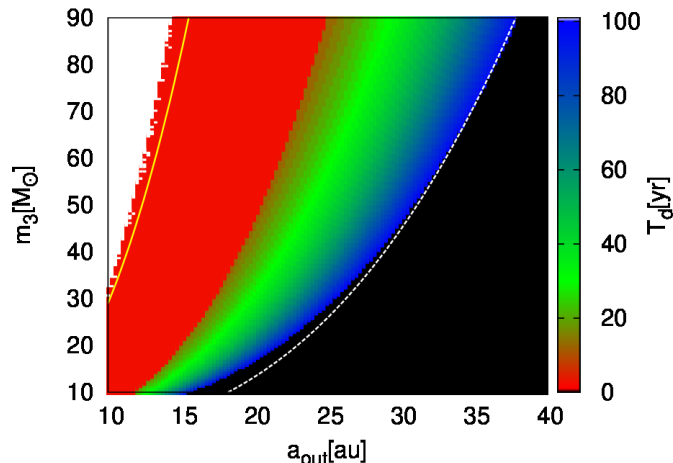
Figure 2.11: The color contour map of T_d that shows the parameter range of the third body with which the bending of the CSPT curve occurs within 100 yrs. The horizontal and vertical axes are the outer semi-major axis a_out and the mass of the tertiary companion m_3, respectively. The color shows the value of T_d, which is the minimum time such that the criterion Eq. (2.65) is satisfied. In the black region, the bending of the CSPT curve does not occur for 100 yrs and the white dashed line corresponds to the theoretical boundary obtained from the rough estimation of the ZLK timescale. In the white region, the system becomes unstable; the yellow solid line is an empirical criterion given by Mardling and Aarseth (2001).

The hierarchical triple systems are classified into three classes according to their mass ratio:

$$\text{Class } [1] \quad m_\mathrm{in} \ll m_3\,,$$
$$\text{Class } [2] \quad m_\mathrm{in} \sim m_3\,,$$
$$\text{Class } [3] \quad m_\mathrm{in} \gg m_3\,.$$

In Class [1], the ZLK oscillation explained in §2.2 can be obtained (VanLandingham et al., 2016; Randall and Xianyu, 2018; Hoang et al., 2019). For Class [2], the ZLK oscillations may also occur (Blaes et al., 2002; Wen, 2003; Thompson, 2011; Liu and Lai, 2018) as in Class [1] as long as the outer semi-major axis a_out is much longer than a_in. The systems in Class [2] with a_out not large enough compared to a_in do not have a sufficient hierarchy and the gravitational interaction between the inner and outer orbits is strong. As a result, both the inner and outer orbital elements will extremely change and the orbit may become chaotic. Such systems are unstable.

In Class [3], when the outer semi-major axis is much longer than that of the inner one ($a_\mathrm{out} \gg a_\mathrm{in}$), the outer object can be treated as a test particle and the inner orbit is not affected so much by the tertiary object, while the orbital elements of the outer orbit may change with time. However, it is known that the outer eccentricity does not change with time at least in the quadrupole order approximation. Instead of the outer eccentricity, the longitude of ascending node of the outer orbit Ω_out and the relative inclination I oscillate in a secular timescale (Naoz et al., 2017). In this

research, I focus on the CSPT caused by the excitation of the eccentricity of the binary pulsar and I discuss only Classes [1] and [2].

In order to observe the CSPT through radio signals, all models should have a pulsar as a component of the inner binary. I choose the companion of the pulsar from compact objects with a similar or larger mass than that of the pulsar, that is, a neutron star (NS) or a black hole (BH), to obtain the large GW emissions. For these compact objects, one can neglect the tidal dissipation effect, which may be strong for a non-compact object like a main-sequence star. The energy dissipation by the tidal force may also affect the periastron shift in addition to the GW emission and the CSPT will be more complicated. This interesting but complicated effect is beyond the scope of this chapter. Hence, below three types of model for inner binaries are discussed here:

$$\text{P-NS binary} \quad (\text{pulsar} + \text{NS}),$$
$$\text{P-BH binary} \quad (\text{pulsar} + \text{BH}),$$
$$\text{P-IMBH binary} \quad (\text{pulsar} + \text{intermediate-mass BH}).$$

The values of the masses and the semi-major axis of these inner binaries are shown in Table 2.2.

As discussed in §2.3.2, there exist some constraints on the parameter of the outer body to have the ZLK oscillation on an appropriate timescale. In Figs. 2.12 to 2.14, the constraints are shown in terms of the outer semi-major axis a_{out} and the mass of the third body m_3 by fixing parameters of the inner binary. The dashed black line shows the boundary for the outer binary mass $m_3 \geq m_1 + m_2$ for the hierarchical triple systems Class [1] and Class [2], which means that the gray area in the figures is not treated in this research.

The blue thin-stripe region is the parameter range where the empirical stability condition obtained in Mardling and Aarseth (2001) given in Eq. (2.66) is satisfied. The boundary of this condition is sometimes called the "chaotic boundary". This condition should be satisfied so that the hierarchical structure of the system does not break at least in the initial state.

The magenta-colored region is obtained from Eq. (2.33), which ensures that the ZLK oscillation occurs even with 1PN effects. Note that this magenta area is depicted by setting $e_{\text{in}} = e_{\text{out}} = 0$ in Eq. (2.33) because it does not change the area so much even for non-zero eccentricities in these figures.

In order to observe the effect of the ZLK oscillation on the CSPT, the ZLK timescale should be shorter than our lifetime. The ZLK timescale can be roughly estimated as $T_{\text{ZLK}} \sim n_{\text{in}} a_{\text{in}}^2 / V_0$ and its contours are shown in Figs. 2.12 to 2.14 by the dark-green lines for $T_{\text{ZLK}} = 10, 10^2$, and 10^3 yrs.

When the third body has the parameters in the area where the blue thin-stripe and the magenta-colored regions are overlapped in Figs. 2.12 to 2.14, the ZLK oscillation will occur on an appropriate timescale. The parameters of the models in this research are plotted by the black dots with the model names in these figures. In this research, nine models are analyzed: for the P-NS inner binary, PNN, PNB, PNIB, and PNSB models, in which the tertiary companion is an NS, BH, IMBH, and supermassive black hole (SMBH), respectively, are discussed. For the P-BH inner binary, I consider three cases: PBB, PBIB, and PBSB, in which the tertiary
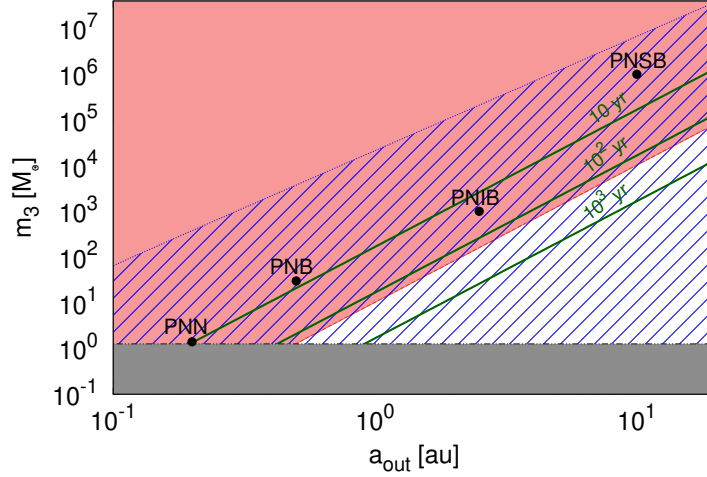
Figure 2.12: The constraints on the parameters of the outer orbit with a pulsar-NS (P-NS) inner binary to have the stable ZLK oscillation on an appropriate timescale. The parameters of the inner binary are fixed as $m_1 = 1.4\,\mathrm{M_\odot}$, $m_2 = 1.4\,\mathrm{M_\odot}$ and $a_{\mathrm{in}} = 0.01\,\mathrm{au}$. The dashed black line denotes the boundary of $m_3 \geq m_1 + m_2$, which is the condition of Class [1] and Class [2] of hierarchical triple systems. In the blue thin-stripe region, a hierarchical triple system is stable from the empirical condition. The condition for the ZLK oscillations not to be suppressed by the 1PN effect is given by the magenta-colored region. The overlapped region gives a stable ZLK oscillation even in the 1PN calculation. The dark-green lines show the ZLK timescales ($T_{\mathrm{ZLK}} = 10, 10^2$, and 10^3 yrs), which should be shorter than our lifetime (< 100 yrs) for observation. Our models given in Table 2.2 are shown by the black dots.
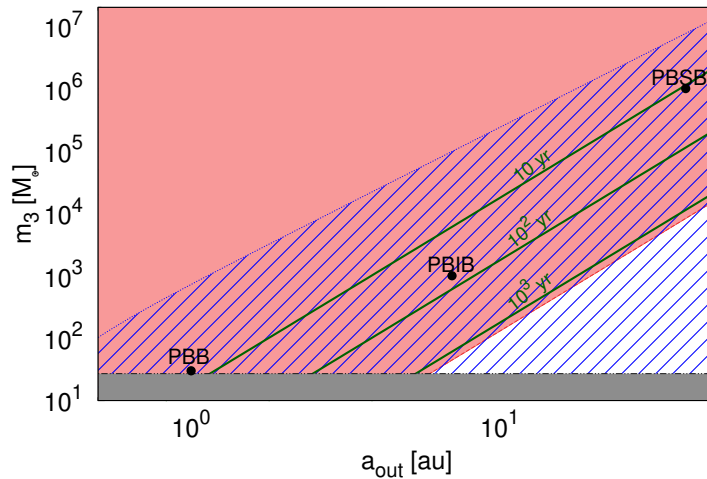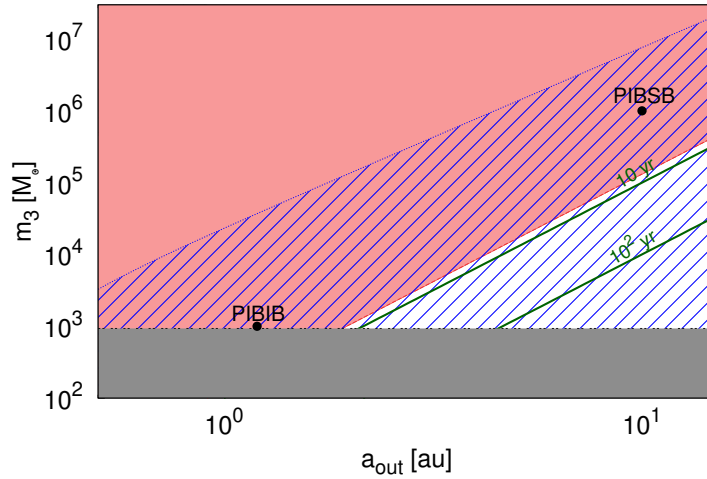

Figure 2.13: The same figure as Fig. 2.12, but the inner binary is a pulsar-BH (P-BH) binary. The parameters of the inner binary are fixed as $m_1 = 30\,\mathrm{M_\odot}$, $m_2 = 1.4\,\mathrm{M_\odot}$ and $a_{\mathrm{in}} = 0.01\,\mathrm{au}$.

Figure 2.14: The same figure as Fig. 2.12, but the inner binary is a pulsar-IMBH (P-IMBH) binary. The parameters of the inner binary are fixed as $m_1 = 10^3\,\mathrm{M_\odot}$, $m_2 = 1.4\,\mathrm{M_\odot}$ and $a_\mathrm{in} = 0.1\,\mathrm{au}$.

companion is a BH, IMBH, and SMBH, respectively. I also analyze the model PIBIB and PIBSB: these systems have the P-IMBH inner binary and an IMBH or SMBH as a tertiary companion. The masses of a pulsar (or NS), BH, IMBH, and SMBH are chosen as $1.4\mathrm{M_\odot}$, $30\mathrm{M_\odot}$, $10^3\mathrm{M_\odot}$, and $10^6\mathrm{M_\odot}$, respectively. The masses, semi-major axes, and the 1PN parameter $\epsilon^{(1\mathrm{PN})}$ defined in Eq. (2.28) for all the models are summarized in Table 2.2.

Here I briefly discuss the 1.5PN effect called the Lense-Thirring precession effect. This is one of the spin-orbit coupling effects appearing in the 1.5PN order corrections (Barker and O'Connell, 1975). Recent studies pointed out that the Lense-Thirring precession caused by the rapid rotation of an outer SMBH changes the evolutions of the ZLK oscillation (Fang and Huang, 2019; Fang et al., 2019; Liu et al., 2019). The timescale of this effect is evaluated in Liu et al. (2019) as

$$T_\mathrm{LT} = \frac{2c^3 a_\mathrm{out}^3 (1 - e_\mathrm{out}^2)^{3/2}}{\chi_3 G^2 m_3^2 (4 + 3m_\mathrm{in}/m_3)},\tag{2.67}$$

where $\chi_3 \leq 1$ is the Kerr parameter of the third object. If T_LT is much larger than the ZLK timescale T_ZLK, the Lense-Thrring precession effect can be neglected on a few ZLK timescales. This situation is obtained if the following condition is satisfied:

$$\left(\frac{a_\mathrm{in}}{\mathrm{au}}\right)^{\frac{3}{2}} \gg 10^{-12} \left(\frac{m_3}{\mathrm{M_\odot}}\right) \left(\frac{m_\mathrm{in}}{\mathrm{M_\odot}}\right)^{\frac{1}{2}},\tag{2.68}$$

where $\chi_3 = 1$ is imposed. Since all models in Table 2.2 satisfy this condition, the 1.5PN effect on the orbital evolution is safely neglected in this research.

In order to set initial conditions for numerical simulations, the other orbital parameters like the eccentricity e and the inclination i are needed. These parameters give the conserved quantities θ and $C_\mathrm{ZLK}^{(1\mathrm{PN})}$, which classify the types of the ZLK

oscillation as "libration" or "rotation" (see §2.2). In this research, four sets of the initial parameters are prepared for each model: "initially circular libration (ICL)", "initially circular rotation (ICR)", "initially eccentric libration (IEL) " and "initially eccentric rotation (IER)". For "Initially circular" and "initially eccentric" types, the initial inner eccentricities are set as $e_{\rm in} = 0.01$ and $e_{\rm in} = 0.6$, respectively. The other parameters are determined to obtain $C_{\rm ZLK}^{\rm (1PN)} < 0$ for libration and $C_{\rm ZLK}^{\rm (1PN)} > 0$ for rotation. The parameters of these types for each model are summarized in Tables 2.3, 2.4, and 2.5 for P-N, P-BH, and P-IMBH inner binaries, respectively, and they are used as the initial conditions for 1PN calculations. In order to study the 1PN effects, the Newtonian calculations are also performed and the results are compared. The Newtonian conserved quantities for the ZLK oscillations are set to have the same value as the 1PN ones: θ^2 is the same as the 1PN one and $C_{\rm ZLK}$ is set equal to $C_{\rm ZLK}^{\rm (1PN)}$ by choosing the initial argument of periastron as $\omega_{\rm in}^{\rm (N)}$ given in the last column of Tables 2.3 to 2.5.

Model	inner binary	tertiary companion	$m_1[\mathrm{M_\odot}]$	$m_2[\mathrm{M_\odot}]$	$m_3[\mathrm{M_\odot}]$	class	$a_{\mathrm{in}}(0)[\mathrm{au}]$	$a_{\mathrm{out}}(0)[\mathrm{au}]$	$\epsilon^{(\mathrm{1PN})}$
PNN	P-NS	NS	1.4	1.4	1.4	[1]	0.01	0.2	0.177
PNB	P-NS	BH	1.4	1.4	30	[2]	0.01	0.5	0.129
PNIB	P-NS	IMBH	1.4	1.4	10^3	[2]	0.01	2.5	0.484
PNSB	P-NS	SMBH	1.4	1.4	10^6	[2]	0.01	10.0	0.0310
PBB	P-BH	BH	30	1.4	30	[1]	0.1	1.0	0.0130
PBIB	P-BH	IMBH	30	1.4	10^3	[2]	0.1	7.0	0.134
PBSB	P-BH	SMBH	30	1.4	10^6	[2]	0.1	40.0	0.249
PIBIB	P-IMBH	IMBH	10^3	1.4	10^3	[1]	0.1	1.2	0.684
PIBSB	P-IMBH	SMBH	10^3	1.4	10^6	[2]	0.1	10.0	0.396

Table 2.2: The masses and the initial semi-major axes of the models are summarized. The second object is fixed as a pulsar with mass $m_2 = 1.4\,\mathrm{M_\odot}$. In the last column, the parameter of the 1PN effect $\epsilon^{(\mathrm{1PN})}$ defined in Eq. (2.28) is shown. P, NS, BH, IMBH, and SMBH are abbreviations of a pulsar, neutron star, black hole, intermediate-mass black hole, and a supermassive black hole, respectively.

model	$\epsilon^{(1PN)}$	Type	e_{in}	$i_{in}[deg]$	$\omega_{in}[deg]$	$C_{ZLK}^{(1PN)}$	θ^2	$\omega_{in}^{(N)}[deg]$
PNN	0.177	ICL	0.01	60	60	-3.18×10^{-5}	0.250	57.0
		ICR	0.01	60	30	6.20×10^{-5}	0.250	26.8
		IEL	0.6	53	90	-0.170	0.232	73.9
		IER	0.6	45	60	0.0667	0.320	53.8
PNB	0.129	ICL	0.01	60	60	-4.42×10^{-5}	0.250	57.8
		ICR	0.01	60	30	5.96×10^{-5}	0.250	27.7
		IEL	0.6	53	90	-0.182	0.232	76.3
		IER	0.6	45	60	0.0548	0.320	55.4
PNIB	0.484	ICL	0.01	60	60	-1.64×10^{-5}	0.250	52.0
		ICR	0.01	60	30	7.73×10^{-5}	0.250	20.4
		IEL	0.6	53	90	-0.0931	0.232	62.7
		IER	0.6	45	60	0.143	0.320	43.9
PNSB	0.0310	ICL	0.01	60	60	-3.91×10^{-5}	0.250	59.5
		ICR	0.01	60	30	5.47×10^{-5}	0.250	29.5
		IEL	0.6	53	90	-0.206	0.232	83.3
		IER	0.6	45	60	0.0302	0.320	58.9

Table 2.3: The important parameters in initial conditions for the 1PN ZLK oscillation for models with the P-NS inner binary. The four sets of initial parameters are prepared: "initially circular libration (ICL)", "initially circular rotation (ICR)", "initially eccentric libration (IEL)" and "initially eccentric rotation (IER)". In the fourth to sixth columns, e_{in}, i_{in}, ω_{in} show the eccentricity, the inclination, and the argument of the periastron of the inner orbit, respectively. The two conserved quantities for the 1PN ZLK oscillation $C_{ZLK}^{(1PN)}$ and θ^2 are also given in the seventh and eighth columns. For "initially circular" and "initially eccentric" types, I set $e_{in} = 0.01$ and $e_{in} = 0.6$, respectively. The other parameters are determined to obtain $C_{ZLK}^{(1PN)} < 0$ for libration and $C_{ZLK}^{(1PN)} > 0$ for rotation types, respectively. For the outer orbit, $e_{out} = 0$ and $i_{out} = 0°$ are used and ω_{out} cannot be defined. About the parameters other than those shown in the table, the longitude of the ascending node Ω is set as 0 for both inner and outer orbits, and the mean anomaly M is set as $0°$ and $20°$ for inner and outer orbits. The Newtonian calculation is also performed to compare both the Newtonian and 1PN results. The Newtonian two conserved quantities for the ZLK oscillation are set as the same value as the 1PN ones, that is, θ^2 is the same as the 1PN one and C_{ZLK} is set equal to $C_{ZLK}^{(1PN)}$ by choosing the initial argument of periastron as $\omega_{in}^{(N)}$ given in the last column.

2.4 Results and Discussions

In this section, the results of the numerical simulations explained in §2.3.1 are shown. First I show the results of the orbital evolutions obtained for the models introduced in §2.3.3. I discuss the accuracy problem of the double-averaging method by comparing the results obtained from the 1PN direct integration and those from the double-averaging method with the 1PN correction. I also compare the 1PN and Newtonian direct-integration results to recognize how the 1PN effect appears in the ZLK mechanism calculated by the direct integration.

model	$\epsilon^{(1PN)}$	Type	e_{in}	$i_{in}[\deg]$	$\omega_{in}[\deg]$	$C_{ZLK}^{(1PN)}$	θ^2	$\omega_{in}^{(N)}[\deg]$
PBB	0.0130	ICL	0.01	60	60	-4.00×10^{-5}	0.250	59.8
		ICR	0.01	60	30	5.38×10^{-5}	0.250	29.8
		IEL	0.6	53	90	-0.211	0.232	85.7
		IER	0.6	45	60	0.0257	0.320	59.5
PBIB	0.177	ICL	0.01	60	60	-3.39×10^{-5}	0.250	57.7
		ICR	0.01	60	30	5.98×10^{-5}	0.250	27.6
		IEL	0.6	53	90	-0.181	0.232	76.0
		IER	0.6	45	60	0.0559	0.320	55.3
PBSB	0.0249	ICL	0.01	60	60	-3.94×10^{-5}	0.250	59.6
		ICR	0.01	60	30	5.44×10^{-5}	0.250	29.6
		IEL	0.6	53	90	-0.208	0.232	84.0
		IER	0.6	45	60	0.0287	0.320	59.1

Table 2.4:   The same table as Table 2.3 but for models with the P-BH inner binary.

model	$\epsilon^{(1PN)}$	Type	e_{in}	$i_{in}[\deg]$	$\omega_{in}[\deg]$	$C_{ZLK}^{(1PN)}$	θ^2	$\omega_{in}^{(N)}[\deg]$
PIBIB	0.684	ICL	0.01	60	60	-6.41×10^{-5}	0.250	48.8
		ICR	0.01	60	30	8.73×10^{-5}	0.250	15.1
		IEL	0.6	53	90	-0.0430	0.232	56.9
		IER	0.6	45	60	0.194	0.320	37.5
PIBSB	0.396	ICL	0.01	60	60	-2.08×10^{-5}	0.250	53.4
		ICR	0.01	60	30	7.29×10^{-5}	0.250	22.3
		IEL	0.6	53	90	-0.115	0.232	65.5
		IER	0.6	45	60	0.122	0.320	46.7

Table 2.5:   The same table as Table 2.3 but for models with the P-IMBH inner binary.

Then I show the results of the CSPT. I discuss how the shape of the CSPT curve depends on the types of the ZLK oscillation by comparing the results of four types of models (ICL, ICR, IEL, IER). I also focus on the initial time when the CSPT calculation is started. I found that the shape of the CSPT curves becomes different when the starting time is different even for the same model.

2.4.1   Orbital Evolutions

The stable orbital evolutions are observed in all the models shown in Tables 2.3 to 2.5. Some results obtained in different models look similar, so I show the results of the PNN (+ PBB) model and the PNIB model as representative avoiding just show many similar figures. The PNN model is chosen because the mass hierarchy in this model is the smallest in all the models and it is expected that the deviation from the test-particle approximation used in the double-averaging method shown §2.2 is the largest. With the results of this model, the differences between these two methods are discussed, and for some related analyses, the results of the PBB model are also shown. The PNIB model has $\epsilon^{(1PN)}$ which is the largest in Table 2.3 and the relativistic effect in this model may be important. I discuss the 1PN effects on the ZLK mechanism by comparing Newtonian and 1PN direct integration results
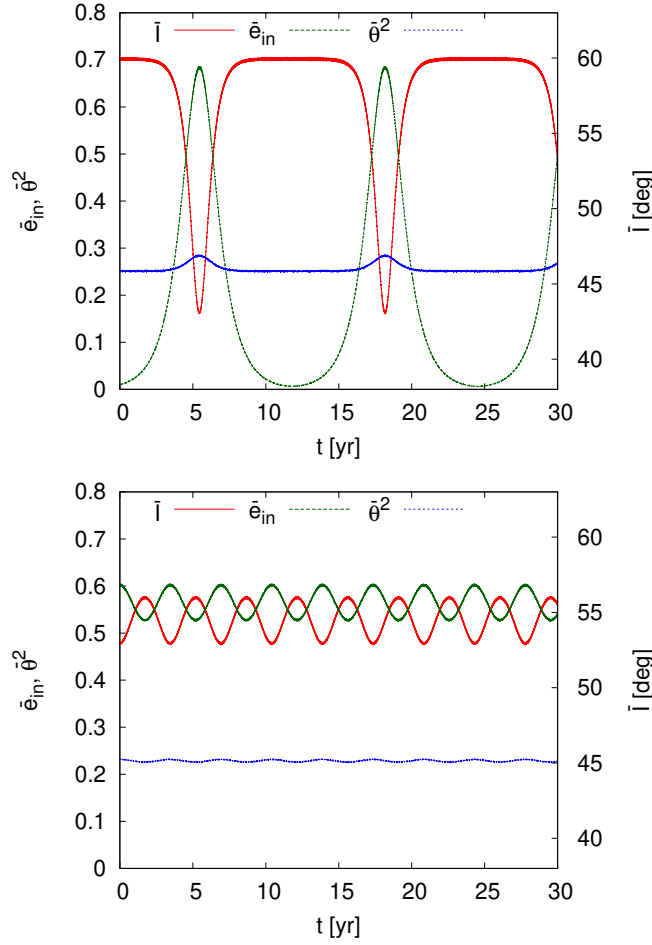
Figure 2.15: Time evolution of the averaged inner eccentricity $\bar{e}_{\rm in}$ (green line), relative inclination $\bar{I}$ (red line) and the conserved value for the ZLK oscillation $\bar{\theta}^2$ (blue line) for the "libration" type of the ZLK oscillations in the PNN model. The top and bottom panels show the results of the ICL and IEL types, respectively.

for this model.

Direct Integration v.s. Double-averaging Method

Figs. 2.15 and 2.16 are the time evolutions of the averaged inner eccentricity $\bar{e}_{\rm in}$, relative inclination $\bar{I}$, and conserved value for ZLK oscillation $\bar{\theta}^2$ of each type of the PNN model: Figs. 2.15 and 2.16 exhibit the results of the libration and rotation types of ZLK oscillations, respectively. The top and bottom panels of these figures are the results of the initially circular and eccentric types, respectively, whose parameters are given in Table 2.3. As in Fig. 2.9, the green, red, and blue lines correspond to the evolutions of $\bar{e}_{\rm in}$, $\bar{I}$, and $\bar{\theta}^2$.

The ZLK oscillation is observed in all the panels in these figures with different amplitudes and timescales. The initially eccentric types (bottom panels) have smaller amplitudes and shorter timescale than those of initially circular types (top panels). This amplitude difference reflects the feature of the ZLK oscillation explained in Fig. 2.6. In the initially circular type, the value of $C_{\rm ZLK}^{\rm (1PN)}$ is almost zero
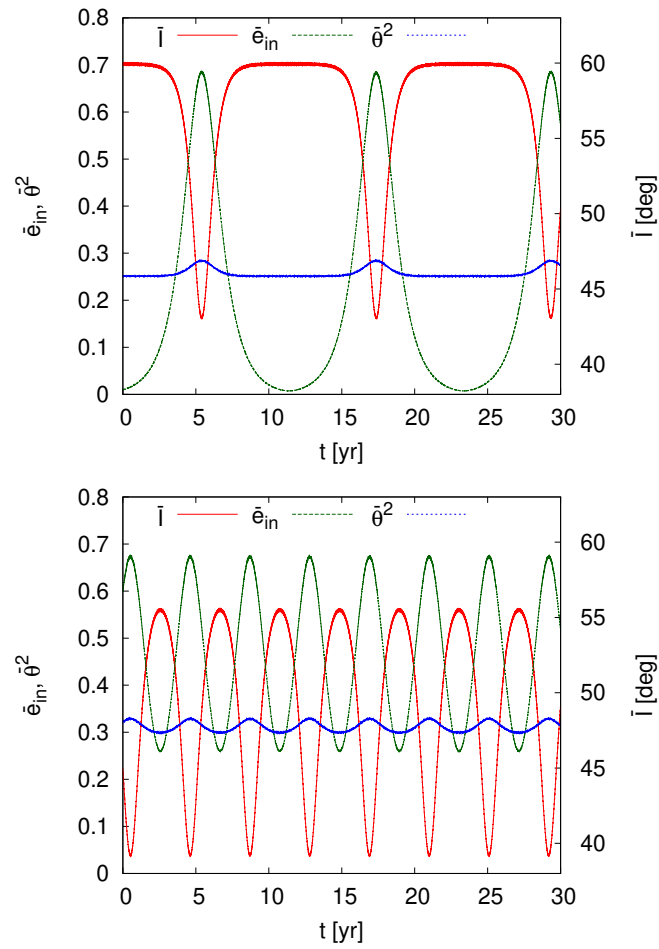
Figure 2.16:   The same figure as Fig. 2.15 for the "rotation" type of the ZLK oscillations in the PNN model. The top and bottom panels are the results of the ICR and IER types, respectively.

and the eccentricity oscillates between zero and the maximum value. In the initially eccentric type, on the other hand, $C_{\mathrm{ZLK}}^{(1\mathrm{PN})}$ has a finite value and the eccentricity oscillates between two finite values around the initial value, which means that the amplitude becomes smaller than that in the initially circular type. However, in all the panels, θ^2 is not exactly constant but oscillates on the ZLK timescale as seen in Fig. 2.9. It should be constant in the analysis by the double-averaging method with test-particle quadrupole approximation (see §2.2) and the oscillation of θ^2 may occur because the mass hierarchy is not enough and the test-particle limit is no longer satisfied in this model. The oscillating feature of θ^2 is consistent with what is seen in the results in Naoz et al. (2013a).

In order to clarify the difference between the results obtained from the direct integration and the double-averaging method, in Figs. 2.17 and 2.18, I show the evolution of $\bar{e}_{\mathrm{in}}$ obtained by the 1PN direct integration as a dark-green solid line as well as that calculated with the Lagrange planetary equations with 1PN correction (see §1.2.2) as a light-green dashed line. The latter one imposes the quadrupole approximation and the test-particle limit. It is integrated by the fourth-order implicit Runge-Kutta method using the W4 method (Okawa et al., 2018; Fujisawa et al., 2019), which is an improved version of the Newton-Raphson method, as an internal nonlinear solver. Each panel in Figs. 2.17 and 2.18 shows the same evolution of $\bar{e}_{\mathrm{in}}$ as shown in the corresponding panel in Figs. 2.15 and 2.16.

At first glance, one finds that the difference between the two lines is very small except for the IER type (the bottom panel in Fig. 2.18). The ZLK timescale obtained from the direct integration is smaller than that calculated in the double-averaging method in the panels of Fig. 2.17, but it is larger in the panels in Fig. 2.18. The deviation in timescale is much more obvious in the bottom panel of Fig. 2.18. For the amplitude, the tendency of the difference is more complicated than that of the timescale. In the results of the ICL and ICR types (top panels in Fig. 2.17 and 2.18), the amplitude of the ZLK oscillation is larger in the direct simulation than that obtained with double-averaged calculation. Both the lines in each panel have the same minimum values but the maximum values are enhanced in dark-green lines. In the result of the IER type (bottom panel of Fig. 2.18), the enhancement of the amplitude in the direct simulation is observed as seen in the ICL and ICR types, but both the maximum and minimum values in the dark-green line are smaller than those of the light-green line. In the result of the IEL type, (bottom panel of Fig. 2.17), on the other hand, the amplitudes of both two lines are almost the same. These differences are summarized in Table 2.6.

From the above features, the double-averaging method with the quadrupole approximation works well for the ICL, IEL, and ICR types of the ZLK oscillations in this model, but it should not be applied to the IER type because the deviation from the direct integration cannot be neglected in this type. One may wonder that the double averaging method can be improved if the higher-multipole interaction terms are taken into account. However, in the models with the PN-binary, the evolution equation obtained from octupole-order equations under the test-particle limit are completely the same as quadrupole ones because the octupole terms are always proportional to the mass difference $m_1 - m_2$ (see Eq. (2.26), which is obtained from Ford et al. (2000)). In order to consider the octupole-order effect for the
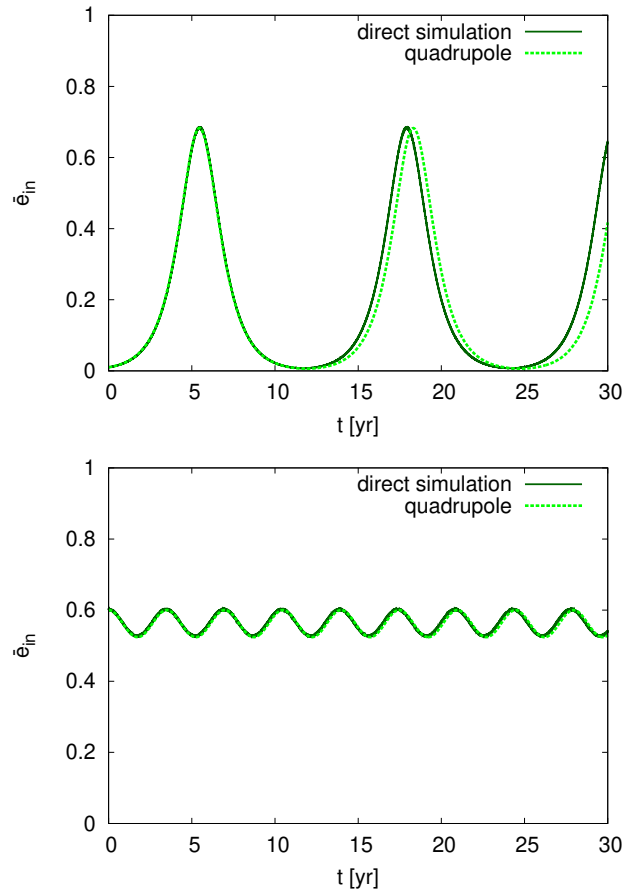
Figure 2.17:   Comparison between two evolution lines of the averaged inner eccentricity $\bar{e}_{\mathrm{in}}$ obtained by the direct integration (solid green line) and the double-averaging method (dashed light-green line) for the libration type of the ZLK oscillations in the PNN model. The top and bottom panels are the results of the ICL and IEL types, respectively.
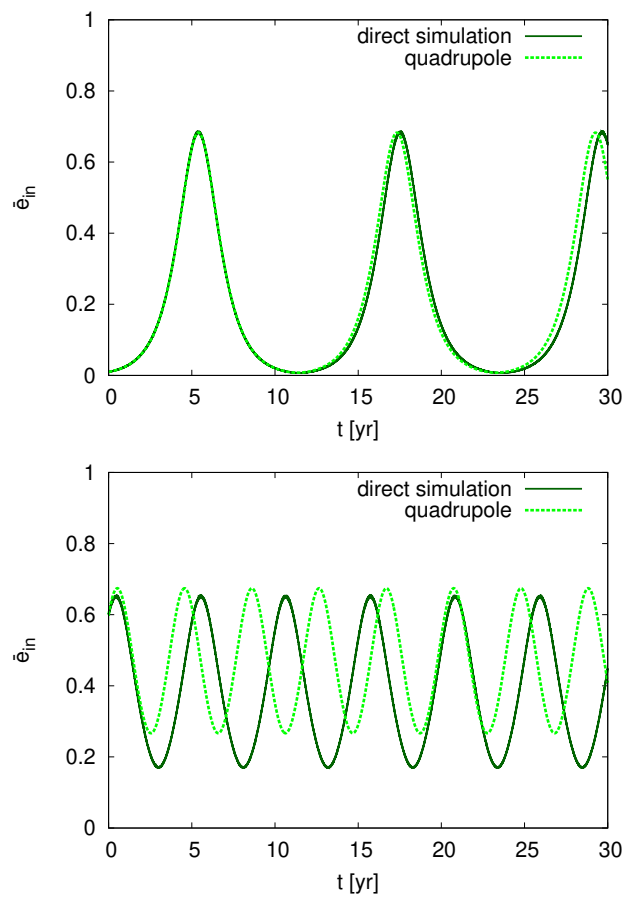
Figure 2.18: The same figure as Fig. 2.17 for the "rotation" type of the ZLK oscillations in the PNN model. The top and bottom panels show the results of the ICR and IER types, respectively.

Type	θ^2	$C_{\mathrm{ZLK}}^{(1\mathrm{PN})}$	method	$e_{\min}$	$e_{\max}$	$T_{\mathrm{ZLK}}[\mathrm{yrs}]$
ICL	0.25	-3.18×10^{-5}	direct	0.00728	0.687	12.465
			average	0.00613	0.683	12.858
ICR	0.25	6.20×10^{-5}	direct	0.00689	0.687	12.117
			average	0.00768	0.683	11.937
IEL	0.232	-0.170	direct	0.525	0.605	3.473
			average	0.524	0.600	3.477
IER	0.32	0.0667	direct	0.170	0.654	5.083
			average	0.267	0.675	4.046

Table 2.6:   The differences between the eccentricity evolutions calculated by the direct integration and by the double averaging method for the PNN model. The maximum and minimum eccentricities and the ZLK timescale T_{ZLK} are given. The first and second rows in each value show those obtained by the direct integration and by the double-averaging method, respectively.

system with $m_1 = m_2$, the potential with octupole order terms should be derived as the quadrupole order potential with massive objects derived in Naoz et al. (2013a), which is beyond the scope of this chapter.

Hence, to see the effect of the octupole-order terms, we instead analyze the PBB model with different-mass binary. The octupole-order double-averaging method is also calculated in the same way as that used for the quadrupole-order one. Figs. 2.19 and 2.20 show the evolution curves obtained by the direct integration (dark-green solid line), by the double-averaging method with quadrupole-order terms (light-green dashed line), and by that with the octupole-order terms (dark-blue dashed line). In the bottom panels of Figs. 2.19 and 2.20, the quadrupole- and octupole-order lines are almost the same but are different from the result of the direct-integration. In the top panels of Figs. 2.19 and 2.20, on the other hand, the difference between the results of quadrupole- and octupole-order expansion are seen. In the top panel of Fig. 2.19, the octupole-order expansion gives a better result compared with the quadrupole one. In the top figure of Fig. 2.20, if one looks at the second period, the result of the octupole-order expansion is better, but the opposite result is seen in the fourth period. This is possible because the result obtained by the direct integration sometimes shows an irregular period. I will revisit this point later in this subsection.

From these results for the PBB model, I cannot confirm that the octupole-order expansion improves the accuracy of the double-averaging method. What I can conclude here is that the double-averaged calculations not only in quadrupole-order but also octupole-order expansion do not exactly reproduce the evolution obtained by the direct integration. I remark that the deviation seen in the eccentricity evolution may be crucial when one evaluates the GW emission for the systems with finite masses because one may overestimate or underestimate the value of the eccentricity with the double-averaging method and the amplitude and frequency of GWs are strongly sensitive to the eccentricity, especially for the highly eccentric orbit like $e > 0.9$. Here I stress that it may be important to calculate the evolutions of such systems by direct integration.
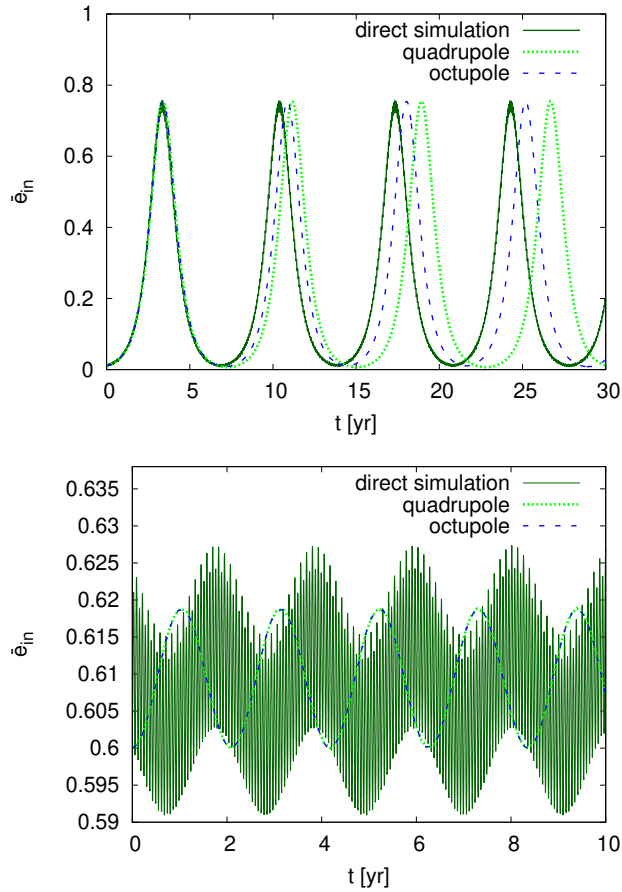
Figure 2.19: Three evolution lines of the averaged inner eccentricity $\bar{e}_{in}$ for the libration type of the ZLK oscillations in the PBB model obtained by three different methods: the direct integration (solid green line), the double-averaging method with the quadrupole approximation (dashed light-green line) and that with the octupole approximation (dashed dark-blue line). The top and bottom panels show the results of the ICL and IEL types, respectively.
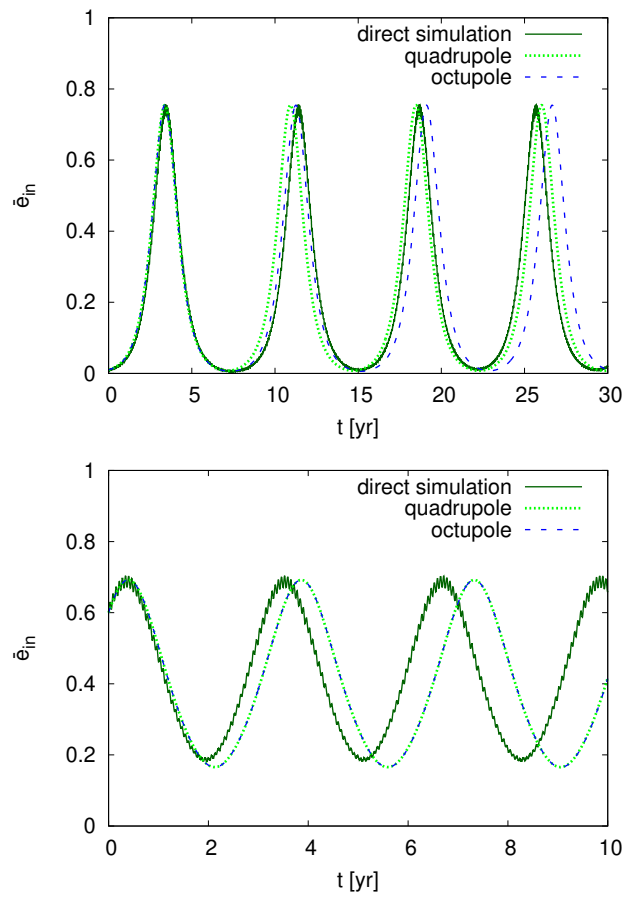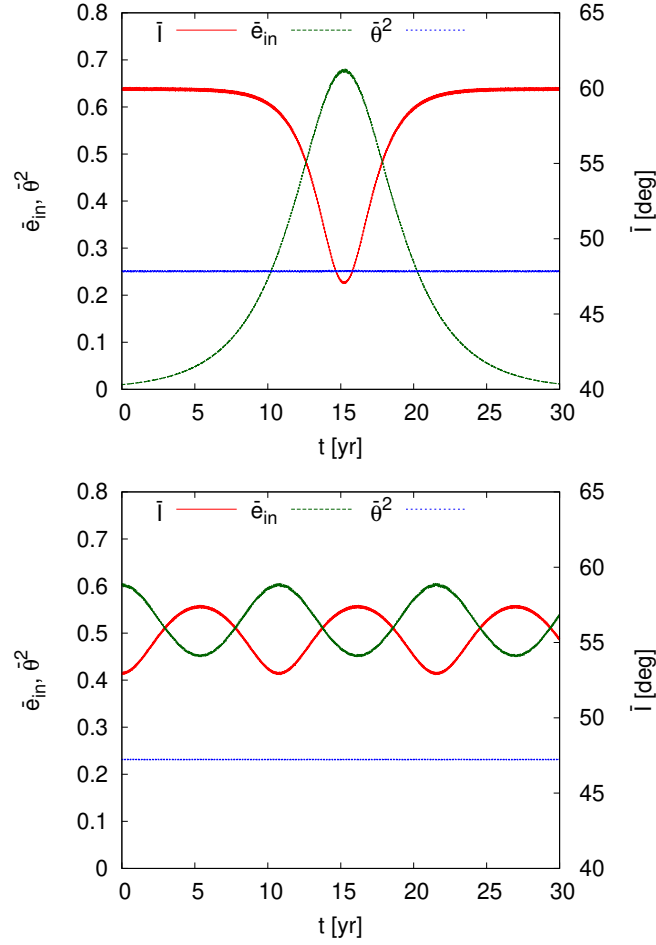
Figure 2.20: The same figure as Fig. 2.19 but for the "rotation" type of the ZLK oscillations in the PBB model. The top and bottom panels show the results of the ICR and IER types, respectively.

Figure 2.21: The same figure as Fig. 2.15 but for the PNIB model. The top and bottom panels correspond to the results of the ICL and IEL types, respectively.

Newtonian v.s. post-Newtonian

Figs. 2.21 and 2.22 are the same figures as Figs. 2.15 and 2.16 but for the PNIB model. The former and latter figures show the results of the libration and rotation types of the ZLK oscillations, respectively. As in the figures for the PNN model, top and bottom panels in each figure are the results of initially circular and eccentric types, respectively. As seen in Figs. 2.15 and 2.16, initially eccentric types (bottom panels) have smaller amplitudes and shorter timescale than those of initially circular types (top panels), which is similar to the results of the PNN model. The ZLK conserved value $\bar{\theta}^2$ is almost constant in the PNIB model unlike that in the PNN model, which means that the test-particle limit is valid in this model. In fact, the deviation from the double-averaging method is smaller than that of the PNN model.

The PNIB model has the largest value of $\epsilon^{(1PN)}$ in Table 2.3 and its relativistic effect may be strong enough to affect the ZLK oscillation. In Figs. 2.23 and 2.24, the evolutions of the eccentricity obtained by the 1PN and Newtonian direct simulations are shown as the dark-green and light-green solid lines, respectively. Each figure exhibits the results of the libration and rotation types of the ZLK oscillations. The top and bottom panels in each figure show the results of the initially circular and
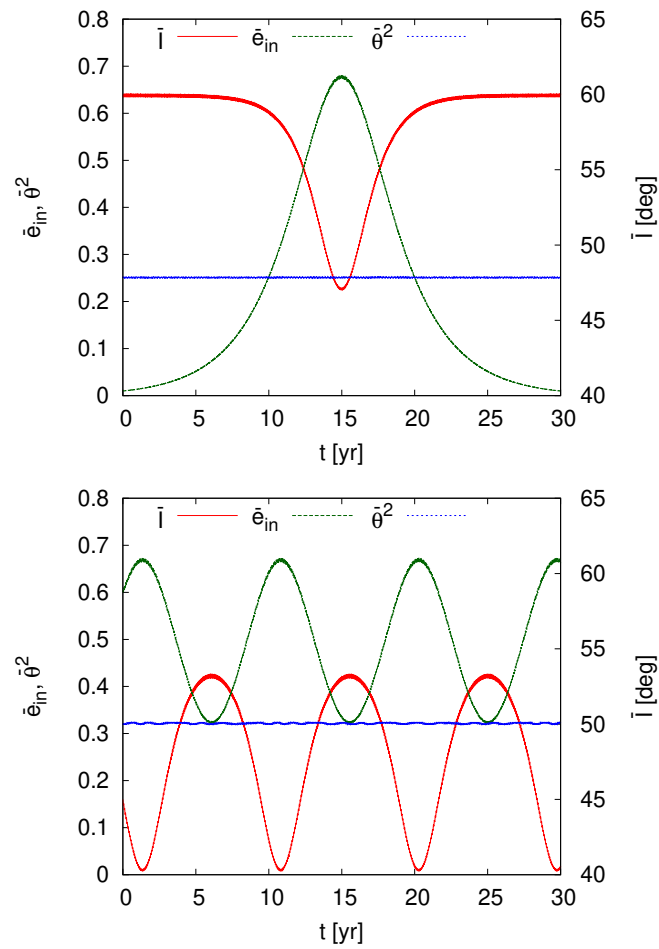
Figure 2.22:   The same figure as Fig. 2.16 but for the PNIB model. The top and bottom panels correspond to the results of the ICR and IER types, respectively.
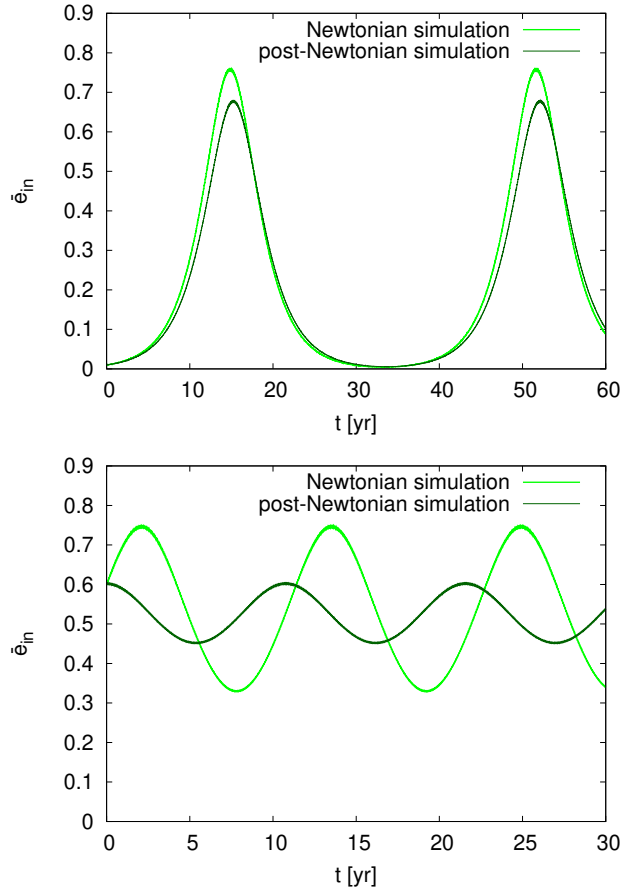
Figure 2.23: Comparison between Newtonian and post-Newtonian evolution curves of the averaged inner eccentricity $\bar{e}_{\mathrm{in}}$ for the "libration" type of the ZLK oscillations in the PNIB model. The top and bottom panels correspond to the results of the ICL and IEL types, respectively. The light- and dark-green curves describe the results obtained from Newtonian and 1PN direct simulations, respectively.

eccentric types.

The tendency of the difference between the two curves is complicated. In the results of the ICL and ICR types (top panels of Figs. 2.23 and 2.24), both the 1PN and Newtonian curves have the same minimum values (about zero), but the maximum value is suppressed in the 1PN curve, that is, the amplitude of the ZLK oscillation is smaller in the 1PN calculation. In these initially circular types, the ZLK timescale is a little longer in the 1PN result. In the results of the IEL and IER types (bottom panels of Figs. 2.23 and 2.24), on the other hand, the ZLK timescale obtained by the 1PN calculation is shorter than that obtained by the Newtonian one. About the amplitude, interestingly, the IEL (bottom panel of Fig. 2.23) and IER (bottom panel of Fig. 2.24) types have different features. In the IEL type, the amplitude obtained by the 1PN simulation is smaller than that of the Newtonian result and both the maximum and minimum values are suppressed unlike the results of the ICL and ICR types. On the other hand, in the result of the IER type, the amplitudes of the 1PN and Newtonian results are almost the same but both the maximum and minimum values of the 1PN result are shifted downward.
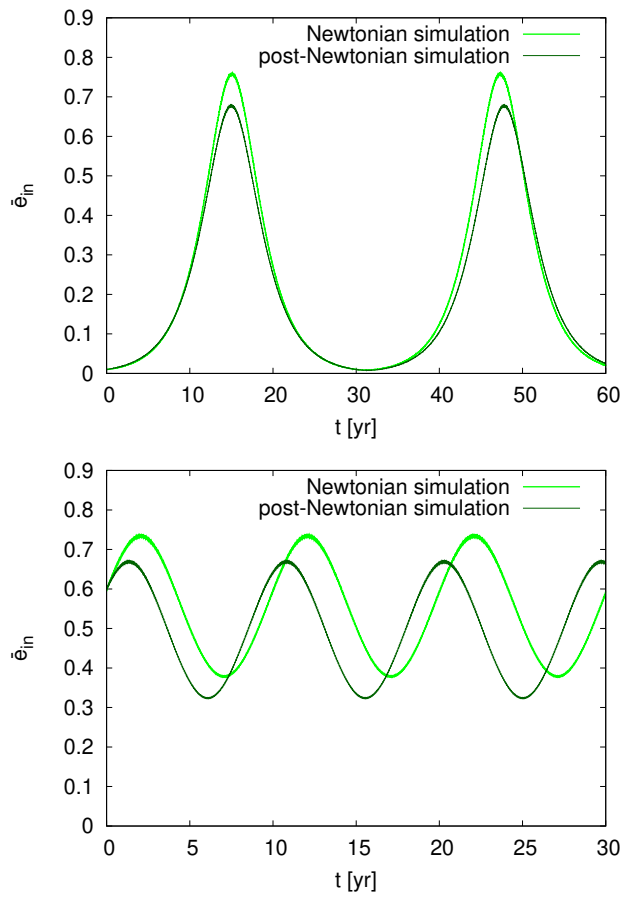
Figure 2.24:   The same figure as Fig. 2.23 for the "rotation" type of the oscillations in the PNIB model. The top and bottom panels correspond to the results of the ICR and IER types, respectively.

These complicated features can be understood basically by using the double-averaging method as discussed in §2.2.2. As in Fig. 2.7, the curves of the maximum and minimum eccentricities in terms of C_{ZLK} in Newtonian dynamics is shifted to the right when the 1PN term is taken into account by fixing $C_{\mathrm{ZLK}}^{(1\mathrm{PN})} = C_{\mathrm{ZLK}}$. In Fig. 2.7, one can find that the maximum value decreases and the minimum value increases for the libration type, while both maximum and minimum values decrease for the rotation type. These features are consistent with the properties seen in Figs. 2.23 and 2.24. I summarize the amplitude and timescale of the ZLK oscillation obtained by 1PN and Newtonian direct simulations in Table. 2.7. In the table, I also add the amplitude and timescale calculated by the 1PN double-averaging analysis in §2.2.2 as a reference.

Type	θ^2	$C_{\mathrm{ZLK}}^{(1\mathrm{PN})}$	method	$e_{\min}$	$e_{\max}$	$T_{\mathrm{ZLK}}[\mathrm{yrs}]$
ICL	0.25	-1.64×10^{-5}	N (direct)	0.00438	0.761	36.779
			1PN (direct)	0.00550	0.680	36.913
			1PN (average)	0.00509	0.668	37.673
ICR	0.25	7.73×10^{-5}	N (direct)	0.00869	0.761	32.231
			1PN (direct)	0.00776	0.680	32.60
			1PN (average)	0.00789	0.668	32.820
IEL	0.232	-0.0931	N (direct)	0.328	0.749	11.419
			1PN (direct)	0.450	0.605	10.804
			1PN (average)	0.428	0.599	11.144
IER	0.32	0.143	N (direct)	0.377	0.738	9.992
			1PN (direct)	0.322	0.672	9.504
			1PN (average)	0.336	0.669	9.111

Table 2.7: The differences between the eccentricity evolutions calculated by the Newtonian and 1PN direct integrations for the PNIB model. The amplitude and timescale calculated by the 1PN double-averaging analysis are also summarized as a reference. The first, second, and third rows give the results of the Newtonian direct integration, the 1PN direct integration, and the 1PN double-averaging method.

Irregularity of KL oscillation period

As we showed above, the amplitude of the ZLK oscillation and its timescale can be understood basically by the double-averaging method. However, sometimes there appears an irregularity of the period in the results calculated by the direct integration for some models. For example, the irregular periods are seen in the ZLK oscillations in the ICR type of the PNB and PBB models as shown in Fig. 2.25. This irregular behavior in the period of the ZLK oscillation was already found in Antonini and Perets (2012). They calculated orbital evolutions of BH binaries around SMBH by the direct integration and found the irregular periods and amplitudes in the ZLK oscillation (Fig. 3 in Antonini and Perets (2012)), which is consistent with but rather more drastic than the results obtained in this chapter.

Note that the amplitude and timescale of the ZLK oscillation are strongly dependent on two conserved quantities θ^2 and $C_{\mathrm{ZLK}}^{(1\mathrm{PN})}$, but not so much on the 1PN
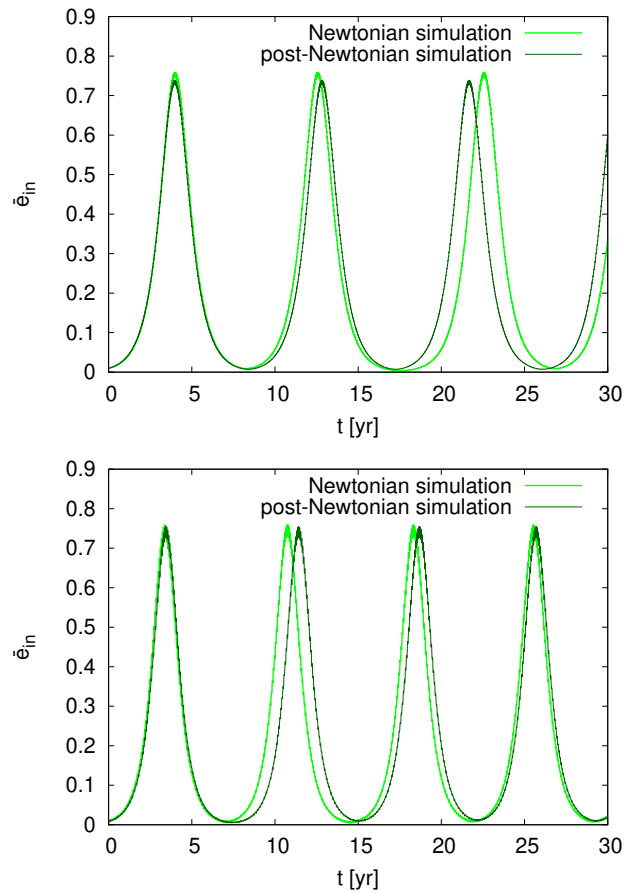
Figure 2.25:   The same figures as Fig. 2.23 for the ICR type of the ZLK oscillations in the PNB model (top) and the PBB model (bottom). The periods between two peaks are not regular on the Newtonian curve in the top panel and on the 1PN curve in the bottom panel.
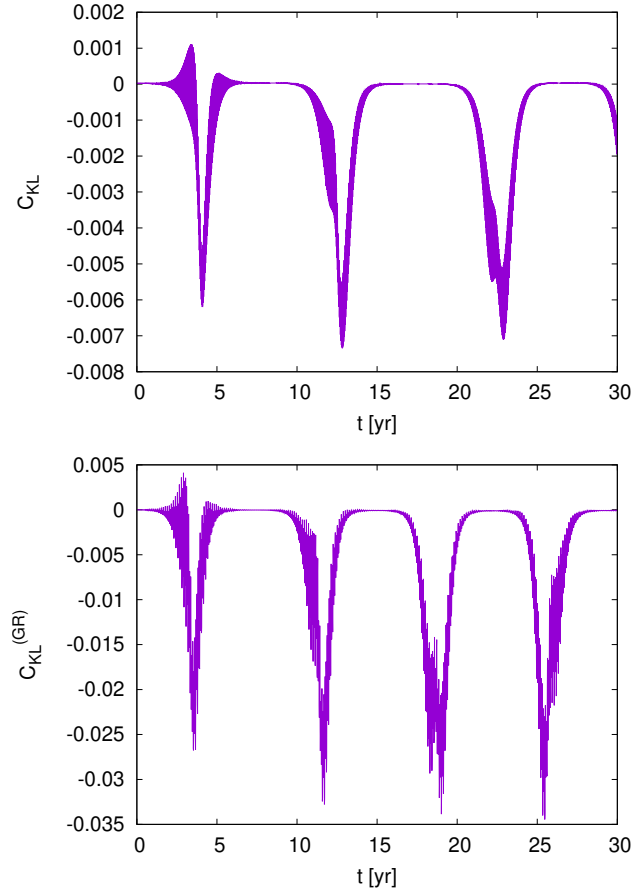
Figure 2.26: Time evolutions of C_{ZLK} and $C_{\text{ZLK}}^{(\text{GR})}$ for the ICR type KL-oscillations in the PNB model (top) and the PBB model (bottom), respectively.

parameter $\epsilon^{(\text{1PN})}$ except for the ICL type, in which the 1PN effect is important because it changes the existence range of the ZLK oscillation (see Eq. (2.33)). Hence, I analyze the behavior of the "conserved" quantities in the direct integration. As seen in Figs. 2.15 and 2.16, the value of θ^2 is not conserved but oscillates and drastically changes when the eccentricity reaches the maximum value. As for the other "conserved" quantity, the time evolution of C_{ZLK} and $C_{\text{ZLK}}^{(\text{1PN})}$ for the models shown in each panel in Fig. 2.25 are exhibited in the top and bottom panels of Fig. 2.26, respectively. These values are no longer conserved especially when the eccentricity reaches the maximum value. However, I remark that it becomes almost constant again when the eccentricity decreases. This time evolution of the "conserved" quantities may cause the irregular oscillations in the direct integration.

In order to analyze the detail, in Table 2.8, I show the numerical values of the oscillation periods obtained from the results in Fig. 2.25. The period n ($n = 1, 2, 3$) denotes the period from the n-th peak of the eccentricity to the $(n + 1)$-th peak. I also show the constant "conserved" values after the eccentricity passes through the maximum value. In addition, I also show the ZLK timescale evaluated by the double-averaging method with those values of C_{ZLK} or $C_{\text{ZLK}}^{(\text{1PN})}$, which are given as "period n (ave)" in the third row of each period in Table 2.8. One finds that those ZLK timescales evaluated by using the "conserved" quantity and the double-

	PNB		PBB	
	Newtonian	1PN	Newtonian	1PN
period 1	8.6 yrs	8.8 yrs	7.4 yrs	8.0 yrs
C_{ZLK} or $C_{\text{ZLK}}^{(1\text{PN})}$	3.2×10^{-5}	5.5×10^{-5}	2.6×10^{-5}	-2.7×10^{-5}
period 1 (ave)	9.34 yrs	8.90 yrs	8.06 yrs	8.03 yrs
period 2	10.0 yrs	8.8 yrs	7.6 yrs	7.2 yrs
C_{ZLK} or $C_{\text{ZLK}}^{(1\text{PN})}$	5.2×10^{-6}	5.6×10^{-5}	1.9×10^{-5}	-7.9×10^{-5}
period 2 (ave)	10.77 yrs	8.88 yrs	8.26 yrs	7.31 yrs
period 3	8.6 yrs	8.8 yrs	7.2 yrs	7.1 yrs
C_{ZLK} or $C_{\text{ZLK}}^{(1\text{PN})}$	3.2×10^{-5}	5.6×10^{-5}	3.1×10^{-5}	-1.1×10^{-4}
period 3 (ave)	9.34 yrs	8.88 yrs	7.94 yrs	7.09 yrs

Table 2.8: The period of the ZLK oscillations obtained from the results in Fig. 2.25. The period n ($n = 1, 2, 3$) denotes the period from the n-th to the $(n + 1)$-th peaks of the eccentricity obtained from the direct integration results. The value of C_{ZLK} or $C_{\text{ZLK}}^{(1\text{PN})}$ is the "conserved" value after the eccentricity passes through the maximum value. The periods calculated by the double-averaging method with the obtained C_{ZLK} or $C_{\text{ZLK}}^{(1\text{PN})}$ are given as the period n (ave), in the third rows of each period.

averaging estimation are consistent with the numerical ones obtained from the direct integration. I believe that these small deviations of the "conserved" values in each period cause a small irregularity of the ZLK oscillation period. Small differences from the numerical results still exist. I think this may be caused by a large deviation of C_{ZLK} or $C_{\text{ZLK}}^{(\text{GR})}$ near the maximum eccentricity.

As discussed in Antonini et al. (2017), this irregular behavior and the evolution of the "conserved" quantities may be caused by the effects of the higher-order multipole terms that are neglected in the double-averaging method. If the eccentricity excites in the orbital evolution, one may need to consider many higher-order multipole terms to obtain the exact evolution with the double-averaging method. Will (2017) calculated the expansion up to hexadecapole order and showed that even such higher-order effects could not be neglected in the orbital evolution with the excitation of the eccentricity. Hence, here I stress again that it should be important to calculate the ZLK mechanism with the direct integration.

2.4.2 Cumulative Shift of Periastron Time

The ZLK oscillation shown in §2.4.1 affects the evolution of the CSPT, Δ_P, of the binary pulsar in the hierarchical triple system. As I showed in §2.3.2, if a hierarchical triple system shows the ZLK oscillations in the observation period, the bending of the CSPT curve is expected. This is because when the eccentricity becomes large, the GW emission is enhanced and then the orbital period changes drastically. Here I discuss how the bending of the CSPT curve depends on the models or types of the ZLK oscillation.

The time evolution of the CSPT is calculated as explained in §2.4.2 for each model in Tables 2.3 to 2.5. Since the behavior of the CSPT curves of these models is similar, only the results for the PNIB model are shown here as representative
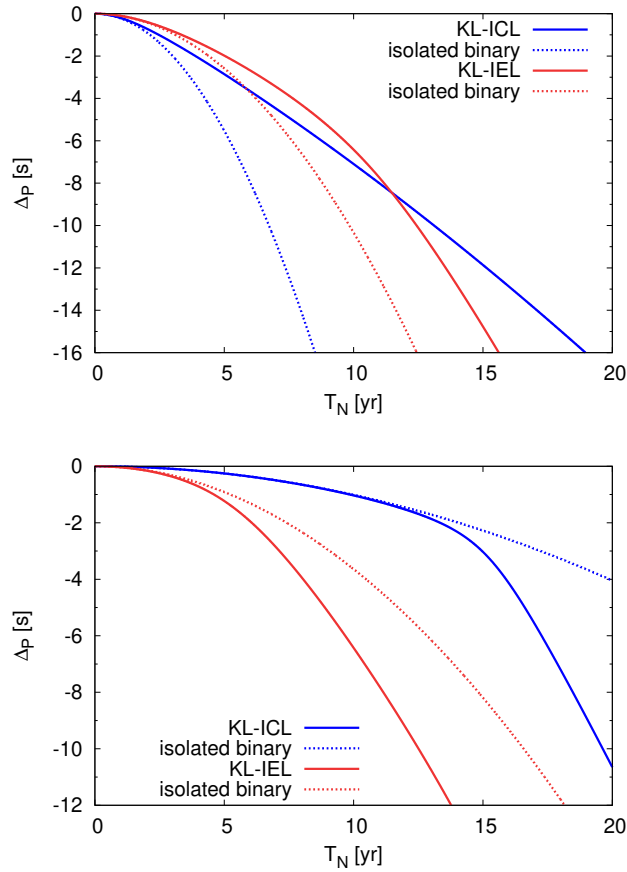
Figure 2.27: The CSPT curve for the libration type of the ZLK oscillation in the PNIB model. The top and bottom panels are the results integrated from the time when the maximum and minimum eccentricities are obtained, respectively. The blue and red solid curves in both the panels correspond to the results of the ICL and IEL types, respectively. The dashed curves are the CSPT curves of the isolated binaries whose parameters are the same as the initial values of the inner binaries of the corresponding types.
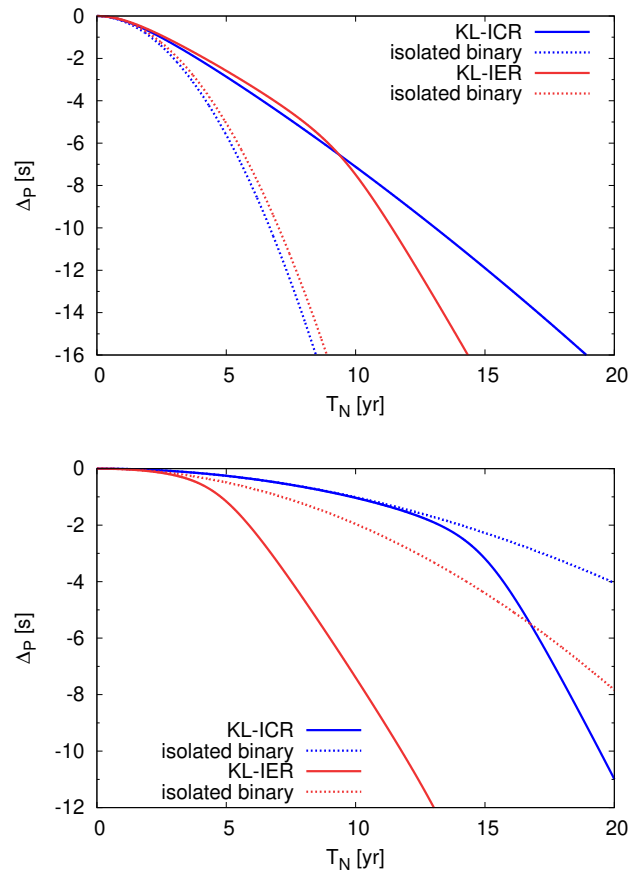
Figure 2.28: The same figure as Fig. 2.27 but for the rotation type. The blue and red solid curves are the results of the ICR and IER types.

avoiding just showing many similar figures. Figs. 2.27 and 2.28 show the results of the libration and rotation types of the ZLK oscillations, respectively. In each panel, the results of the initially circular and eccentric types are shown as the red and blue solid curves, respectively. The top panel in each figure shows the CSPT curves calculated from the time when the maximum eccentricity in each ZLK oscillation type (at $t = 15.21$ yr, $t = 0$ yr, $t = 14.96$ yr and $t = 1.32$ yr for the ICL, IEL, ICR, and IER types, respectively) is obtained, while the bottom panel exhibits those calculated from the time when the eccentricity reaches the minimum value (at $t = 0$ yr, $t = 5.40$ yr, $t = 0$ yr and $t = 6.10$ yr for the ICL, IEL, ICR, and IER types, respectively). By comparing the top and bottom panels, one can find that the CSPT curves become completely different depending on the choice of the initial time of the integration, $T_N = 0$, even for the same model. As a reference, I also show the CSPT curves of the isolated binaries whose parameters are the same as the initial parameters of the inner binaries in corresponding hierarchical triple models, by the red and blue dashed curves. The curves of the isolated binaries are approximated by the quadratic functions as Eq. (2.62).

At first, the CSPT curves of the triple systems coincide with the quadratic curves of corresponding isolated binaries. However, when the eccentricity changes with the ZLK oscillation, the curves of the triple systems bend and the discrepancy from those of the isolated binaries becomes large as already shown in §2.3.2. This is because the decrease of the orbital period of the inner binary due to the GW emission $\dot{P}_{\rm in}$ depends on the orbital eccentricity as given by Eq. (2.52). Hence, the ZLK oscillation of the orbital eccentricity changes $\dot{P}_{\rm in}$ and then causes the large deviation of the CSPT curve from the quadratic curve.

In the top panels of Figs. 2.27 and 2.28, the solid curves at first coincide with the quadratic curves of the eccentric isolated binaries, but they switch to the less steep curves as the eccentricities become smaller by the ZLK oscillation. This feature causes a slower decrease of Δ_P in the triple system compared with that of the isolated eccentric binary. The slope and bending timescale of the red and blue solid curves are different from each other depending on the amplitude and timescale of the ZLK oscillation. On the other hand, in the bottom panels of Figs. 2.27 and 2.28, the switch from the circular curves to the eccentric steeper curves results in the rapid decrease of Δ_P in the triple system curves than those of the isolated circular binaries.

This bending feature may be useful to detect the ZLK oscillation from the observation of pulsars. The shape of the CSPT curve has the information on the amplitude and timescale of the ZLK oscillation in its slope change. The bending of the CSPT curve is clear when the curve is integrated from the minimum eccentricity (bottom panels of Figs. 2.27 and 2.28), but the curve from the maximum eccentricity (top panels of these figures) does not show clear bending. The change of the CSPT curve becomes clearer, however, if the time-derivative of Δ_P is plotted. In Figs. 2.29 and 2.30, the time-evolution of $d\Delta_P/dT_N$ for libration and rotation types of the ZLK oscillations are plotted, respectively. In the top and bottom panels in each figure, $d\Delta_P/dT_N$ is calculated from the time when the maximum and minimum eccentricities are obtained, respectively. In each panel, the red and blue curves are the results of the initially circular and eccentric types. The clear changes of the
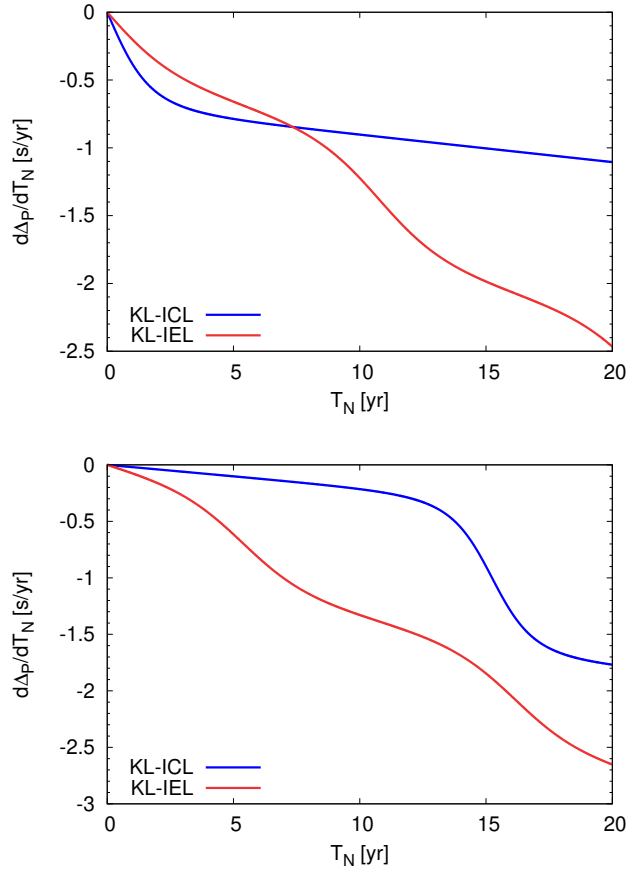
Figure 2.29: Time derivative of the CSPT $d\Delta_P/dt$ calculated for the libration type of the ZLK oscillation for the PNIB model. The top and bottom panels are the results calculated from the time when the maximum and minimum eccentricities are obtained, respectively. The blue and red solid curves are the results of the ICL and IEL types.

slopes of $d\Delta_P/dT_N$ curves are seen in these figures even for the curve integrated from the maximum eccentricity (top panels).

Here the slope of the $d\Delta_P/dT_N$ curve is defined from Eq. (2.61) as

$$S(T_N) = \frac{d^2\Delta_P}{dT_N^2} = \frac{\dot{P}_{\mathrm{in}}(T_N)}{P_{\mathrm{in}}(0)}. \tag{2.69}$$

When the eccentricity gets large, the slope of the $d\Delta_P/dT_N$ curve becomes steep, i.e., the absolute value of $S(T_N)$ becomes large, and vise versa. Hence, the difference between the minimum and maximum values of the slope (S_{min} and S_{max}) indicates the amplitude of the ZLK oscillation.

The magnitude of $S(T_N)$ depends not only on the eccentricity but also on the other model parameters. If a system has a smaller semi-major axis or larger masses in its inner binary, the GW emission rate is larger, which makes the slope of the $d\Delta_P/dT_N$ curve becomes steeper. In Table 2.9, I summarize the minimum slope S_{min} and the maximum slope S_{max} as well as the ZLK timescale T_{ZLK}, which gives
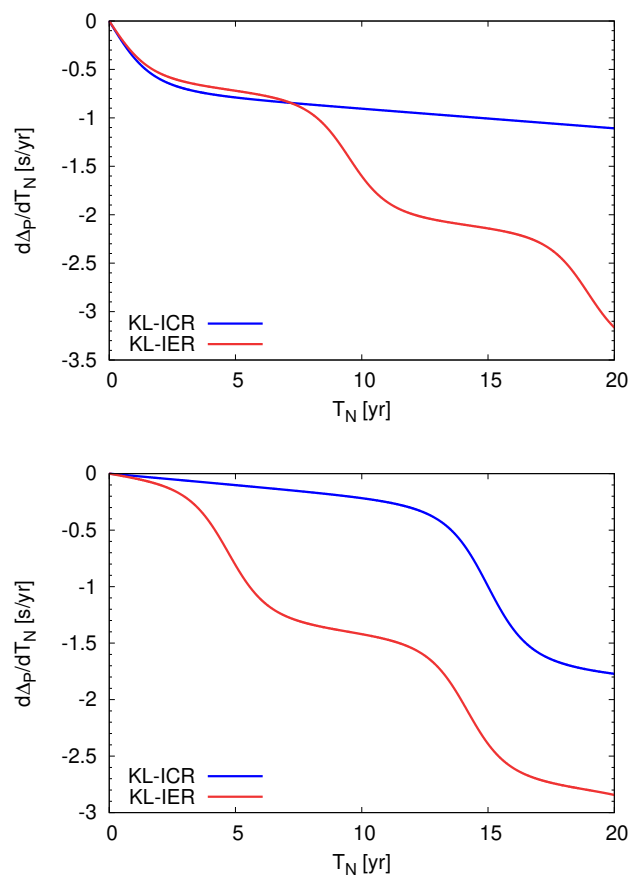
Figure 2.30: The same figures as Fig. 2.27 but for the rotation type of the ZLK oscillation. The blue and red solid curves are the results of the ICR and IER types.

the time interval between minimum and maximum slopes, for all models calculated in this section.

For the Hulse-Taylor binary, the slope is $S_{\mathrm{HT}} \approx -8.57 \times 10^{-2}$. Hence it is expected that the observation of the change of the slope is possible for most models except for the models with the P-BH inner binary. The models with the P-BH inner binary give the smallest absolute values of $S(T_N)$, for which we may need more precise observation to find the CSPT curve. In each model, the difference between $S_{\min}$ and $S_{\max}$ in the IEL type is the smallest of all types of ZLK oscillations. This is because the amplitude of the ZLK oscillation in this type is the smallest as seen in Figs. 2.17 and 2.23.

Next, I discuss the spin-orbit coupling effect mentioned in §2.3.2. The spin-orbit coupling in 1.5PN terms (Barker and O'Connell, 1975) may change the direction of the pulsar rotation axis, which may affect the radio observation. In the other words, the change of the beaming direction of the pulse signal due to the 1.5PN effect may cause the disappearance of the pulsar in the radio observation. Following Liu and Lai (2017, 2018), the evolution of spin in the ZLK oscillation due to the 1.5PN effect is characterized by the "adiabaticity parameter" $\mathcal{A}$ defined as the ratio of the de-Sitter spin precession rate Ω_{SL} to the orbital precession rate by the ZLK oscillation Ω_{L}. The adiabaticity parameter $\mathcal{A}$ is described as

$$\mathcal{A} \equiv \left| \frac{\Omega_{\mathrm{SL}}}{\Omega_{\mathrm{L}}} \right| \simeq 4 \frac{r_{\mathrm{g,in}}}{a_{\mathrm{in}}} \frac{m_1 + \mu_{\mathrm{in}}/3}{m_3} \left(\frac{a_{\mathrm{out}}}{a_{\mathrm{in}}} \right)^3 (1 - e_{\mathrm{out}}^2)^{\frac{3}{2}}, \qquad (2.70)$$

where $\mu_{\mathrm{in}} \equiv m_1 m_2 / (m_1 + m_2)$ is the reduced mass of the inner binary. This parameter is quite similar to $\epsilon^{(\mathrm{1PN})}$ defined in Eq. (2.28). When the ZLK oscillation is successfully obtained in the relativistic three-body system, the condition in Eq. (2.33) derived with $\epsilon^{(\mathrm{1PN})}$ should be satisfied. By rewriting $\epsilon^{(\mathrm{1PN})}$ with $\mathcal{A}$, I find that the adiabaticity parameter $\mathcal{A}$ should satisfy

$$\mathcal{A} \lesssim \frac{m_1(3m_1 + 4m_2)}{(m_1 + m_2)^2}(1 - e_{\mathrm{in}}^2)^{\frac{3}{2}} \leq 3. \qquad (2.71)$$

The adiabaticity parameters of our models are summarized in Table 2.10.

In case that $\mathcal{A} \ll 1$, the spin evolution is classified as "non-adiabatic", that is, the orbital precession by the ZLK oscillation is much faster than the relativistic spin precession, and then the spin axis cannot 'catch up' with the precession of the angular-momentum axis. In the non-adiabatic evolution, the spin axis of the pulsar is expected to be parallelly transported just as in the Newtonian case, which means that the beaming direction of the radio signal is expected not to change so much even when the inclination changes by the ZLK oscillation. The PBB model may correspond to this case. For the other models, $\mathcal{A}$ is still smaller than unity, but not extremely small. In the system with such a mid-range of $\mathcal{A}$, the spin axis of the pulsar is perturbed around its initial direction as shown in Liu and Lai (2018). If the perturbation is large enough so that the beaming angle of the pulsar goes out from the observable range, the radio signal from the pulsar will disappear and will rarely re-appear due to the complicated evolution of the spin direction of the pulsar. If such a disappearance of a pulsar is observed, it will be an important example of the 1.5PN effect on the ZLK oscillation. The critical value of $\mathcal{A}$ for the

Model	Type	T_{KL} [yr]	$S_{\min}[\mathrm{s/yr}^2]$	$S_{\max}[\mathrm{s/yr}^2]$
PNN	ICL	12.7	-0.475	-2.02×10^{-2}
	ICR	12.0	-0.476	-2.02×10^{-2}
	IEL	3.47	-0.215	-0.117
	IER	4.08	-0.423	-3.10×10^{-2}
PNB	ICL	9.18	-0.902	-2.02×10^{-2}
	ICR	8.84	-0.903	-2.02×10^{-2}
	IEL	2.48	-0.223	-0.167
	IER	3.40	-0.480	-2.79×10^{-2}
PNIB	ICL	36.9	-0.442	-2.02×10^{-2}
	ICR	32.6	-0.442	-2.02×10^{-2}
	IEL	10.8	-0.215	-7.28×10^{-2}
	IER	9.50	-0.406	-3.91×10^{-2}
PNSB	ICL	1.98	-1.21	-1.99×10^{-2}
	ICR	1.97	-1.21	-2.02×10^{-2}
	IEL	0.588	-0.255	-0.179
	IER	0.876	-0.527	-2.34×10^{-2}
PBB	ICL	7.05	-2.70×10^{-2}	-4.85×10^{-4}
	ICR	7.99	-2.72×10^{-2}	-4.88×10^{-4}
	IEL	2.23	-6.33×10^{-3}	-4.62×10^{-3}
	IER	3.19	-1.38×10^{-2}	-6.01×10^{-4}
PBIB	ICL	75.1	-2.13×10^{-2}	-4.85×10^{-4}
	ICR	69.9	-2.13×10^{-2}	-4.86×10^{-4}
	IEL	21.6	-5.40×10^{-3}	-3.88×10^{-3}
	IER	29.1	-1.20×10^{-2}	-6.90×10^{-4}
PBSB	ICL	14.0	-2.82×10^{-2}	-4.85×10^{-4}
	ICR	14.5	-2.86×10^{-2}	-4.87×10^{-4}
	IEL	4.09	-6.28×10^{-3}	-4.37×10^{-3}
	IER	5.96	-1.41×10^{-2}	-6.08×10^{-4}
PIBIB	ICL	2.50	-6.04	-0.516
	ICR	2.26	-6.01	-0.518
	IEL	0.899	-6.34	-0.771
	IER	0.491	-10.5	-1.20
PIBSB	ICL	1.20	-11.5	-0.516
	ICR	1.20	-11.5	-0.519
	IEL	0.400	-7.69	-1.48
	IER	0.339	-13.7	-0.915

Table 2.9: The minimum and maximum slopes $S_{\min}$ and $S_{\max}$ and the ZLK timescale T_{ZLK} for all the models calculated in this section are summarized.

name	$\mathcal{A}$
PNN	0.103
PNB	0.075
PNIB	0.282
PNSB	0.0181
PBB	0.0125
PBIB	0.129
PBSB	0.0242
PIBIB	0.683
PIBSB	0.396

Table 2.10:   The adiabaticity parameter $\mathcal{A}$ is calculated for all the models in this section.

disappearance of the signal should depend on the radio emission mechanism of the pulsar, the intensity of the radio signal, the distance to the system, and the opening angle of the radio telescope. If the CSPT is observed for a whole ZLK timescale despite the precession of the spin direction of the pulsar, it means the pulsar is successively observed from some different directions and such observation may give new information about the pulsar.

The hierarchical three-body system which causes the bending of the CSPT curve requires high relative inclination so that the ZLK oscillation occurs. Such highly inclined triple systems may need to be formed by the dynamical interaction in dense environments like globular clusters and galactic nuclei (Kulkarni et al., 1993; Samsing et al., 2014; Zevin et al., 2019). Hence we need a large N-body simulation to estimate event rates of the observation of bending of the CSPT. The distance to the system should be close enough to observe the radio signals, which should also be considered to estimate the event rate. Though such a large N-body simulation considering all factors is beyond the scope of this chapter, it can be expected that the observation of the bending of the CSPT curve may be a rare event. However, as mentioned in §2.3.2, this interesting signal is important not only to confirm the existence of the third body but to provide the first indirect evidence of GW emission from triple systems. The GW emission makes the inner binary more compact. The waveform of GW from such a compact triple system with the ZLK oscillation can be observed by future GW detectors (Hoang et al., 2019; Randall and Xianyu, 2019; Deme et al., 2020; Gupta et al., 2020) like LISA (Amaro-Seoane et al., 2017), DECIGO (Sato et al., 2017), and Big Bang Observer (Harry et al., 2006).

As explained in §2.3.2, for some binary pulsars like the PSR J1840-0643 system (Knispel et al., 2013), the possible existence of the tertiary companion has not been denied. Radio observations of such binary pulsars for a long period may lead to the discovery of the first indirect evidence of the GW emission from the triple system with ZLK oscillations through the detection of the bending of the CSPT curves.

2.5 Summary

In this research, the ZLK oscillations in relativistic hierarchical triple systems with compact objects were studied by taking the 1PN relativistic correction into account. All the models in this research have a pulsar as a component of the inner binary and the CSPT that may be observed in the radio signal from the pulsar was also calculated.

The ZLK mechanism is one of the orbital resonances seen in the hierarchical triple systems and characterized as the secular oscillations of the inner eccentricity and the relative inclination. In the theoretical analysis using the double-averaging method, the amplitude and timescale of the oscillation are determined by the two conserved quantities, θ^2 and C_{ZLK}. When the 1PN effect is taken into account, the value of C_{ZLK} is no longer conserved, and, in addition to θ^2, the new conserved quantity with the 1PN correction that is named as $C_{\mathrm{ZLK}}^{(\mathrm{1PN})}$ determines the amplitude and timescale of the ZLK oscillation. These amplitude and timescale obtained in 1PN calculation should be different from Newtonian ones.

When the eccentricity of the binary pulsar is excited by the ZLK oscillation, it enhances the GW emission from the binary, which changes the shape of the CSPT curve. The theoretical calculation method of the CSPT for a general hierarchical three-body system with a binary pulsar was proposed in this chapter. An example of the CSPT calculation was shown by using the parameters of the PSR J1840-0643 system. This system was chosen because the presence of the third body around this binary pulsar has not been excluded yet. It was confirmed that the ZLK oscillation effect appears in the CSPT as the bending of the curve. I discussed the parameter space of the third body where the bending of the CSPT curve could be observed within 100 yrs.

Then I introduced several models composed of compact objects including a pulsar as a component of the inner binary. By fixing the parameters of some inner binaries, the parameter region of the third body was discussed. The four sets of initial parameters were chosen for each model to realize four different types of the ZLK oscillation: the ICL, IEL, ICR, and IER types.

I calculated the orbital evolution of the models by the direct integration of the 1PN equations of motion. In the four types of ZLK oscillation, the amplitudes and timescales are different, and, in addition, the non-test particle limit effect and the 1PN effect appeared differently. In the result of the model whose mass hierarchy is small (e.g. PNN model), the "conserved" quantities are not conserved but oscillating whereas they should be constant in the double-averaged method with the quadrupole and test-particle limit approximations. It was also found that the amplitudes and timescales obtained in the direct integration do not coincide with those obtained in the double-averaged method. The tendency of these discrepancies is different in the four types of ZLK oscillation. The amplitudes and frequencies of the GW are quite sensitive to the eccentricity, and these differences between eccentricity evolutions in the direct integration and the double-averaged method may be crucial when the GW emission is estimated for the systems with finite masses. It may be better to use the direct integration for the calculation of such systems because one may overestimate or underestimate the maximum or minimum value of the eccentricity

with the double-averaged method.

In the model with large $\epsilon^{(1PN)}$ (e.g. PNIB model), clear differences between the results obtained by the Newtonian and 1PN direct integrations are observed. The 1PN effect appears differently in the four types of ZLK oscillation. Such complicated behavior can be basically understood theoretically by using the double-averaging method with the 1PN corrections. However, in some models (e.g. PNB and PBB models), the irregular periods appear in the ZLK oscillation, which cannot be explained by the double-averaging method. This may be because the conserved quantities of the ZLK oscillation are not exactly constant in the direct integration.

As seen in the example with the PSR J1840-0643 system, the bending of the CSPT curves are caused by the effect of the ZLK oscillation for all the other models. The slope of the curve at each phase reflects the values of the maximum or minimum eccentricity, while the time between two bending points indicates the ZLK timescale. The shapes of the CSPT curves become completely different depending on the choice of the initial time of the integration even for the same model. The bending of the CSPT curve is clear when the curve is integrated from the time when the minimum eccentricity is obtained, but the clear binding is not obtained for the curve calculated from the time when the maximum eccentricity is reached. In the latter case, the time derivative of the CSPT can be a good indicator of the bending.

The system that causes this interesting signal may be rare because such compact hierarchical triple systems with relatively high inclinations may be formed by dynamical interactions in dense environments like globular clusters or the galactic center. However, once such systems are observed with the pulsar signal, it is very important because it is the first indirect observation of the GW from triple systems. It will be the precursor of the direct detection of the waveform of the GW by the future gravitational detectors like LISA, DECIGO, and Big Bang Observer.

Some highly relativistic triple systems should show the spin precession of the pulsar due to the spin-orbit coupling in the 1.5PN effect, which may change the beaming angle of the pulsar. If the beaming angle of the pulsar is perturbed and goes out of the observable range, the radio signals from the pulsar will disappear and rarely appear again. If the disappearance of the signal from a pulsar in the triple system occurs, it will provide one of the important examples of the 1.5PN effect on the ZLK oscillation. On the other hand, if the CSPT is observed for a whole ZLK timescale despite the precession of the spin direction of the pulsar, it means that one successively observes a pulsar from different directions and such observation may give new information about a pulsar.

Chapter 3

Hill Stability Problem

3.1 Purpose

The orbital stability of multi-body systems is one of the oldest problems that have been discussed in celestial mechanics. Numerous astronomers, physicists, and mathematicians have discussed this problem from various perspectives with theoretical and numerical analyses (e.g. Marchal and Bozis (1982); Gladman (1993); Eggleton and Kiseleva (1995); Chambers et al. (1996); Mardling and Aarseth (2001); Deck et al. (2013); Petrovich (2015)). In this chapter, I focus on one of the stability problems called the Hill stability problem and extend the discussion to the general relativistic regime.

The research of the Hill stability problem started from the study on the lunar motion by Hill (1878). It is defined as orbital stability against a close approach, that is, the system is Hill stable if none of the pairs of orbits in the system experiences a close approach for all the time. In Hill's pioneer paper (Hill, 1878) and the following works (Szebehely, 1967; Hénon, 1970; Hénon and Petit, 1986), it was studied for a limited configuration called the circular restricted three-body system, in which two components have much smaller masses than the other one and are orbiting around this massive component on coplanar and circular trajectories. A conserved quantity called Jacobi integral found in such systems was used to analyze the motion. The authors found that if the initial distance between the two orbits Δ is large enough, the two orbiting objects are separated by the so-called forbidden region for all the time, and hence cannot approach each other, which means that the system is Hill stable. A detailed analysis using so-called Hill's coordinates was given by Hénon and Petit (1986).

Various authors have extended the investigation of the Hill stability problem to more and more general three-body systems (see Marchal and Bozis (1982); Milani and Nobili (1983); Roy et al. (1984) and references therein). As a generalization of the idea of the Jacobi integral, they analyzed the allowed and forbidden regions for each component with the relation between the values of the total energy and the angular momentum of the system.

In the 1990s, the Hill stability was focused on in the context of the evolution and formation of planetary systems. After the first discovery of the extra-solar planetary system in 1992 (Wolszczan and Frail, 1992), Gladman (1993) refined the sufficient

condition of the Hill stability for general three-body systems derived by Marchal and Bozis (1982) into simpler inequalities with respect to the orbital separations under several approximations appropriate for the planetary systems. This simple sufficient condition has been broadly used in planetary science.

In 1996, Chambers et al. (1996) explored the Hill stability for four- and more-than-four-body systems with numerical simulations. It was surprising that the sufficient condition for the Hill stability seems not to exist for these more-than-three-body systems. Instead, they obtained a log-linear relation between the initial orbital separation Δ and the time that it takes the system to experience a close approach $T_{\rm stab}$. The limited configurations that three components with small masses orbit around a massive object in coplanar and circular orbits were assumed in their pioneer work, and many authors have expanded the research considering different configurations: elliptical orbits (Ito and Tanikawa, 1999; Chatterjee et al., 2008; Smith and Lissauer, 2009; Pu and Wu, 2015), noncoplanar orbits (Marzari and Weidenschilling, 2002), unequal initial orbital separations (Marzari, 2014), and somewhat more massive planets (Morrison and Kratter, 2016). The relation between the system scale Δ and the onset time of the instability $T_{\rm stab}$ obtained from these researches have been applied to the studies of the formation of planetary systems (Chambers and Wetherill, 1998; Iwasaki and Ohtsuki, 2006; Zhou et al., 2007), by interpreting $T_{\rm stab}$ as the timescale for the collision of planetesimals.

So far, almost all works about the Hill stability problem have used Newtonian mechanics for their discussions. It is fine because their main targets were satellites, planets, and planetesimals. However, if one considers multi-body systems composed of compact objects like black holes (BH), neutron stars (NS), and white dwarfs in tight orbits, Newtonian mechanics is no longer appropriate and general relativity must be taken into account.

As introduced in §1.2, such relativistic multi-body system has already been observed (Ransom et al., 2014), and, as discussed in Chapter 2, more discoveries through GW (Hoang et al., 2019; Randall and Xianyu, 2019; Deme et al., 2020; Gupta et al., 2020) and radio observations (Suzuki et al., 2019, 2021) are also expected. It has been pointed out that the multi-body interactions between compact objects in these relativistic systems are definitely important to make compact binaries that experience coalescence within the Hubble time (Samsing et al., 2014; Leigh et al., 2016, 2017; Liu and Lai, 2017; Zevin et al., 2019). The multi-body interactions in dense environments like globular clusters or galactic centers have been investigated with large-scale N-body numerical simulations (Secunda et al., 2019; Fragione and Antonini, 2019) and the effect of the presence of supermassive black holes (SMBH) or intermediate-mass black holes (IMBH) at the center of such environments have been also explored (Trani et al., 2019a; Fragione and Bromberg, 2019; Trani et al., 2019b).

Although more and more attention has been paid to the studies of the relativistic multi-body systems, few types of research have been devoted to a systematic examination of the stability problem in general relativity. One exception is the paper by Ge and Alexander (1991), but their theoretical analysis can be applied only to the Schwarzschild geometry, whose application to different configurations is not easy.

The purpose of this chapter is hence to investigate the effect of general relativity

on the Hill stability. I use the PN approximation instead of the fully relativistic gravity as in Ge and Alexander (1991) to make the application to different configurations easier. As a first step, I address only relativistic three-body systems to obtain the sufficient condition for the relativistic Hill stability, and only the 1PN effect is taken into account. By limiting the configurations to have an SMBH or IMBH at the center of the system and two orbiting objects with much smaller masses, for simplicity, I successfully extend the theoretical Newtonian analysis in the previous works to the 1PN gravity and give approximated sufficient conditions of the relativistic Hill stability. Other configurations, more-than-three-body systems, and higher-order PN effects will be discussed in future works.

Numerical simulations are also conducted with the 1PN equations of motion to test the approximated sufficient conditions. I show that the systems are more unstable in the sense of the Hill stability in the relativistic calculation than in the Newtonian one and that the theoretical and numerical results are consistent with each other. The approximated sufficient conditions will be useful not only to predict the stability of relativistic three-body systems but also to analyze the results of large-scale N-body simulations of dense environments like globular clusters.

In this chapter, first, in §3.2, I review the previous studies of the sufficient condition of the Hill stability problem discussed in Newtonian mechanics. Second, in §3.3, I explain the analyses with the 1PN equations: I introduce the theoretical analysis to give the approximated sufficient conditions of the relativistic Hill stability, and, subsequently, the method for the numerical simulations to test the stability conditions are explained. The results and discussions are presented in §3.4. I summarize this chapter in §3.5.

3.2 Review of Newtonian Analyses

In this section, I review several important results in previous research about the Hill stability done in Newtonian mechanics. First I derive an important typical distant scale called Hill radius in §3.2.1. After that, in §3.2.2, I introduce the derivation of the Newtonian sufficient condition of the Hill stability of the general three-body systems and subsequently show the simpler description obtained assuming a limited configuration.

3.2.1 Hill radius

In this section, an important distant scale called Hill radius is derived. It is obtained from the analysis of the motion of a test particle moving around a binary system with a circular orbit. The derivation is also explained in detail in e.g. Murray and Dermott (2000).

Here the position of the test particle is denoted as $\boldsymbol{r}_{\mathrm{t}}$ and those of the massive components are written as $\boldsymbol{r}_1$ and $\boldsymbol{r}_2$. The masses of the components of the binary are denoted as m_1 and m_2. In the inertial frame, the equations of motion of the test particle are written as

$$\frac{d^2\boldsymbol{r}_{\mathrm{t}}}{dt^2} = -\frac{\partial U}{\partial \boldsymbol{r}_{\mathrm{t}}}, \tag{3.1}$$
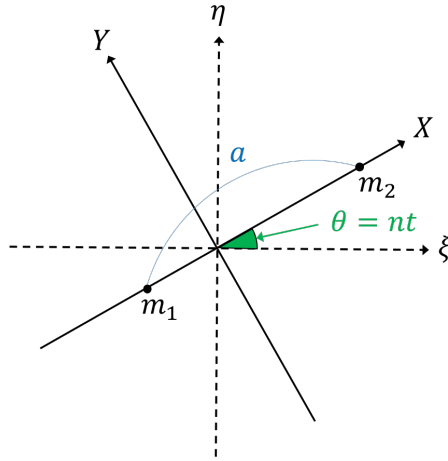
Figure 3.1:   The configuration of the coordinates on the orbital plane. The coordinates in the inertial frame are described as ξ and η, and those in the rotating frame are shown as X and Y. The origins of both coordinates are at the center of mass of the binary. The semi-major axis and the mean motion of the outer orbit is denoted as a and n, respectively.

where U is the Newtonian potential defined as

$$U = -\frac{Gm_1}{|\boldsymbol{r}_{\mathrm{t}} - \boldsymbol{r}_1|} - \frac{Gm_2}{|\boldsymbol{r}_{\mathrm{t}} - \boldsymbol{r}_2|}. \tag{3.2}$$

Here I denote the coordinates of $\boldsymbol{r}_{\mathrm{t}}$ in the inertial frame as $\boldsymbol{r}_{\mathrm{t}} = (\xi, \eta, \zeta)$ and consider a rotating frame that rotates with the outer circular orbit $\boldsymbol{r}_{\mathrm{t}}^* = (X, Y, Z)$. I set the origin of both the coordinates at the center of mass of the binary and the ξ-η (X-Y) plane as the orbital plane of the binary. The ζ-axis coincides with the Z-axis. The configuration on the orbital plane is shown in Fig. 3.1. The semi-major axis and the mean motion of the binary orbit are denoted as a and n in the figure, respectively. The relations between the two coordinates are given as

$$\begin{aligned}
\xi &= X\cos\theta - Y\sin\theta, & \text{(3.3)} \\
\eta &= X\sin\theta + Y\cos\theta, & \text{(3.4)} \\
\zeta &= Z. & \text{(3.5)}
\end{aligned}$$

The acceleration of the test particle is calculated from these equations as

$$\begin{aligned}
\ddot{\xi} &= \ddot{X}\cos\theta - \ddot{Y}\sin\theta - 2n\dot{X}\sin\theta - 2n\dot{Y}\cos\theta \\
&\quad -n^2 X\cos\theta + n^2 Y\sin\theta, & \text{(3.6)} \\
\ddot{\eta} &= \ddot{X}\sin\theta + \ddot{Y}\cos\theta + 2n\dot{X}\cos\theta - 2n\dot{Y}\sin\theta \\
&\quad -n^2 X\sin\theta + n^2 Y\cos\theta. & \text{(3.7)} \\
\ddot{\zeta} &= \ddot{Z}. & \text{(3.8)}
\end{aligned}$$

The acceleration can also be calculated from the equation of motion (Eq. (3.1)) as

$$\ddot{\xi} = -\frac{\partial X}{\partial \xi}\frac{\partial U}{\partial X} - \frac{\partial Y}{\partial \xi}\frac{\partial U}{\partial Y} = -\cos\theta\frac{\partial U}{\partial X} + \sin\theta\frac{\partial U}{\partial Y}, \tag{3.9}$$

$$\ddot{\eta} = -\frac{\partial X}{\partial \eta}\frac{\partial U}{\partial X} - \frac{\partial Y}{\partial \eta}\frac{\partial U}{\partial Y} = -\sin\theta\frac{\partial U}{\partial X} - \cos\theta\frac{\partial U}{\partial Y}, \tag{3.10}$$

$$\ddot{\zeta} = -\frac{\partial Z}{\partial \zeta}\frac{\partial U}{\partial Z} = -\frac{\partial U}{\partial Z}. \tag{3.11}$$

By using Eqs. (3.6) to (3.11), one can erase θ from the equations and obtain the equations of motion in the rotating frame as

$$\ddot{X} - 2n\dot{Y} - n^2 X = -\frac{\partial U}{\partial X}, \tag{3.12}$$

$$\ddot{Y} + 2n\dot{X} - n^2 Y = -\frac{\partial U}{\partial Y}, \tag{3.13}$$

$$\ddot{Z} = -\frac{\partial U}{\partial Z}. \tag{3.14}$$

The second and third terms in the left-hand sides of Eq. (3.12) and Eq (3.13) correspond to the Coriolis forces and the centrifugal forces, respectively. The latter ones can be written in the potential form by using the centrifugal potential U_{CF} defined as

$$U_{\mathrm{CF}} \equiv -\frac{1}{2}n^2(X^2 + Y^2). \tag{3.15}$$

Hence, the equations of motion of the test particle are rewritten with the total potential $U_{\mathrm{tot}} \equiv U + U_{\mathrm{CF}}$ as,

$$\ddot{X} - 2n\dot{Y} = -\frac{\partial U_{\mathrm{tot}}}{\partial X}, \tag{3.16}$$

$$\ddot{Y} + 2n\dot{X} = -\frac{\partial U_{\mathrm{tot}}}{\partial Y}, \tag{3.17}$$

$$\ddot{Z} = -\frac{\partial U_{\mathrm{tot}}}{\partial Z}. \tag{3.18}$$

By multiplying $\dot{X}$, $\dot{Y}$, and $\dot{Z}$ to Eqs. (3.16), (3.17) and (3.18), respectively, and summing up those values, I obtain

$$\dot{X}\ddot{X} + \dot{Y}\ddot{Y} + \dot{Z}\ddot{Z} = -\frac{\partial U_{\mathrm{tot}}}{\partial X}\frac{dX}{dt} - \frac{\partial U_{\mathrm{tot}}}{\partial Y}\frac{dY}{dt} - \frac{\partial U_{\mathrm{tot}}}{\partial Z}\frac{dZ}{dt} = -\frac{dU_{\mathrm{tot}}}{dt}. \tag{3.19}$$

A conserved quantity called Jacobi integral Γ is calculated by integrating this equation with respect to time as

$$\frac{1}{2}(\dot{X}^2 + \dot{Y}^2 + \dot{Z}^2) + U_{\mathrm{tot}} = const. \equiv \Gamma. \tag{3.20}$$

The first term in the left-hand side of Eq. (3.20) is greater than or equal to zero, which gives

$$U_{\mathrm{tot}} \leq \Gamma. \tag{3.21}$$

The position of the test particle should satisfy this inequality, that is, this inequality gives the allowed region of the motion of the particle. Especially, the criterion curve $U_{\mathrm{tot}} = \Gamma$ is called zero-velocity curve because the criterion is satisfied only when the velocity of the test particle is zero.
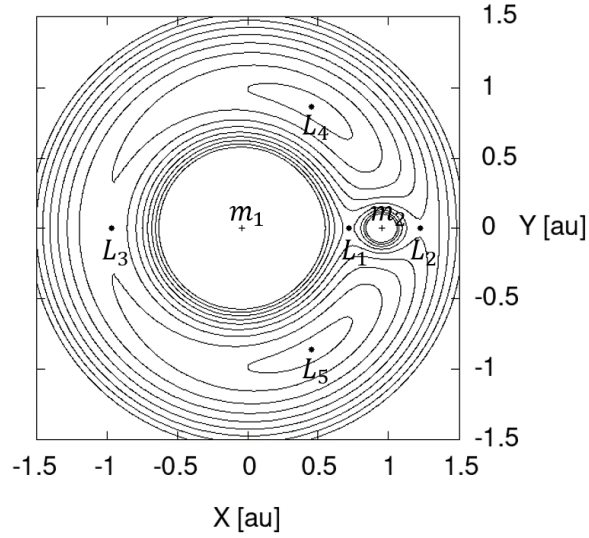
Figure 3.2:   The contour map of U_{tot} on the X-Y plane. The parameters of the binary are chosen as $m_1 = 1.0\,\mathrm{M_\odot}$, $m_3 = 0.05\,\mathrm{M_\odot}$ and $a = 1.0\,\mathrm{au}$. The Lagrange points L_1 to L_5 are plotted as the black dots. Detail explanation of the figure is in the text.

In Fig. 3.2, the contours of U_{tot} on the X-Y plane are plotted for a binary system whose parameters are chosen as $m_1 = 1.0\,\mathrm{M_\odot}$, $m_2 = 0.05\,\mathrm{M_\odot}$ and $a = 1.0\,\mathrm{au}$. The black points L_1 to L_5 in Fig. 3.2 are the special solutions of the equation of motion of the restricted triple systems called the Lagrange points. They are obtained by solving Eqs. (3.16) to (3.18) with the right-hand-side set as zero. The coordinates of the Lagrange points L_4 to L_5 are given as

$$X = a\left\{\frac{1}{2} - \frac{m_1}{m_1 + m_2}\right\}, \;\; Y = \pm\frac{\sqrt{3}}{2}a. \tag{3.22}$$

For the systems with $m_1 > m_2$, the X-coordinates of the Lagrange points L_1 to L_3 are given as the expansions with m_2/m_1 as

$$X_{L_1} = a\left\{\frac{m_1}{m_2 + m_1} - \left(\frac{m_2}{3m_1}\right)^{\frac{1}{3}} + \frac{1}{3}\left(\frac{m_2}{3m_1}\right)^{\frac{2}{3}} - \ldots\right\}, \tag{3.23}$$

$$X_{L_2} = a\left\{\frac{m_1}{m_2 + m_1} + \left(\frac{m_2}{3m_1}\right)^{\frac{1}{3}} + \frac{1}{3}\left(\frac{m_2}{3m_1}\right)^{\frac{2}{3}} - \ldots\right\}, \tag{3.24}$$

$$X_{L_3} = a\left\{-1 + \frac{7}{12}\left(\frac{m_2}{m_1}\right) - \frac{7}{12}\left(\frac{m_2}{m_1}\right)^2 + \ldots\right\}. \tag{3.25}$$

In a test-particle limit $m_2 \ll m_1$, the higher-order terms are neglected and the

coordinates are approximated as

$$X_{L_1} \approx a\left\{1 - \left(\frac{m_2}{3m_1}\right)^{\frac{1}{3}}\right\}, \tag{3.26}$$

$$X_{L_2} \approx a\left\{1 + \left(\frac{m_2}{3m_1}\right)^{\frac{1}{3}}\right\}, \tag{3.27}$$

$$X_{L_3} \approx a\left\{-1 + \frac{7}{12}\left(\frac{m_2}{m_1}\right)\right\}. \tag{3.28}$$

A region inside the eight-shape contour crossing the Lagrange point L_1 is called Roche lobe. In the Roche lobe, the allowed region of a test particle is inside of a counter that corresponds to the given Jacobi constant Γ. The boundary of the allowed region is given as a sphere whose center is on a component of the binary. The largest sphere around the component is called as Hill sphere. As seen in Fig. 3.2, the radius of the Hill sphere can be approximated by the distance between the component and the Lagrange point L_1. Especially, in the test particle limit $m_2 \ll m_1$, the distance between the component with smaller mass and the Lagrange point L_1 is obtained from the coordinate of L_1 in Eq. (3.26) as

$$R_{\text{Hill},2} = \left(\frac{m_2}{3m_1}\right)^{\frac{1}{3}} a. \tag{3.29}$$

Such approximated radius of the Hill sphere is called Hill radius. When the Hill stability problem is discussed, the Hill radius is regarded as a typical scale where the gravitational force from the object can be dominant.

3.2.2 Sufficient Conditions for Three-Body Systems

In this section, I review the derivation of the sufficient condition of the Hill stability for general three-body systems by Marchal and Bozis (1982) and introduce the simplified sufficient conditions for the Hill stability of planetary systems obtained by Gladman (1993).

Marchal and Bozis (1982) defined the generalized Hill stability for general three-body systems as follows: a triple system is stable in the sense of the Hill stability if it can be grouped into a close bounded binary and a third body orbiting it. I remark that even if the third body escapes from the system, the system is Hill stable according to this definition.

The Hill stability of a given three-body system had been discussed especially in the 1970s and 1980s with the topological analyses (see e.g. Hénon (1970); Hénon and Petit (1986); Marchal and Bozis (1982); Milani and Nobili (1983); Roy et al. (1984)). The Hill stability can be judged by the phase space of the third body in the triple system, which is divided into allowed and forbidden regions. If the forbidden region exists between the orbits of the inner binary and the third body in the phase space, they cannot approach each other closely, that is, the system is Hill stable. This means that the existence of the forbidden region between the two orbits works as a sufficient condition for the Hill stability of the three-body system.

Allowed and Forbidden Region from Sundman's Inequality

First, I explain how the allowed and forbidden regions are obtained from the conserved quantities of the three-body system in Newtonian mechanics. This is the generalization of the discussion with the Jacobi integral shown in the last subsection. In the analysis of the three-body system, Sundman's inequality plays a quite important role (see e.g. Ge and Alexander (1991); Ge and Leng (1994)). The inequality is written as

$$\left(\sum_j m_j r_j^2\right)\left(\sum_j m_j v_j^2\right) \geq \left|\sum_j m_j \boldsymbol{r}_j \times \boldsymbol{v}_j\right|^2 + \left|\sum_j m_j \boldsymbol{r}_j \cdot \boldsymbol{v}_j\right|^2. \tag{3.30}$$

In the stability analysis, m_j, $\boldsymbol{r}_j$, and $\boldsymbol{v}_j$ in this inequality normally mean the mass, position, and velocity vectors of the j-th object, respectively. I remark, however, that two vectors can be chosen arbitrarily and m_j can take an arbitrary positive value in fact. The subscript j runs from 1 to an arbitrary integer N, which is chosen to be $N = 3$ in this research. This inequality is proven by using the well-known Cauchy's inequality. The proof is shown in Appendix B.

Here I choose m_j, $\boldsymbol{r}_j$, and $\boldsymbol{v}_j$ to be the mass, position, and velocity vectors as usual. Then the inequality (3.30) can be rewritten with some Newtonian characteristic quantities of the system as

$$2\left(\sum_j m_j r_j^2\right)(\mathcal{H}_{\mathrm{N}} - U_{\mathrm{N}}) \geq J_{\mathrm{N}}^2 + \left|\sum_j m_j \boldsymbol{r}_j \cdot \boldsymbol{v}_j\right|^2, \tag{3.31}$$

where $\mathcal{H}_{\mathrm{N}}$, U_{N}, and J_{N} are the total Hamiltonian, gravitational potential, and the magnitude of the total angular momentum, respectively. These quantities are defined as

$$\mathcal{H}_{\mathrm{N}} = \frac{1}{2}\sum_j m_j v_j^2 + U_{\mathrm{N}}, \tag{3.32}$$

$$U_{\mathrm{N}} = -\frac{1}{2}\sum_i \sum_{j \neq i} \frac{G m_i m_j}{r_{ij}}, \tag{3.33}$$

$$J_{\mathrm{N}} = \left|\sum_j m_j \boldsymbol{r}_j \times \boldsymbol{v}_j\right|, \tag{3.34}$$

where $r_{ij} = |\boldsymbol{r}_i - \boldsymbol{r}_j|$ is the distance between the i-th and j-th objects. The second term on the right-hand side of the inequality (3.31) is positive and I obtain

$$2\left(\sum_j m_j r_j^2\right)(\mathcal{H}_{\mathrm{N}} - U_{\mathrm{N}}) \geq J_{\mathrm{N}}^2. \tag{3.35}$$

Since this inequality depends only on the positions, when two of the three positions are fixed, the condition for the remaining position is given. In other words, the allowed regions of the remaining body are characterized by the conserved quantities of the system $\mathcal{H}_{\mathrm{N}}$ and J_{N} by the inequality (3.35). Hence the Hill stability of a given three-body system can be judged if one knows the conserved quantities of the system and if the positions of two objects are fixed.

Derivation of Sufficient Condition

From the inequality (3.35), Marchal and Bozis (1982) successfully obtained the sufficient condition of the Hill stability of general three-body systems. Here I explain their strategy.

They rewrite the inequality (3.35) by introducing several new parameters describing distances. First, they rewrite the positions in the inequality (3.35) by two distances: the mean quadratic distance ρ and the mean harmonic distance η. These distances are defined as

$$\rho^2 \equiv \frac{m_1 m_2 r_{12}^2 + m_2 m_3 r_{23}^2 + m_3 m_1 r_{31}^2}{m_1 m_2 + m_2 m_3 + m_3 m_1}, \tag{3.36}$$

$$\frac{1}{\nu} \equiv \frac{1}{m_1 m_2 + m_2 m_3 + m_3 m_1} \left(\frac{m_1 m_2}{r_{12}} + \frac{m_2 m_3}{r_{23}} + \frac{m_3 m_1}{r_{31}} \right). \tag{3.37}$$

Another two distances corresponding to the conserved quantities of the system are also introduced: the generalized semi-major axis a_* and the generalized semi-latus rectum p_*. These distances are defined as

$$a_* \equiv -\frac{G(m_1 m_2 + m_2 m_3 + m_3 m_1)}{2\mathcal{H}_{\mathrm{N}}}, \tag{3.38}$$

$$p_* \equiv \frac{(m_1 + m_2 + m_3) J_{\mathrm{N}}^2}{G(m_1 m_2 + m_2 m_3 + m_3 m_1)^2}. \tag{3.39}$$

With these distances, the inequality (3.35) is rewritten as

$$\frac{\rho}{\nu} \geq \frac{\rho}{2a_*} + \frac{p_*}{2\rho}. \tag{3.40}$$

If the generalized semi-major axis a_* is positive (in the case, the total energy $\mathcal{H}_{\mathrm{N}} < 0$), the right-hand side becomes minimum value equal to $\sqrt{p_*/a_*}$ with $\rho = \sqrt{a_* p_*}$ due to the relation between the arithmetic mean and the geometric mean. Hence the inequality (3.40) gives

$$\frac{\rho}{\nu} \geq \sqrt{\frac{p_*}{a_*}}, \tag{3.41}$$

where the right-hand side is written with the conserved quantities. The allowed region of one of the components of the system can be described by mapping the contours of the left-hand side of the inequality (3.41) fixing the positions of the other two components. This is the generalization of the discussion in §3.2.1 with the inequality (3.21).

In Fig. 3.3, I show an example of the color and contour map of ρ/ν on an orbital plane of the binary. Here I fix the parameters of a binary and plot ρ/ν as a function of the position of the third component. The parameters of the binary are the same as those used in Fig. 3.2, but the mass of the third component is set as $m_3 = 0.05\,\mathrm{M}_\odot$ in this plot.

The value of ρ/ν is minimum at the Lagrange points L_4 and L_5, and, on the other hand, it becomes infinitely large at m_1, at m_2, and at infinity. If the value
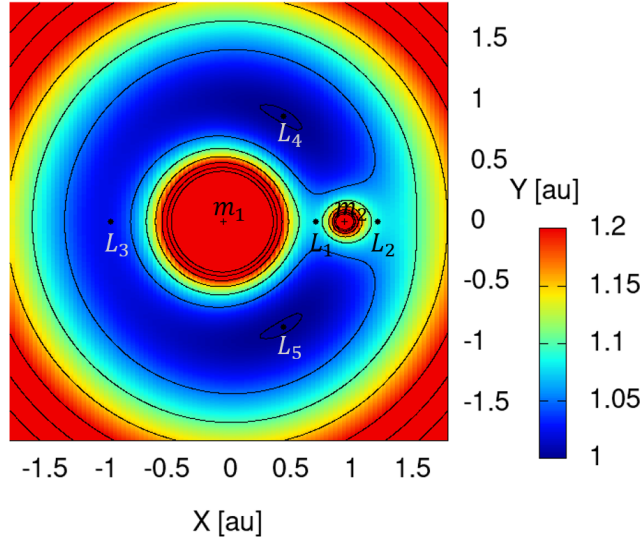
Figure 3.3: The contour and color map of ρ/ν on the orbital plane of a binary. The parameters of the binary are the same as those used in Fig. 3.2. The mass of the third component is $m_3 = 0.05\,\mathrm{M_\odot}$. The Lagrange points L_1 to L_5 are plotted as the black dots.

of $\sqrt{p_*/a_*}$ is large enough, the allowed region of the third body is split into three parts (the reddish region in Fig 3.3). In such a case, the motion in the system can be successfully divided into a binary orbit and a motion of a third body separated from the binary, which means that the system is Hill stable. The critical value to split the allowed region into three parts is given by the value of ρ/ν at Lagrange points L_1, L_2, or L_3, depending on the system. Hence, the sufficient condition of the Hill stability of general three-body systems is given as

$$\frac{p_*}{a_*} > \left[\sup\left\{\frac{\rho}{\nu}(L_1),\ \frac{\rho}{\nu}(L_2),\ \frac{\rho}{\nu}(L_3)\right\}\right]^2. \qquad (3.42)$$

Gladman's Simple Sufficient Conditions

Gladman (1993) rewrote the sufficient condition of the general three-body systems given as the inequality (3.42) as a useful form by limiting the situation to planetary systems, where the mass of the central object overwhelms other objects orbiting it. He also assumed that two orbits in the system are coplanar. Here I introduce his simpler sufficient conditions written with the orbital elements of the system.

For the three-body system with $m_1 \gg m_2$, m_3, as shown by Marchal and Bozis (1982), the critical value of p_*/a_* given in the right-hand side of the inequality (3.42) can be approximated as

$$\left(\frac{p_*}{a_*}\right)_{\mathrm{crit}} \approx 1 + \frac{3^{\frac{4}{3}}m_2 m_3}{m_1^{\frac{2}{3}}(m_2+m_3)^{\frac{4}{3}}}. \qquad (3.43)$$

In addition, in that limited case, the conserved quantities are approximately given as the summation of those of each binary orbit. The conserved quantities are hence

given with the initial orbital elements as

$$\mathcal{H}_{\mathrm{N}} \approx -\frac{Gm_1m_2}{2a_{\mathrm{in}}} - \frac{Gm_1m_3}{2a_{\mathrm{out}}}, \tag{3.44}$$

$$J_{\mathrm{N}}^2 \approx (J_{\mathrm{in}} + J_{\mathrm{out}})^2, \tag{3.45}$$

where the magnitudes of the angular momenta of the inner and outer orbits J_{in} and J_{out} are defined as

$$J_{\mathrm{in}} = \sqrt{G\frac{m_1^2 m_2^2}{m_1 + m_2} a_{\mathrm{in}}(1 - e_{\mathrm{in}}^2)}, \tag{3.46}$$

$$J_{\mathrm{out}} = \sqrt{G\frac{m_1^2 m_3^2}{m_1 + m_3} a_{\mathrm{out}}(1 - e_{\mathrm{out}}^2)}. \tag{3.47}$$

By substituting these values into the inequality (3.42), the sufficient condition becomes

$$(\mu_2 + \mu_3)^{-3}\left(\mu_2 + \frac{\mu_3}{1+\delta}\right)\left(\mu_2\sqrt{1 - e_{\mathrm{in}}^2} + \mu_3\sqrt{1 - e_{\mathrm{out}}^2}\sqrt{1+\delta}\right)^2$$
$$> 1 + 3^{\frac{4}{3}}\frac{\mu_2\mu_3}{(\mu_2 + \mu_3)^{\frac{4}{3}}}, \tag{3.48}$$

where $\mu_i \equiv m_i/m_1$ $(i = 2, 3)$ is the ratio of the mass of the orbiting objects to that of the central object, and $\delta \equiv (a_{\mathrm{out}} - a_{\mathrm{in}})/a_{\mathrm{in}}$ is the normalized difference between two semi-major axes.

This description becomes even simpler under the condition that the two orbiting objects have equal masses $\mu = \mu_2 = \mu_3$, by expanding Eq. (3.48) with μ and e and taking the lowest order. The sufficient conditions obtained in Gladman (1993) are classified into three cases:

1. for initially circular orbits $(e_{\mathrm{in}}, e_{\mathrm{out}} = 0)$

$$\delta > 3\mu^{\frac{1}{3}}, \tag{3.49}$$

2. for initially low eccentric orbits $(e_{\mathrm{in}}, e_{\mathrm{out}} \leq \mu^{\frac{1}{3}})$

$$\delta > \sqrt{\frac{8}{3}(e_{\mathrm{in}}^2 + e_{\mathrm{out}}^2) + 9\mu^{\frac{2}{3}}}, \tag{3.50}$$

3. for initially highly eccentric orbits $(e_{\mathrm{in}} = e_{\mathrm{out}} = e > \mu^{\frac{1}{3}})$

$$\delta > \left(\sqrt{\frac{3 + e^2}{2(1 - e^2)} - \frac{1}{2}\sqrt{\frac{9 - e^2}{1 - e^2}}} + \frac{1}{2}\sqrt{\frac{9 - e^2}{1 - e^2}} - \frac{1}{2}\right)^2 - 1. \tag{3.51}$$

In §3.4, I compare these conditions with the approximated sufficient conditions obtained in this chapter.

3.3 Post-Newtonian Analysis

In this section, I present the method to give the sufficient condition of the 1PN Hill stability following Suzuki et al. (2020). First, I explain the 1PN analysis with Sundman's inequality to give the allowed and forbidden regions for three-body systems in §3.3.1. Instead of the theoretical way done by Marchal and Bozis (1982), I obtained the 1PN sufficient condition numerically by using some results of the numerical simulations of three-body systems with an SMBH or IMBH. I explain the method of the numerical simulations in §3.3.2.

3.3.1 1PN Analysis with Sundman's Inequality

In this subsection, I expand the analysis with Sundman's inequality from the Newtonian to 1PN discussion. I use the 1PN Hamiltonian and linear momentum given in Eqs. (1.160) and (1.161), respectively. The total angular momentum $\boldsymbol{J}_{\mathrm{1PN}}$ is defined as

$$\boldsymbol{J_{1PN}} = \sum_j \boldsymbol{r}_j \times \boldsymbol{P}_j. \tag{3.52}$$

The total energy $\mathcal{H}_{\mathrm{1PN}}$ in Eq. (1.160) and total angular momentum $\boldsymbol{J}_{\mathrm{1PN}}$ in Eq. (3.52) are conserved quantities of the system.

For simplicity, I limit the configurations of the systems to the triple systems that have a massive central object like an SMBH or IMBH whose mass is denoted as m_1, and two orbiting objects with much smaller masses, that is, $m_2, m_3 \ll m_1$. In this limited case, it can be assumed that the barycenter of the system exists almost on the central object. It means that if the coordinate origin is set on the barycenter, the following relations approximately hold:

$$\boldsymbol{r}_1 \approx \boldsymbol{0}, \tag{3.53}$$
$$\boldsymbol{r}_2 \approx \boldsymbol{r}_2 - \boldsymbol{r}_1, \tag{3.54}$$
$$\boldsymbol{r}_3 \approx \boldsymbol{r}_3 - \boldsymbol{r}_1, \tag{3.55}$$
$$\boldsymbol{v}_1 \approx \boldsymbol{0}, \tag{3.56}$$
$$\boldsymbol{v}_2 \approx \boldsymbol{v}_2 - \boldsymbol{v}_1, \tag{3.57}$$
$$\boldsymbol{v}_3 \approx \boldsymbol{v}_3 - \boldsymbol{v}_1. \tag{3.58}$$

By using these approximations, the 3-body 1PN Hamiltonian can be approximated with the Hamiltonian of the relative motion as in the following form:

$$\mathcal{H}_{\mathrm{1PN}} \approx m_2 \mathcal{H}_{\mathrm{rel}}^{(1-2)} + m_3 \mathcal{H}_{\mathrm{rel}}^{(1-3)} - \frac{Gm_2 m_3}{r_{23}}, \tag{3.59}$$

where $\mathcal{H}_{\mathrm{rel}}^{(1-2)}$ and $\mathcal{H}_{\mathrm{rel}}^{(1-3)}$ are the 1PN specific Hamiltonians for the relative motions $\boldsymbol{r}_2 - \boldsymbol{r}_1$ and $\boldsymbol{r}_3 - \boldsymbol{r}_1$, respectively. Here I neglected 1PN correction terms proportional to $m_2 m_3$ or $m_1 m_2 m_3$ because they have the order of $m_2(\sim m_3)/m_1 \times$ the dominant 1PN corrections, $m_2 \mathcal{H}_{\mathrm{rel}}^{(1-2)}$ and $m_3 \mathcal{H}_{\mathrm{rel}}^{(1-3)}$. Note that these terms for the models in this chapter are confirmed by direct numerical evaluations to be always smaller by a factor of 10^6. Each 1PN specific Hamiltonian $\mathcal{H}_{\mathrm{rel}}$, as well as the specific

linear momentum $\boldsymbol{p}$ of the relative motion $\boldsymbol{r} = \boldsymbol{r}_i - \boldsymbol{r}_1$, were derived by Richardson and Kelly (1988) as shown in Eqs. (1.162) and (1.163). In Eq. (1.162), with the approximation $m_2, m_3 \ll m_1$, I make the following replacements: $G(m_1 + m_2) \approx Gm_1$, $\boldsymbol{r}_2 - \boldsymbol{r}_1 \approx \boldsymbol{r}_2$ and $\boldsymbol{v}_2 - \boldsymbol{v}_1 \approx \boldsymbol{v}_2$. Denoting the terms of the order of $1/c^2$ in $\mathcal{H}_{\mathrm{rel}}$ as $X(\boldsymbol{r}, \boldsymbol{p})$, $\mathcal{H}_{\mathrm{rel}}^{(1-2)}$, and $\mathcal{H}_{\mathrm{rel}}^{(1-3)}$ are written as

$$\mathcal{H}_{\mathrm{rel}}^{(1-2)} \approx \frac{1}{2}\boldsymbol{p}_2 \cdot \boldsymbol{p}_2 - \frac{Gm_1}{r_{12}} + X^{(1-2)}(\boldsymbol{r}_2, \boldsymbol{p}_2), \tag{3.60}$$

$$\mathcal{H}_{\mathrm{rel}}^{(1-3)} \approx \frac{1}{2}\boldsymbol{p}_3 \cdot \boldsymbol{p}_3 - \frac{Gm_1}{r_{13}} + X^{(1-3)}(\boldsymbol{r}_3, \boldsymbol{p}_3). \tag{3.61}$$

By substituting these expressions in Eq. (3.59), the total Hamiltonian is rewritten as

$$\mathcal{H}_{\mathrm{1PN}} \approx \frac{1}{2}m_2 p_2^2 + \frac{1}{2}m_3 p_3^2 + U_{\mathrm{N}} + m_2 X^{(1-2)}(\boldsymbol{r}_2, \boldsymbol{p}_2) + m_3 X^{(1-3)}(\boldsymbol{r}_3, \boldsymbol{p}_3), \tag{3.62}$$

where U_{N} is the Newtonian gravitational potential defined in Eq.(3.33).

I use Sundman's inequality shown in Eq. (3.30) for 1PN analysis. As remarked in §3.2.2, the two vectors in this inequality can be chosen arbitrarily. In the 1PN analysis, I choose the specific linear momentum $\boldsymbol{p}$ instead of the velocity $\boldsymbol{v}$. Then the Sundman's inequality is written as

$$\left(\sum_j m_j r_j^2\right)\left(\sum_j m_j p_j^2\right) \geq \left|\sum_j m_j \boldsymbol{r}_j \times \boldsymbol{p}_j\right|^2 + \left|\sum_j m_j \boldsymbol{r}_j \cdot \boldsymbol{p}_j\right|^2. \tag{3.63}$$

Note that the terms with $j = 1$ are almost vanishing due to the approximations I imposed here. Following the procedure in §3.2.2, this inequality is further rewritten in terms of the characteristic quantities of the system as

$$2\left(\sum_j m_j r_j^2\right)\left(\mathcal{H}_{\mathrm{1PN}} - U_{\mathrm{N}} - m_2 X^{(1-2)}(\boldsymbol{r}_2, \boldsymbol{p}_2) - m_3 X^{(1-3)}(\boldsymbol{r}_3, \boldsymbol{p}_3)\right) \geq J_{\mathrm{1PN}}^2. \tag{3.64}$$

The above inequality is the 1PN counterpart of the Newtonian inequality (3.35). However, this is not convenient compared with the Newtonian one, because the functions $X^{(1-2)}(\boldsymbol{r}_2, \boldsymbol{p}_2)$ and $X^{(1-3)}(\boldsymbol{r}_3, \boldsymbol{p}_3)$ depend not only on the position but also on the specific linear momentum. In order to obtain the allowed and forbidden regions as in the Newtonian discussion, they need to be approximated somehow with the functions of the position alone. Here I propose to apply the 1PN virial theorem derived by Chandrasekhar and Contopoulos (1963) individually to the two-body systems consisting of the central object and one of the orbiting objects:

$$v_i^2 \approx \frac{Gm_1}{r_i}\left(1 - \frac{3}{c^2}\frac{Gm_1}{r_i}\right) \tag{3.65}$$

In fact, the last term of the 1PN virial approximation in Eq. (3.65) can be neglected because it corresponds to the higher-order PN term when it is employed in the terms that are already of the 1PN order. When the higher-order term is neglected,

this approximation is reduced to the Newtonian virial relation. Strictly speaking, the virial relation holds only for the average over the orbital cycle unless the orbit is circular. In this chapter, however, this relation is used even for elliptic orbits pointwise as an approximation, which is confirmed to work well in the numerical simulation.

By substituting this approximation in Eq. (1.163) and using the result in the definition of $X^{(1-i)}(\boldsymbol{r}_i, \boldsymbol{p}_i)$, I obtain

$$X^{(1-i)}(\boldsymbol{r}_i, \boldsymbol{p}_i) \approx -\frac{9}{8}\frac{1}{c^2}\frac{G^2 m_1^2}{r_i^2} + \mathcal{O}\left(\frac{v_i^4}{c^4}\right). \tag{3.66}$$

I remark that the angle θ between $\boldsymbol{r}_i$ and $\boldsymbol{p}_i$ which appears as $p^2(3 + \chi \cos^2\theta)$ in the calculation of $X^{(1-i)}(\boldsymbol{r}_i, \boldsymbol{p}_i)$, can be neglected because $\chi \ll 1$. By using this approximated $X^{(1-i)}(\boldsymbol{r}_i, \boldsymbol{p}_i)$, Eq. (3.64) is also approximated as

$$2\left(\sum_j m_j r_j^2\right)\left\{\mathcal{H}_{1\text{PN}} - U_\text{N} + \frac{9}{8}\frac{G^2 m_1^2}{c^2}\left(\frac{m_2}{r_2^2} + \frac{m_3}{r_3^2}\right)\right\} \geq J_{1\text{PN}}^2. \tag{3.67}$$

This inequality depends only on the position and works as the 1PN counterpart of the Newtonian inequality (3.35).

Next, we bound $\mathcal{H}_{1\text{PN}}$ from above and $J_{1\text{PN}}^2$ from below in the inequality (3.67) with the initial orbital elements. First, with the virial relation given in Eq. (3.65), the total Hamiltonian $\mathcal{H}_{1\text{PN}}$ is approximately written as

$$\mathcal{H}_{1\text{PN}} \approx \frac{1}{2}m_2 v_2^2 + \frac{1}{2}m_3 v_3^2 + U_\text{N} + \frac{19}{8}\frac{1}{c^2}\left(\frac{G^2 m_1^2 m_2^2}{r_2^2} + \frac{G^2 m_1^2 m_3^2}{r_3^2}\right) \tag{3.68}$$

As in Gladman (1993), the Newtonian orbital energy can be rewritten with the initial semi-major axes a_in and a_out as

$$\frac{1}{2}m_2 v_2^2 - \frac{Gm_1 m_2}{r_2} \approx \frac{1}{2}\frac{m_1 m_2}{m_1 + m_2}v_{12}^2 - \frac{Gm_1 m_2}{r_{12}} = -\frac{Gm_1 m_2}{2a_\text{in}}, \tag{3.69}$$

$$\frac{1}{2}m_3 v_2^3 - \frac{Gm_1 m_3}{r_3} \approx \frac{1}{2}\frac{m_1 m_3}{m_1 + m_3}v_{13}^2 - \frac{Gm_1 m_3}{r_{13}} = -\frac{Gm_1 m_3}{2a_\text{out}}, \tag{3.70}$$

The gravitational interaction term between m_2 and m_3, $Gm_2 m_3/r_{23}$, can be neglected because it is much smaller than the two orbital energies. In order to bound the Hamiltonian from above, the last term in Eq. (3.68) can be evaluated with the following relation

$$\frac{1}{r^2} \leq \frac{1}{a^2(1-e)^2}. \tag{3.71}$$

In this evaluation, I used the periastron distance in the Kepler orbit as the minimum distance between the central and orbiting objects. By substituting this evaluation into Eq. (3.68), the total Hamiltonian is now estimated from above as

$$\mathcal{H}_{1\text{PN}} \lesssim -\frac{Gm_1 m_2}{2a_\text{in}} - \frac{Gm_1 m_3}{2a_\text{out}} + \frac{19}{8}\frac{G^2 m_1^2}{c^2}\left\{\frac{m_2}{a_\text{in}^2(1-e_\text{in})^2} + \frac{m_3}{a_\text{out}^2(1-e_\text{out})^2}\right\}. \tag{3.72}$$

The square of the magnitude of the angular momentum $J^2_{1\text{PN}}$ can be estimated similarly. The total angular momentum $\boldsymbol{J}_{1\text{PN}}$ is written as

$$\boldsymbol{J}_{1\text{PN}} = \boldsymbol{J}_{\text{in,N}} \left[1 + \frac{1}{c^2} \left(\frac{v_2^2}{2} + \frac{3Gm_1}{r_2} \right) \right] + \boldsymbol{J}_{\text{out,N}} \left[1 + \frac{1}{c^2} \left(\frac{v_3^2}{2} + \frac{3Gm_1}{r_3} \right) \right], \quad (3.73)$$

where $\boldsymbol{J}_{\text{in,N}} = m_2 \boldsymbol{r}_2 \times \boldsymbol{v}_2$ and $\boldsymbol{J}_{\text{out,N}} = m_3 \boldsymbol{r}_3 \times \boldsymbol{v}_3$ are the Newtonian angular momenta of the inner and outer orbits, respectively. Their magnitudes are expressed with the orbital elements as shown in Eqs. (3.46) and (3.47). Then the square of the magnitude of the total angular momentum $J^2_{1\text{PN}}$ is given as

$$\begin{aligned}
J^2_{1\text{PN}} &= J^2_{\text{in,N}} \left[1 + \frac{2}{c^2} \left(\frac{v_2^2}{2} + \frac{3Gm_1}{r_2} \right) \right] + J^2_{\text{out,N}} \left[1 + \frac{2}{c^2} \left(\frac{v_3^2}{2} + \frac{3Gm_1}{r_3} \right) \right] \\
&\quad + 2\boldsymbol{J}_{\text{in,N}} \cdot \boldsymbol{J}_{\text{out,N}} \left[1 + \frac{1}{c^2} \left\{ \frac{v_2^2 + v_3^2}{2} + 3Gm_1 \left(\frac{1}{r_2} + \frac{1}{r_3} \right) \right\} \right] \\
&\quad + \mathcal{O}\left(\frac{v^4}{c^4} \right).
\end{aligned} \quad (3.74)$$

The scalar product of the inner and outer angular momenta in the second line of Eq. (3.74) can be calculated as $\boldsymbol{J}_{\text{in,N}} \cdot \boldsymbol{J}_{\text{out,N}} = J_{\text{in,N}} J_{\text{out,N}}$ because the coplanar prograde orbits are considered here and the two angular momenta are aligned with each other. I use the 1PN virial relation given in Eq. (3.65) again and Eq. (3.74) becomes

$$\begin{aligned}
J^2_{1\text{PN}} &\approx J^2_{\text{in,N}} \left[1 + 7\frac{1}{c^2}\frac{Gm_1}{r_2} \right] + J^2_{\text{out,N}} \left[1 + 7\frac{1}{c^2}\frac{Gm_1}{r_3} \right] \\
&\quad + 2J_{\text{in,N}} J_{\text{out,N}} \left[1 + \frac{7}{2}\frac{Gm_1}{c^2} \left(\frac{1}{r_2} + \frac{1}{r_3} \right) \right] + \mathcal{O}\left(\frac{v^4}{c^4} \right).
\end{aligned} \quad (3.75)$$

In order to bound $J^2_{1\text{PN}}$ from below, the following relation is employed:

$$\frac{1}{r} \geq \frac{1}{a(1+e)}. \quad (3.76)$$

The maximum value of the distance is set as the apoastron distance in the Kepler orbit. Then the total angular momentum squared is estimated as

$$\begin{aligned}
J^2_{1\text{PN}} &\gtrsim J^2_{\text{in,N}} \left[1 + \frac{7}{c^2}\frac{Gm_1}{a_{\text{in}}(1 + e_{\text{in}})} \right] + J^2_{\text{out,N}} \left[1 + \frac{7}{c^2}\frac{Gm_1}{a_{\text{out}}(1 + e_{\text{out}})} \right] \\
&\quad + 2J_{\text{in,N}} J_{\text{out,N}} \left[1 + \frac{7}{2}\frac{Gm_1}{c^2} \left\{ \frac{1}{a_{\text{in}}(1 + e_{\text{in}})} + \frac{1}{a_{\text{out}}(1 + e_{\text{out}})} \right\} \right], \quad (3.77)
\end{aligned}$$

By employing these approximations of the conserved quantities shown in the inequalities (3.72) and (3.77) in the inequality (3.67) and by fixing the positions of two objects, I obtain the allowed and forbidden regions of the remaining body. As explained in the Newtonian discussion in §3.2.2, the existence of the forbidden region between two orbits may be interpreted as a sufficient condition of the 1PN

Hill stability. Note that this 1PN evaluation can be applied only to the triple system with a massive central object and two orbiting objects with much smaller masses.

In the Newtonian discussion in §3.2.2, the sufficient condition of the Hill stability is obtained by rewriting the inequality with an adequate parameterization. Finding such a good parameterization in the 1PN inequality (3.67) is a big challenge, however, and will be deferred to future work. Instead of the theoretical approach with the parameterization, here I evaluate the 1PN inequalities (3.67), (3.72), and (3.77) numerically to obtain the approximated sufficient conditions for some models. I also compare the approximated sufficient condition with the results of numerical three-body simulations in the 1PN approximation to validate the 1PN criterion.

3.3.2   Numerical Simulations

In order to obtain the approximated sufficient condition of the 1PN Hill stability numerically and to test it, I conduct some numerical simulations following Chambers et al. (1996), who computed Newtonian orbital evolutions of four or more-than-four-body systems with various initial orbital separations until the instability occurs in the sense of the Hill stability. The onset of the instability was judged from the orbital separation during the simulation. From the relation between the initial orbital separation and the time when the instability occurs, the condition needed for the Hill Stability is obtained.

I conduct both the Newtonian and 1PN simulations and compare the results. Note that neglected higher-order PN terms may have some important effects on the Hill stability. For example, the Lense-Thrring effect caused by 1.5PN terms have been pointed out to affect the orbital evolution of the hierarchical triple systems (see Fang and Huang (2019); Fang et al. (2019); Liu et al. (2019) and also §2.3.3 in this thesis) and may also affect the Hill stability. The 2.5PN order effects corresponding to the GW emission may be also important because it extracts energy from the inner orbit more efficiently than from the outer orbit (Peters and Mathews, 1963) and, as a result, the orbital separation will become larger, which should affect the Hill stability. In this research, however, I ignore these interesting higher-order PN effects and focus on the 1PN effect as a first step. I will give a rough estimation of these higher PN effects in §3.4, though. They will be investigated in detail in future works.

Our numerical models of relativistic three-body systems are divided into two groups: the SMBH and IMBH groups, where the models have an SMBH and an IMBH as their central object, respectively. Each group has three models: the circular, small-eccentricity (small-e) and large-eccentricity (large-e) models according to the classification by Gladman (1993); in the circular model, the inner and outer orbits are both circular ($e = 0$), whereas in the low- and high-eccentricity models, the two orbital eccentricities satisfy $e < \mu^{1/3}$ and $e > \mu^{1/3}$, respectively.

The important parameters in the initial conditions are summarized for all the models in Table 3.1. We use the Kepler elements introduced in §1.1.1. In the SMBH group, I fix the inner semi-major axis $a_{\rm in}$ to 1.0 au, while in the IMBH group, $a_{\rm in}$ is determined so that the inner orbital period should be the same as that of the SMBH group to facilitate comparison. All the models have coplanar and prograde

group	model	$m_1[\mathrm{M}_\odot]$	$m_i[\mathrm{M}_\odot]$	$a_\mathrm{in}[\mathrm{au}]$	e	$\omega[\mathrm{deg}]$
SMBH	circular	10^6	1.0	1.0	0	-
SMBH	small-e	10^6	1.0	1.0	0.009	0
SMBH	large-e	10^6	1.0	1.0	0.1	0
IMBH	circular	10^3	1.0	0.1	0	-
IMBH	small-e	10^3	1.0	0.1	0.009	0
IMBH	large-e	10^3	1.0	0.1	0.2	0

Table 3.1: The important parameters in the initial conditions for all models treated in this research. The third and fourth columns, m_1 and m_i, are the masses of the central object and the orbiting objects in the three-body system. The subscript i runs from 2 to 3 and I set $m_2 = m_3$. The fifth column, a_in, is the semi-major axis of the inner orbit. The semi-major axis of the outer orbit, a_out, is determined from the parameter of the orbital separation Δ as explained in the text. The sixth column, e, is the eccentricity, which is assumed to be common to the inner and outer orbits. The last column, ω, is the argument of periastron of the two orbits, which are assumed to be the same. Note that in the circular orbit, we cannot define it. The information about the other orbital elements, e.g., the inclinations and the mean anomalies are given in the text.

orbits, that is, the relative inclination $I = 0$. The longitude of the ascending node Ω cannot be defined in such a condition. Note that the Newtonian Hill stability with finite relative inclinations is investigated in detail by Grishin et al. (2017). They showed that for highly inclined Hierarchical three-body systems, the ZLK mechanism operates and affects stability. It is known, on the other hand, that the 1PN effects change the features of the ZLK mechanism as discussed in Chapter 2. Although its effect on stability is also an interesting issue, it is beyond the scope of this research and will be addressed in the future.

As mentioned repeatedly, here I consider the relation between the onset time of the orbital instability and the initial orbital separation. The latter one is denoted as Δ, which is defined as the difference of the semi-major axes in the units of the mutual Hill radius R'_Hill:

$$a_\mathrm{out} - a_\mathrm{in} = \Delta R'_\mathrm{Hill}. \tag{3.78}$$

The mutual Hill radius R'_Hill is a distant scale almost the same as the Hill radius given in Eq. (3.29) but the mass and semi-major axis in the definition are replaced with the mean values of those of the two orbits, that is, it is defined as

$$R'_\mathrm{Hill} \equiv \left(\frac{\mu_2 + \mu_3}{3} \right)^{\frac{1}{3}} \frac{a_\mathrm{in} + a_\mathrm{out}}{2}, \tag{3.79}$$

where μ_i is the mass ratio that is the same as that used in §3.2.2. The mutual Hill radius was used as the typical distant scale for the Hill stability in e.g. Hénon and Petit (1986); Chambers et al. (1996).

For each model, I change the value of Δ from 1.0 by an increment of 0.1 and compute both the Newtonian and 1PN orbital evolutions. The initial mean anomalies of the two orbiting objects M_in and M_out are set randomly to satisfy that they should

be separated by at least 20°. For each value of Δ, I perform three computations with different combinations of mean anomalies.

The method of numerical simulations is almost the same as that explained in §2.3.1. First, the Kepler elements are transformed into the positions and velocities in the Cartesian coordinates of the constituent bodies. Then the Newtonian and 1PN (Eq. (1.159)) equations of motion are numerically integrated by using the sixth order implicit Runge-Kutta method (Butcher, 1964). As mentioned in §2.3.1, I directly integrate the equations of motions and successfully avoid the difficulty pointed out for the double-averaging method (see §1.2.2). Each computation is continued up to either the onset of instability or 10^6 yrs. When the integration is completed, the positions and velocities at each timestep again converted into the orbital elements of the osculating orbit.

In the numerical simulations, the onset of the instability is judged by the separation of two adjacent orbits, that is, we assume that the instability sets in when the difference of the distance of the periastron of the outer orbit and that of the apoastron of the inner orbit becomes smaller than one of the Hill radii of the two orbiting objects:

$$a_{\mathrm{out}}(1 - e_{\mathrm{out}}) - a_{\mathrm{in}}(1 + e_{\mathrm{in}}) < R_{\mathrm{Hill},i}, \qquad (3.80)$$

where $R_{\mathrm{Hill},i}$ is the Hill radius of the i-th object defined in Eq. (3.29). We remark that although some authors employed the mutual Hill radius as the critical distance instead of the Hill radius, both the radii are not much different from each other. Hence I do not think that the change of the criterion would produce qualitatively different results. As already mentioned, if Eq. (3.80) is satisfied in the simulation, I record the time as the onset time of instability T_{stab}. If, on the other hand, the system has a stable evolution up to 10^6 yrs in all the three calculations for the same Δ but different initial mean anomalies for the consecutive three values of Δ, I stop the calculation for that model assuming the system is Hill stable.

3.4   Results and Discussions

3.4.1   SMBH group

Here first I show the results of the numerical simulations of the models in the SMBH group. Second, I give the approximated sufficient conditions from the analyses by the mapping of the allowed and forbidden regions. Then I also discuss the higher-order PN effects with some timescales.

Orbital Evolutions and Relation between Δ and T_{stab}

In Fig. 3.4, I show an example of the 1PN evolutions of orbital elements of the small-e model in the SMBH group with $\Delta = 13.3$. The top and middle panels show the evolutions of the semi-major axes and eccentricities, respectively, and, in the bottom panel, the evolutions of the apoastron distance of the inner orbit and of the periastron distance of the outer orbit are presented. One can find that both the semi-major axes and the eccentricities are fluctuating around their initial values. The orbital evolution is calculated until the separation between the apoastron distance
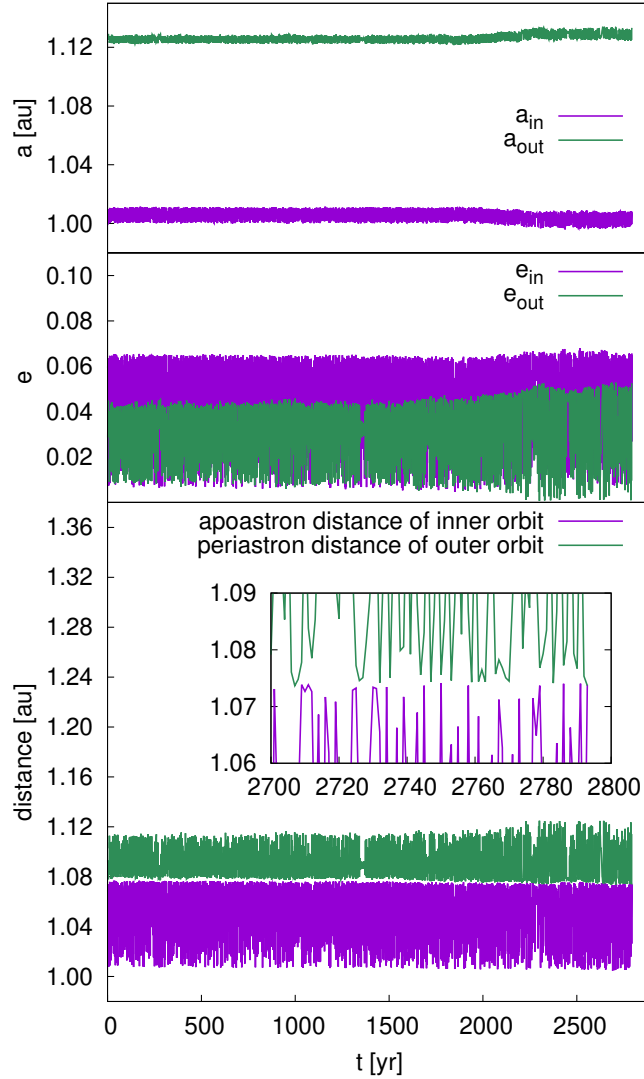
Figure 3.4: The 1PN evolutions of the orbital elements for the small-e model in the SMBH group with $\Delta = 13.3$. The purple and green lines correspond to the evolution lines of the inner and outer orbital elements, respectively. The top and middle panels show the evolutions of the semi-major axes and eccentricities. The bottom panel exhibits the time evolutions of the apoastron distance of the inner orbit and the periastron distance of the outer orbit. The inset is the enlargement around the onset time of the instability $T_{\mathrm{stab}} = 2793\,\mathrm{yrs}$.
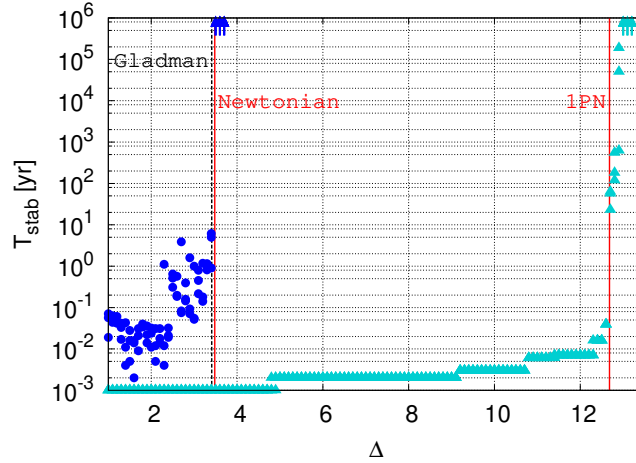
Figure 3.5:   The relation between Δ and T_{stab} for the circular model in the SMBH group. The blue dots and cyan triangles show the results of the Newtonian and 1PN calculations, respectively. Detailed explanations about the other vertical lines are in the text.

of the inner orbit and the periastron distance of the outer orbit satisfies the criterion of the Hill stability Eq. (3.80). In this case, the onset time of the instability T_{stab} is 2793 yrs.

The relations between Δ and T_{stab} for the circular, small-e, and large-e models in the SMBH group are summarized in Figs. 3.5 to 3.7, respectively. In these figures, the blue dots and the cyan triangles show the results of the Newtonian and 1PN calculations. The onset time of the instability T_{stab} is shorter for the 1PN calculations than for the Newtonian ones in these figures, which means that the 1PN evolutions are more unstable than the Newtonian ones in the sense of the Hill stability.

The 1PN effect should mainly appear as the orbital periastron shift as seen in §1.2.2, and this may be the cause of the earlier instability. The timescale of the periastron shift t_{P} can be estimated from the evolutionary equation of the argument of periastron ω with the simplest 1PN correction in Eq. (1.170) as

$$
\begin{aligned}
t_{\mathrm{P}} &= \frac{n_{\mathrm{in}} a_{\mathrm{in}}^2}{V^{(\mathrm{1PN})}} \approx \frac{1}{3\pi} \frac{a_{\mathrm{in}}}{r_{g,1}} P_{\mathrm{in}} \\
&\sim 2\mathrm{day} \left(\frac{a_{\mathrm{in}}}{1.0\mathrm{au}} \right) \left(\frac{r_{g,1}}{0.020\mathrm{au}} \right)^{-1} \left(\frac{P_{\mathrm{in}}}{0.365\mathrm{day}} \right), \qquad (3.81)
\end{aligned}
$$

where $r_{g,1} = 2Gm_1/c^2$ is the Schwarzschild radius of the central object, and P_{in} is the period of the inner orbit. This timescale is not much longer than the inner-orbital period and smaller than T_{stab} in the Newtonian calculations, e.g., for $\Delta < 4.0$ in Fig. 3.5, which suggests that the periastron shift should affect the 1PN Hill stability.

The onset time of the instability T_{stab} grows almost monotonically with respect to Δ in the circular and small-e models, but in the large-e model, its behavior looks more complicated. This may be because, for the highly eccentric orbits, the initial mean anomalies become another important factor of the stability. In order to confirm this, I plot another three 1PN calculations in Fig. 3.7 by fixing the initial
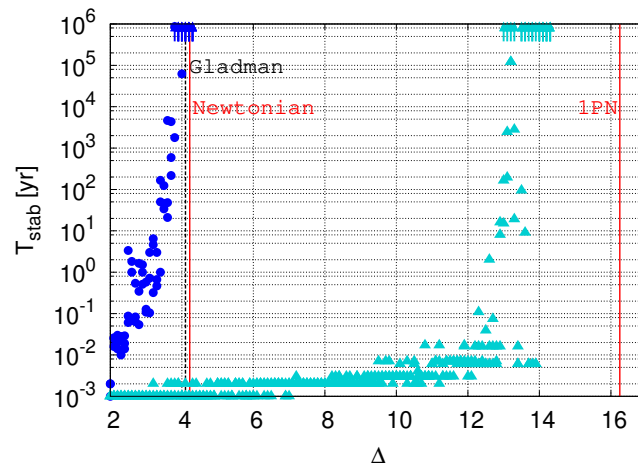
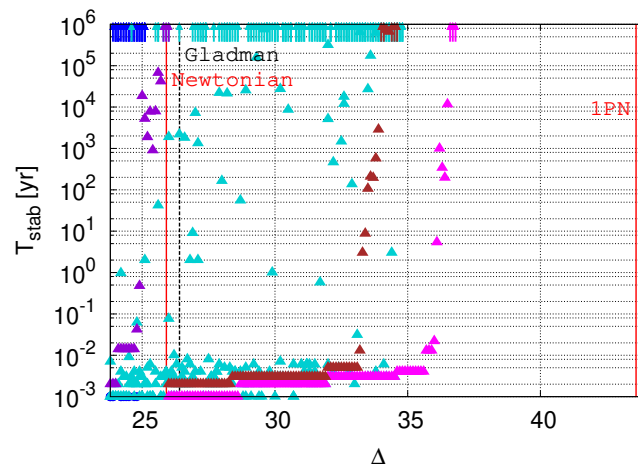Figure 3.6: The same as Fig. 3.5 but for the small-e model in the SMBH group.

Figure 3.7: The same as Figs. 3.5 and 3.6 but for the large-e model in the SMBH group. Three 1PN calculations with fixed initial mean anomalies are also shown as the triangles with different colors: magenta, brown and purple triangles show the results of the 1PN calculations with $(M_{\mathrm{in}}, M_{\mathrm{out}}) = (0°, 0°)$, $(0°, 180°)$, and $(180°, 90°)$, respectively.

mean anomalies to different values: magenta, brown and purple triangles exhibit the 1PN results for the initial mean anomalies $(M_{\text{in}}, M_{\text{out}}) = (0°, 0°)$, $(0°, 180°)$ and $(180°, 90°)$, respectively. One can find that T_{stab} grows almost monotonically with respect to Δ when the initial mean anomalies are fixed. The purple triangles corresponding to $(M_{\text{in}}, M_{\text{out}}) = (180°, 90°)$ show rapid increase of T_{stab} around $\Delta = 25.0$, whereas, for the magenta triangles corresponding to $(M_{\text{in}}, M_{\text{out}}) = (0°, 0°)$, it keeps small value until $\Delta = 35.0$. These two extreme results probably correspond to the most stable and unstable limits and encompass the results with other mean anomalies.

The black dashed lines in Figs. 3.5 to 3.7 show the sufficient conditions given by Gladman (1993) as Eqs. (3.49) to (3.51). In these figures, Gladman's sufficient conditions well explain the numerical results obtained from the Newtonian calculations. However, they are clearly inconsistent with those from the 1PN calculations, which means that it is inappropriate to apply Gladman's Newtonian sufficient conditions to such compact multi-body systems with an SMBH as considered here.

The red lines in these figures are the approximated sufficient conditions obtained in this chapter. In the next part, I explain the derivation of them. One finds that the 1PN approximated sufficient conditions for the Hill stability works much better than the Gladman's Newtonian conditions. The features of the approximated condition seen in each figure are also discussed in the next part.

Approximated Sufficient Condition

In order to analyze the numerical results further, I map the allowed and forbidden regions of motion for the third body by using Eq. (3.35) for the Newtonian and Eq. (3.67) for the 1PN cases, respectively. For the mapping of the allowed region of the third body, one needs to fix the positions of the central and inner-orbiting objects as explained in §3.3.1, so here I fix Δ and r_{12} in addition to the values of the total energy and angular momentum. Since r_{12} fluctuates with time as shown in the bottom panel of Fig. 3.4, I use r_{12} in a finite range.

In Fig. 3.8, the maps of the Newtonian allowed regions for the circular models with $\Delta = 2.0$, 3.0, and 3.6 are exhibited. The top left and right panels show the whole map for $\Delta = 2.0$ and the enlargement of the vicinity of the inner-orbiting object, and the bottom left and right panels are the enlarged maps for $\Delta = 3.0$ and $\Delta = 3.6$, respectively. The cross points in these panels indicate the positions of the central SMBH and the inner-orbiting object. In this figure, the value of r_{12} is fixed to $1.01a_{\text{in}}$. The color in the figure shows the value of the function f_{N} defined as

$$f_{\text{N}} = 2 \left(\sum_j m_j r_j^2 \right) (\mathcal{H}_{\text{N}} - U_{\text{N}}) - J_{\text{N}}^2. \tag{3.82}$$

In the bluish region of the figure, the value of f_{N} is positive, which means that inequality (3.35) is satisfied and the region corresponds to the allowed region for the third body. On the other hand, in the reddish region, f_{N} is negative, and the region corresponds to the forbidden region where the third body cannot enter. The green line is a contour corresponding to $f_{\text{N}} = 0$, which is the boundary between the allowed and forbidden regions.
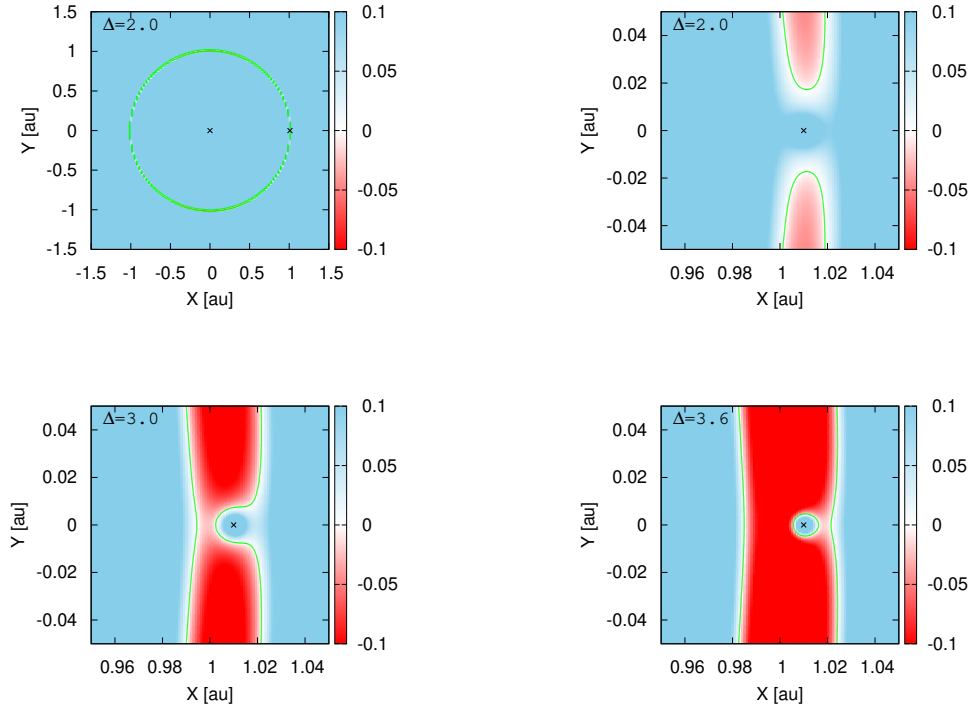
Figure 3.8: The Newtonian allowed and forbidden regions for the third body of the circular model in the SMBH group. The upper two panels show the results for $\Delta = 2.0$: the right panel is the enlargement of the inner-orbiting object. The enlargements for $\Delta = 3.0$ and 3.6 are displayed in the bottom left and right panels, respectively. The value of function f_N is represented by colors. The bluish and reddish regions correspond to the allowed and forbidden regions, respectively. The green lines are contours for $f_N = 0$, which corresponds to the boundary dividing the two regions. Cross points are the positions of the central SMBH and the inner-orbiting object. The distance between these two objects is fixed to $1.01a_{in}$.
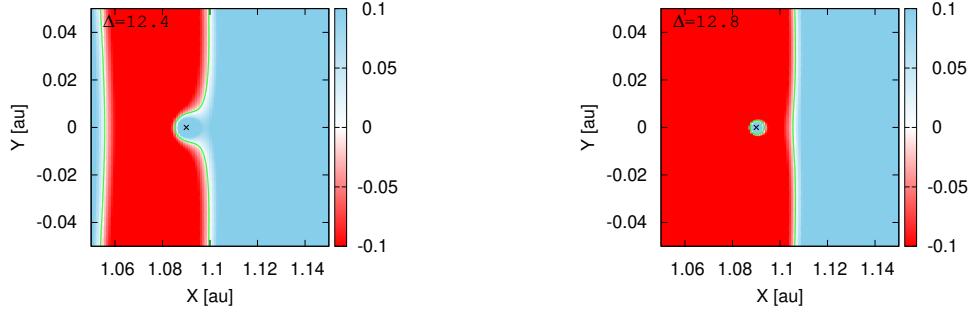
Figure 3.9:   The 1PN allowed and forbidden regions for the third body of the circular model in the SMBH group. The left and right panels show the enlargements of the inner-orbiting objects for $\Delta = 12.4$ and 12.8, respectively. The value of function f_{1PN} is represented by colors. The bluish and reddish regions show the allowed and forbidden regions, respectively. The green lines are contours for $f_{1PN} = 0$, which corresponds to the boundary dividing the two regions. The position of the inner-orbiting object in each panel is indicated as the cross point. The distance between the central and the inner-orbiting objects is fixed as $r_{12} = 1.09 a_{in}$.

For $\Delta = 2.0$, the inner orbit except around the cross point is covered with the forbidden region. As seen in the bottom panels, when Δ increases, the forbidden region is expanded. At $\Delta = 3.0$, the forbidden region is extended to the Lagrangian point L_1 between the central and inner-orbiting objects, and at $\Delta = 3.6$, the forbidden region reaches another Lagrangian point L_2 and the inner-orbiting object is now completely surrounded by the forbidden region. In the latter situation, the third body is not allowed to approach the inner-orbiting one as closely as the Hill radius, that is, the system is Hill stable. This behavior of the Newtonian allowed-region is consistent with what was explained in §3.2.2.

The allowed and forbidden regions described with the 1PN inequality (3.67) show similar behaviors as Newtonian ones. The enlarged maps for $\Delta = 12.4$ and 12.8 are exhibited in Fig. 3.9. The color in this figure shows the value of the function f_{1PN} defined as

$$f_{1PN} = 2 \left(\sum_j m_j r_j^2 \right) \left\{ \mathcal{H}_{1PN} - U_N + \frac{9}{8} \frac{G^2 m_1^2}{c^2} \left(\frac{m_2}{r_2^2} + \frac{m_3}{r_3^2} \right) \right\} - J_{1PN}^2. \quad (3.83)$$

As in the Newtonian maps in Fig. 3.8, the bluish and reddish regions are the allowed and forbidden regions for the third body, respectively. The green line corresponds to the boundary between them. In the left panel of Fig. 3.9, one finds that the forbidden region is extended to the inner Lagrangian point L_1 at $\Delta = 12.4$. On the other hand, in the right panel, one can see that the forbidden region is further expanded to the outer Lagrangian point L_2 and surrounds the inner-orbiting object completely at $\Delta = 12.8$. From these results, it can be considered that, in this configuration, the arrival of the forbidden region at L_2 may be regarded as the sufficient condition of the Hill stability both in the Newtonian and 1PN calculations.

The local minimum of f_{1PN} is close but not exactly the same as that of f_N. In

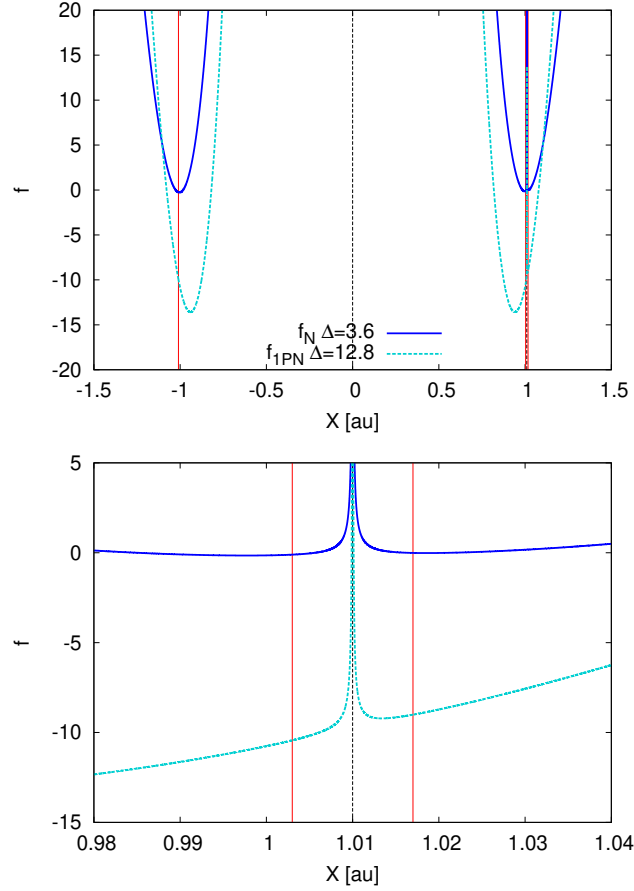Figure 3.10: The values of f_{N} (blue solid line) and f_{1PN} (cyan dashed line) as functions of X with $Y = 0$. The bottom panel is the enlargement of the inner-orbiting object. The values of Δ are set as $\Delta = 3.6$ and 12.8 for the Newtonian and 1PN calculations, respectively. The black lines show the positions of the central and inner-orbiting objects. The distance between them is fixed as $r_{12} = 1.01a_{\mathrm{in}}$ in both the Newtonian and 1PN calculations. The red solid lines exhibit the Newtonian Lagrangian points.

Fig. 3.10, I show the values of f_{N} and f_{1PN} on the X-axis with $Y = 0$. The value of Δ is set as 3.6 and 12.8 in the Newtonian and 1PN calculations, respectively. The top and bottom panels show the whole view and the enlargement of the inner-orbiting object. The blue and cyan lines exhibit the values of f_{N} and f_{1PN}, respectively. The black dashed lines correspond to the positions of the central and inner-orbiting objects. The distance between the central and inner-orbiting objects r_{12} is fixed to $1.01a_{\mathrm{in}}$ in both the Newtonian and 1PN calculations. The red solid lines exhibit the Newtonian Lagrange points L_1, L_2, and L_3, whose X-coordinates are obtained by replacing a in Eqs. (3.26) to (3.28) with r_{12}. As in Fig. 3.10, the local minimum points of f_N coincide with the Newtonian Lagrange points, but those of f_{1PN} are slightly dislocated from the points. The local minimum points of f_{1PN} are hence should be called the 1PN Lagrangian points.

From the above analyses with the mapping of the allowed and forbidden regions, I find the approximated sufficient condition of the Hill stability could be obtained

in the following steps: fixing r_{12}, I first search for the value of $\Delta = \Delta_{\mathrm{cr}}$ at which the forbidden region appears for the first time, in the range of $R_{\mathrm{Hill},2}$ to $50R_{\mathrm{Hill},2}$ from the inner-orbiting object; second, the value of r_{12} is varied in the range of $0.5a_{\mathrm{in}}(e_{\mathrm{in}} - 1)$ to $1.5a_{\mathrm{in}}(e_{\mathrm{in}} + 1)$, looking for the maximum value of Δ_{cr} at which the forbidden region surrounds the inner-orbiting object. The maximum value of Δ_{cr} obtained in this way is regarded as the approximated sufficient condition of the Hill stability. The Newtonian and 1PN sufficient conditions derived by the above way are exhibited in Figs. 3.5 to 3.7 as the red solid lines.

In these figures, one finds that the Newtonian red lines agree well with Gladman's sufficient conditions although the criterion is a bit tighter for the large-e case. They are also consistent with the numerical results as a sufficient condition for the Hill stability. The discrepancies from Gladman's conditions may be caused by the numerical procedure to search maximum Δ_{cr}, in which the values of r_{12} and Δ are changed independently within a finite range.

The 1PN red lines that are newly obtained here, on the other hand, are also consistent with the results of the 1PN simulations. As sufficient conditions for the 1PN Hill stability, it is a little too tight for the circular model as seen in Fig. 3.5 whereas they are looser for small- and large-e models compared with the Newtonian calculations. Some of the approximations imposed in §3.3.1 may be the cause of these discrepancies: actually, the virial approximation in Eq. (3.65) is not strictly satisfied and may have caused the small discrepancy seen in Fig. 3.5, and, on the other hand, in the small- and large-e models in Figs 3.6 and 3.7, the approximations used in Eqs. (3.71) and (3.76) may be too conservative and be the reason for the looseness of the 1PN approximated sufficient conditions.

Effect of Higher-Order PN Terms

So far, the higher-order PN terms are completely neglected in this chapter. Here their importance for the Hill stability of the models in the SMBH group is roughly estimated.

The 1.5PN terms cause the spin-orbit coupling called the Lense-Thrring precession. Its timescale is given as Eq. (2.67) and with the parameters of the models in the SMBH group, it is estimated as

$$t_{\mathrm{LT}} = \frac{2c^3 a_{\mathrm{in}}^3 (1 - e_{\mathrm{in}}^2)^{3/2}}{\chi_1 G^2 m_1^2 (4 + 3m_2/m_1)} \sim 1\mathrm{yr} \left(\frac{\chi_1}{0.1}\right)^{-1} \left(\frac{a_{\mathrm{in}}}{1.0\mathrm{au}}\right)^3 \left(\frac{m_1}{10^6 \mathrm{M}_\odot}\right)^{-2}, \qquad (3.84)$$

where $\chi_1 \leq 1$ is the Kerr parameter. This timescale is not much longer than the orbital periods and hence may have an important effect on the relativistic Hill stability even if the Kerr parameter of the central SMBH is not so large. Its detailed analysis will be given in future work.

The 2.5PN term corresponds to the GW emission. The timescale of the GW emissions in a binary system is estimated in Peters (1964) and calculated with the

parameters of the models with an SMBH as

$$
\begin{aligned}
t_{\mathrm{GW}} &= \frac{5}{256}\frac{c^5}{G^3}\frac{a_{\mathrm{in}}}{m_1 m_2 (m_1 + m_2)} \\
&\sim 10^5 \mathrm{yr} \left(\frac{a_{\mathrm{in}}}{1.0\mathrm{au}}\right)^4 \left(\frac{m_1}{10^6 \mathrm{M_\odot}}\right)^{-2} \left(\frac{m_2}{1.0\mathrm{M_\odot}}\right)^{-1}.
\end{aligned}
\tag{3.85}
$$

This is essentially the time that it takes to cause the merger of the inner-orbiting object with the central SMBH, that is, if T_{stab} is longer than t_{GW}, the inner orbit collapses before the system become unstable in the sense of the Hill stability. In such a case, the so-called Extreme Mass Ratio Inspiral (EMRI) with an outer perturber might be observed through the GW observations (Amaro-Seoane et al., 2012; Yang and Casals, 2017; Bonga et al., 2019). Although it is also interesting to investigate how the GW emission affects the sufficient conditions themselves, it will be addressed in the future.

These interesting effects are unaddressed, though, I think that the 1PN approximated sufficient conditions for the relativistic Hill stability should be a useful tool. It can be used, for example, to estimate the stability of multi-body systems before conducting costly direct numerical simulations.

3.4.2 IMBH group

For models in the IMBH group, the relations between Δ and T_{stab} obtained from the 1PN numerical simulations are not so different from those obtained from the Newtonian calculations. Both of the Newtonian and 1PN results for models in the IMBH group show actually the same behavior as the Newtonian results for the models in the SMBH group. The results of the circular, small-e, and large-e models are exhibited in Figs. 3.11 to 3.13, respectively.
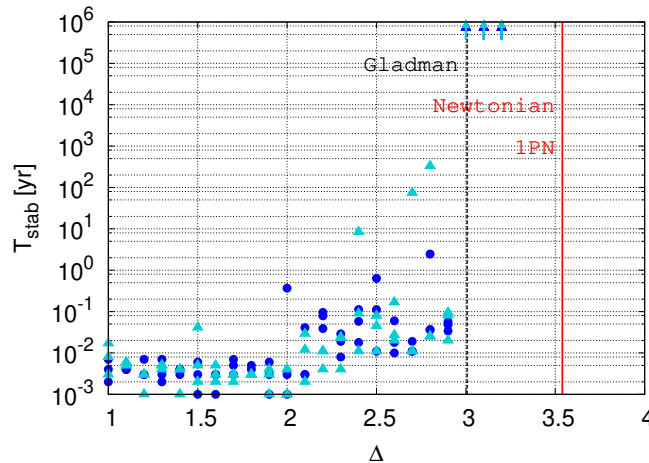

Figure 3.11: The same as Fig. 3.5 but for the circular model in the IMBH group.

The long-term numerical simulations done in this chapter show the typical error less than $1\,\%$ in the conservation of total angular momentum. For a small number of models in the IMBH group, however, I found much larger numerical errors more
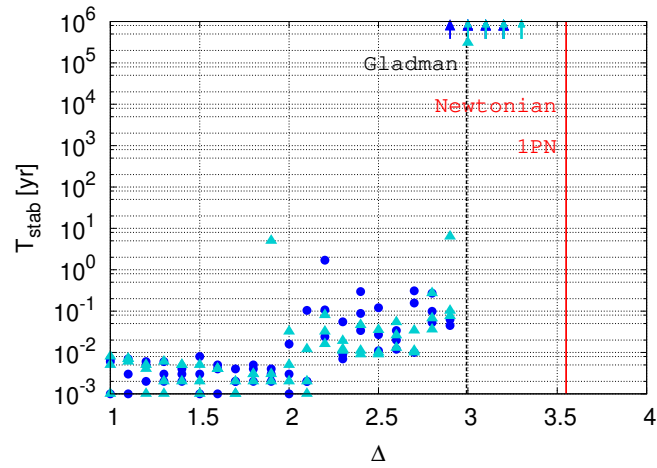
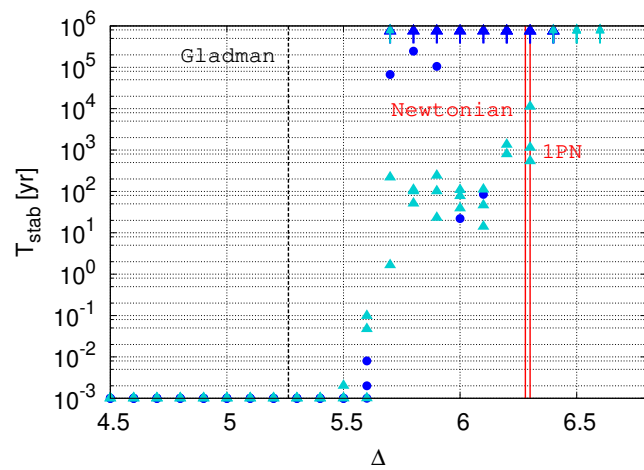Figure 3.12:   The same as Fig. 3.5 but for the small-*e* model in the IMBH group.

Figure 3.13:   The same as Fig. 3.5 but for the large-*e* model in the IMBH group.

than a few tens %, which is caused when the eccentricities are highly excited in their orbital evolutions. In such situations, I should have employed a much shorter timestep to resolve fast motions around the periastron, which I could not afford due to the computational cost, though. Hence, those apparently failed computations with the relative error of more than 5 % are just excluded from the analysis.

The Newtonian and 1PN approximated sufficient conditions shown as the red lines in the figures are completely overlapped. This can be explained with the inequality (3.67), that is, the left-hand side of inequality (3.67) is negligibly small in models in the IMBH group and inequalities (3.35) and (3.67) become almost identical. The timescale of the periastron shift is $t_P \sim 2.0 \times 10^3$ days. This value is much longer than the inner-orbital period and somewhat longer than T_{stab} in the Newtonian case, which implies again that the 1PN effects do not affect the Hill stability very much in the models in the IMBH group.

Hence, the 1PN effect on the Hill stability is important only when the last term in the left-hand side of Eq. (3.67) becomes comparable with the total Hamiltonian or the Newtonian potential. Here I find that this is not the case for the systems with the 10^3 M$_\odot$ IMBH and the inner-orbital semi-major axis $a_{in} = 0.1$ au. The difference between Gladman's sufficient conditions and the Newtonian approximated sufficient conditions seen in Figs. 3.11 and 3.12 may be caused by the numerical procedure to derive the latter conditions as I discussed in §3.4.1. Interestingly, Gladman's condition fails to reproduce the results of the Newtonian simulation in Fig. 3.13. This may be because the expansion with μ and e used to derive Eq. (3.50) in §3.2.2 no longer appropriate in this model.

Finally, I give the estimations of the neglected higher-order PN effects as done in §3.4.1. The timescale of the Lense-Thrring precession t_{LT} corresponding to the 1.5PN order is evaluated with the parameters of the models with an IMBH as

$$t_{LT} \sim 10^3 \text{yr} \left(\frac{\chi_1}{0.1}\right)^{-1} \left(\frac{a_{in}}{0.1\text{au}}\right)^3 \left(\frac{m_1}{10^3 \text{M}_\odot}\right)^{-2}. \tag{3.86}$$

This is not so long compared with the typical value of T_{stab} in Figs. 3.11 to 3.13 and the 1.5PN terms may affect the relativistic Hill stability for the models in the IMBH group, especially when the IMBH has a relatively large spin parameter. On the other hand, the effect of the GW emission at the 2.5PN order is estimated as

$$t_{GW} \sim 10^7 \text{yr} \left(\frac{a_{in}}{0.1\text{au}}\right)^4 \left(\frac{m_1}{10^3 \text{M}_\odot}\right)^{-2} \left(\frac{m_2}{1.0\text{M}_\odot}\right)^{-1}. \tag{3.87}$$

This timescale is much longer than the computational time in this chapter and the GW effect may not be seen in similar simulations. If the orbital evolutions are calculated for a much longer time, the inner orbit may merge before the system becomes unstable in the sense of Hill stability, as discussed in §3.4.1.

3.5 Summary

I studied the relativistic effects on the stability problem of the multi-body systems focusing on the Hill stability problem. The Hill stability is defined as the stability

of multi-body systems against close approaches of their orbits. In this chapter, I extended the Newtonian formalism to obtain the sufficient condition to the relativistic one using the 1PN approximation and limiting the configuration to the three-body systems that have an SMBH or an IMBH as a central object and two objects with much smaller masses orbiting around the central object. I successfully obtained the approximated sufficient condition for the 1PN Hill stability of the three-body systems with the above configurations and confirmed its validity with numerical simulations.

In Newtonian mechanics, the sufficient condition for the Hill stability of three-body systems was obtained from the analysis with Sundman's inequality. With the conserved quantities of the system, the inequality gives the allowed region for the motion of the components of the system. If a forbidden region lies between the two orbiting objects, the system should be stable in the sense of the Hill stability. In the previous study by Marchal and Bozis, the Newtonian sufficient condition for general three-body systems was obtained with a technical parameterization of Sundman's inequality.

In order to derive the relativistic sufficient condition of the Hill stability, first I derived the inequality for the allowed region by substituting the 1PN Hamiltonian and total angular momentum into Sundman's inequality. For simplicity, I imposed several approximations assuming a limited configuration that a central object is much heavier than those of orbiting objects, and also employed the virial approximation to rewrite the velocity with the function of the positions. I found that, as in the Newtonian case, when a forbidden region lies between the two orbiting objects, the system is judged as stable in the sense of the Hill stability. Instead of the technical approach done in Newtonian analysis, I used numerical analysis to obtain the 1PN sufficient condition from the inequality for the allowed regions, that is, I estimated the inequality by changing orbital separation Δ and the distance between two objects r_{12} independently within finite ranges, and found the maximum value of Δ as the approximated sufficient condition of the Hill stability.

I confirmed this newly obtained 1PN approximated sufficient condition with numerical simulations. In the numerical analysis, the 1PN equations of motion were directly integrated with the sixth-order implicit Runge-Kutta method. Following the Newtonian previous studies, I computed numerous three-body systems with different initial orbital separation Δ and investigated the relation between Δ and the onset time of the orbital instability T_{stab}. The systems computed in this research were divided into two groups: one with an SMBH as the central object and the other containing an IMBH. Each group consisted of three models: circular, small-e, and large-e models. The relation between Δ and T_{stab} was investigated for each model in each group, and the result was compared with the 1PN approximated sufficient condition derived in this research.

In the SMBH group, the 1PN effects are important for stability. Actually, the 1PN orbital evolutions are more unstable than the Newtonian ones in all the models in the SMBH group. The numerical results are consistent with the new criterion as a sufficient condition for the 1PN Hill stability, especially for the circular and small-e models. Although it is also valid as a sufficient condition in the large-e model, the criterion is not so strict compared with the numerical results. This is probably

because the approximation adopted for the position r is somewhat too conservative. In the IMBH group, the results obtained in the 1PN calculations are not so different from those obtained in the Newtonian calculations. These results imply that the 1PN effect is negligible for the Hill stability of the three-body systems in the IMBH group. Incidentally, I found that the Newtonian sufficient condition obtained by Gladman is inconsistent with the numerical results for the large-e model whereas the Newtonian criterion obtained in this chapter is still valid in these cases.

I did not include the higher-order PN terms for simplicity but estimated the several important effects: the Lense-Thirring precession (1.5PN) and GW emissions (2.5PN). The timescales on which these effects become appreciable are not so long compared with the orbital periods of the systems. This indicates that these processes cannot be ignored to obtain a tighter condition. These higher-order PN effects will be an interesting topic worth further investigation. Although these important issues still remain, I think the 1PN approximated sufficient conditions given in this chapter will be useful as a measure for the orbital stability of relativistic multi-body systems, and one can use them before conducting costly numerical simulations for such systems.

Chapter 4

Conclusion

Stellar dynamics is one of the oldest research topics that has been discussed mainly in Newtonian mechanics. It started to be discussed with general relativity recently, but many interesting topics have not been discussed yet in the general relativistic regime. In this thesis, I intended to study these remaining topics and to contribute to the comprehension of the dynamics of relativistic multi-body systems. I used post-Newtonian (PN) approximation to consider relativistic effects as some correction terms to the Newtonian equations of motion. The first-order PN (1PN) approximation was mainly used in this thesis, and the higher-order PN effects were briefly discussed in each chapter. Since some authors pointed out several accuracy problems of the so-called double-averaging method, which has been commonly used to calculate dynamics of relativistic multi-body systems, I directly integrated the 1PN equations of motion in the numerical simulations to avoid the difficulty of the double-averaging method.

First, I discussed the 1PN effect on the von Zeipel-Lidov-Kozai (ZLK) mechanism and its application to the observation of the effect of the emission of gravitational waves (GW) through the cumulative shift of periastron time (CSPT) of a binary pulsar in a hierarchical triple system. The ZLK mechanism is one of the orbital resonances seen in the hierarchical triple systems and characterized by the periodic oscillation of the inner-orbital eccentricity and the relative inclination between the inner and outer orbits. Its Newtonian features have been deeply understood with the double-averaging method. The 1PN correction on the method has also given a simple estimation of the relativistic effects on the ZLK mechanism. However, by comparing the numerical results obtained from the direct integration of the equations of motion with those from the double-averaging estimation, I found several discrepancies that should not be neglected when the GW emission is considered. I stressed that it is important to calculate the relativistic ZLK mechanism by the direct integration especially when the maximum eccentricity becomes quite large.

The excitation of the eccentricity by the ZLK mechanism enhances the GW emission from the binary. If it occurs in a hierarchical triple system with a binary pulsar, the enhanced GW emission changes the shape of the CSPT curve, which may be seen in the radio observation of a pulsar. I proposed a method to calculate the CSPT for a general hierarchical three-body system with a binary pulsar and calculated it for several three-body models. The models consist of compact objects

whose parameters are in the ranges where the change of the CSPT curve due to the ZLK mechanism could be observed within our lifetime (< 100 yr). When the ZLK mechanism occurs in the models, the bending of the CSPT curve is seen. Its slope and the time between two bending points in the curve indicate the value of the eccentricity and the ZLK timescale. Although the systems that cause such an interesting signal might be rare, searching such signals is very important because it will be the first indirect observation of the GW from triple systems. In regard to the higher-order PN effects, the 1.5PN terms may affect the systems as the precession of the beaming angle of the pulsar and it may result in the disappearance of the pulsar from the observable range, which will provide one of the important examples of the 1.5PN effect on the ZLK oscillation.

Second, I studied the relativistic effects on the stability problems focusing on the Hill stability problem, which is defined as the stability of multi-body systems against the close approach of their orbits. I discussed the relativistic Hill stability problem for three-body systems with limited configurations that have an SMBH or IMBH as their central object and obtained an approximated sufficient condition with the 1PN approximation. I derived the inequality for the allowed region by substituting the 1PN conserved quantities into Sundman's inequality imposing several approximations: I assumed that a central object is much heavier than orbiting objects, and also employed the virial approximation to rewrite the velocity with the function of the positions. By mapping the allowed region, I found that the system is Hill stable when a forbidden region appears between the two orbiting objects. Although the sufficient condition was obtained in the Newtonian case by the technical parameterization of the inequality for the allowed region, in the 1PN case, I used the numerical analysis to obtain the 1PN approximated sufficient condition. I estimated the inequality by changing orbital separation Δ and the distance between the central and inner-orbiting objects r_{12} independently within finite ranges and found the maximum value of Δ with which a forbidden region appears between the two orbiting objects. I interpreted the maximum Δ as the approximated sufficient condition of the Hill stability.

This newly obtained 1PN approximated sufficient condition was confirmed by the comparison with the results of the numerical simulations. Numerous three-body systems with different initial orbital separation Δ were calculated to investigate the relation between Δ and the onset time of the orbital instability T_{stab}. For the system with an SMBH as its central object, the 1PN calculation showed much more unstable evolutions than those in the Newtonian calculation. The results are consistent with the 1PN approximated sufficient condition especially when the orbits in the model initially have zero or small eccentricities. When the system has initially highly eccentric orbits, the criterion is not so strict compared with the numerical results, although it is still valid as a sufficient condition, probably because of the approximation adopted to obtain the inequality for the allowed region. For the systems with an IMBH, the 1PN and Newtonian simulations showed not-so-different results, which implies that the 1PN effect is negligible for the Hill stability in such systems. The higher-order PN effects that were neglected in this research, like 1.5PN and 2.5PN effects, may also have important effects on the Hill stability. Although these higher-order PN terms remain to be included, I consider the 1PN

approximated sufficient conditions will be useful as a measure for the orbital stability of the relativistic multi-body systems and one can employ them before conducting costly numerical simulations.

Appendix A

Delaunay variables

From the Liouville-Arnold theorem, an integrable Hamiltonian system could be described with the canonical variables called action-angle variables (Arnold, 1989). The momenta of the variables are called *actions*. They correspond to the first integrals of the system, that is, they do not evolve with time. The corresponding coordinates are called *angles*, which are cyclically defined with period 2π. With these variables, the Hamiltonian of the system becomes the function only of the actions. These variables are mainly used to analyze the resonances with the Hamiltonian mechanical approach.

The action-angle variables for the Keplerian motion are well known as *Delaunay variables*. They are described with the orbital elements as

$$L = \sqrt{\mathcal{G}(m_1 + m_2)a}, \quad l = M \tag{A.1}$$

$$G = L\sqrt{1 - e^2}, \qquad g = \omega \tag{A.2}$$

$$H = G\cos i, \qquad h = \Omega. \tag{A.3}$$

The variables denoted with capital letters L, G, and H are actions, whereas small characters l, g, and h describe corresponding angles. Here the gravitational constant is denoted as $\mathcal{G}$. In some researches about the stellar dynamics, these variables are used instead of the Kepler elements (e.g. Ford et al. (2000); Naoz et al. (2013a); Iwasa and Seto (2017)). The detailed derivation of these variables is explained in e.g. Morbidelli (2011).

Each action corresponds to the conserved quantities of the system: the action L is related with the orbital specific energy E defined in Eq. (1.1) as

$$L = \frac{\mathcal{G}(m_1 + m_2)}{\sqrt{-2E}}, \tag{A.4}$$

and G and H are the magnitude and Z-component of the specific angular momentum, respectively, that is,

$$G = \mathcal{J} = |\boldsymbol{\mathcal{J}}|, \tag{A.5}$$

$$H = \mathcal{J}_z, \tag{A.6}$$

where $\boldsymbol{\mathcal{J}}$ is the same as $\boldsymbol{h}$ defined in Eq. (1.2). On the other hand, three angles l, g, and h correspond to the angles in Kepler elements, the inclination i, the argument of periastron ω, and the longitude of the ascending node Ω, respectively.

Appendix B

Proof of Sundman's inequality

Sundman's inequality (3.30) can be proved by using the well-known Cauchy's inequality, which is given as

$$\left| \sum_j (A_j B_j) \right|^2 \leq \left| \sum_j (A_j)^2 \right| \left| \sum_j (B_j)^2 \right|, \tag{B.1}$$

where A_j and B_j are the components of arbitrary vectors $\boldsymbol{A}$ and $\boldsymbol{B}$. The components on the right-hand side of Eq. (3.30) are estimated as

$$\left| \sum_j m_j \boldsymbol{r}_j \times \boldsymbol{v}_j \right| \leq \sum_j m_j r_j v_j \left| \sin \gamma_j \right| = \sum_j \sqrt{m_j r_j^2} \sqrt{m_j v_j^2 \sin^2 \gamma_j}, \tag{B.2}$$

$$\left| \sum_j m_j \boldsymbol{r}_j \cdot \boldsymbol{v}_j \right| \leq \sum_j m_j r_j v_j \left| \cos \gamma_j \right| = \sum_j \sqrt{m_j r_j^2} \sqrt{m_j v_j^2 \cos^2 \gamma_j}, \tag{B.3}$$

where γ_j is the angle between $\boldsymbol{r}_j$ and $\boldsymbol{v}_j$. Applying Cauchy's inequality to the square value of Eq.(B.2) and (B.3) gives

$$\left| \sum_j m_j \boldsymbol{r}_j \times \boldsymbol{v}_j \right|^2 \leq \left| \sum_j \sqrt{m_j r_j^2} \sqrt{m_j v_j^2 \sin^2 \gamma_j} \right|^2$$

$$\leq \left(\sum_j m_j r_j^2 \right) \left(\sum_j m_j v_j^2 \sin^2 \gamma_j \right), \tag{B.4}$$

$$\left| \sum_j m_j \boldsymbol{r}_j \cdot \boldsymbol{v}_j \right|^2 \leq \left| \sum_j \sqrt{m_j r_j^2} \sqrt{m_j v_j^2 \cos^2 \gamma_j} \right|^2$$

$$\leq \left(\sum_j m_j r_j^2 \right) \left(\sum_j m_j v_j^2 \cos^2 \gamma_j \right). \tag{B.5}$$

Sundman's inequality (3.30) is immediately obtained if the summation of both two inequalities is taken.

Acknowledgments

First of all, I would like to express my sincere gratitude to Prof. Shoichi Yamada. As my supervisor and collaborator, he gave me a lot of advice not only on physics but also on the attitude toward research. He was always positive and I was inspired by him. The daily discussion with him was one of the most meaningful experiences in my life as a Ph.D. student. My research was not always going well and was delayed many times, but thanks to his encouragement I was able to continue my research.

I would also like to show my appreciation to Prof. Kei-ichi Maeda. I am convinced that it was a turning point for me that he invited me to study gravitational waves in my first year of the doctoral course. I was very fortunate to be able to study with him just before his retirement. I learned from him the way of thinking as a theoretical physicist.

I would also like to thank my collaborators, Dr. Hirotada Okawa and Ms. Priti Gupta. We had a weekly meeting with Prof. Maeda about gravitational waves and had a lot of meaningful discussions. I am proud to have been able to research with this team. I want to thank Dr. Yusuke Nakamura, another collaborator. The code created by him was the basis for my research.

I greatly appreciate all the members of Yamada Lab and Maeda Lab. Daily discussions and conversations with them have always inspired and encouraged me to continue my research.

Finally, I thank all my family and friends for supporting and encouraging me in my daily life.

Bibliography

Amaro-Seoane, P., Brem, P., Cuadra, J., and Armitage, P. J.: 2012, *Astrophys. J. Lett.* **744**, L20

Amaro-Seoane, P. et al.: 2017, *Laser Interferometer Space Antenna*, arXiv e-prints (arXiv:1702.00786)

Anderson, K. R., Lai, D., and Storch, N. I.: 2017, *Mon. Not. R. Astron. Soc.* **467**, 3066

Anderson, K. R., Storch, N. I., and Lai, D.: 2016

Antognini, J. M., Shappee, B. J., Thompson, T. A., and Amaro-Seoane, P.: 2014, *Mon. Not. R. Astron. Soc.* **439**, 1079

Antognini, J. M. O.: 2015, *Mon. Not. R. Astron. Soc.* **452**, 3610

Antonini, F., Chatterjee, S., Rodriguez, C. L., Morscher, M., Pattabiraman, B., Kalogera, V., and Rasio, F. A.: 2016, *Astrophys. J.* **816**, 65

Antonini, F. and Perets, H. B.: 2012, *Astrophys. J.* **757(1)**, 27

Antonini, F., Toonen, S., and Hamers, A. S.: 2017, *Astrophys. J.* **841**, 77

Antonini1, F., Hamers, A. S., and Lithwick, Y.: 2016, *Astron. J.* **152**, 174

Arnold, V.: 1989, *Mathematical methods of classical mechanics*, Vol. 60, Springer

Barker, B. M. and O'Connell, R. F.: 1975, *Phys. Rev. D* **12**, 329

Blaes, O., Lee, M. H., and Socrates, A.: 2002, *Astrophys. J.* **578**, 775

Bonga, B., Yang, H., and Hughes, S. A.: 2019, *Phys. Rev. Lett.* **123**, 101103

Butcher, J. C.: 1964, *math. Comp.* **18**, 50

Chambers, J. E. and Wetherill, G. W.: 1998, *Icarus* **136**, 304

Chambers, J. E., Wetherill, G. W., and Boss, A.: 1996, *Icarus* **119**, 261

Chandrasekhar, S. and Contopoulos, G.: 1963, *Proc. Natl. Acad. Sci. U. S. A.* **49(5)**, 608

Chatterjee, S., Ford, E. B., Matshumura, S., and Rasio, F. A.: 2008, *Astrophys. J.* **686**, 580

Chen, X., Madau, P., Sesana, A., and Liu, F. K.: 2009, *Astrophys. J. Lett.* **697**, L149

Chen, X., Sesana, A., Madau, P., and Liu, F. K.: 2011, *Astrophys. J.* **729**, 13

Chenciner, A. and Montgomery, R.: 2000, *Ann. of Math.* **152**, 881

Deck, K. M., Payne, M., and Holman, M. J.: 2013, *Astrophys. J.* **774**, 129

Deme, B., Hoang, B.-M., Naoz, S., and Kocsis, B.: 2020, *Astrophys. J.* **901**, 125

Eggleton, P. and Kiseleva, L.: 1995, *Astrophys. J.* **455**, 640

Einstein, A., Infeld, L., and Hoffmann, B.: 1938, *Annals of Mathematics. Second series.* **39(1)**, 65

Fang, Y., Chen, X., and Huang, Q.-G.: 2019, *Astrophys. J.* **887(2)**, 210

Fang, Y. and Huang, Q.-G.: 2019, *Phys. Rev. D* **99**, 103005

Ford, E. B., Kozinsky, B., and Rasio, F. A.: 2000, *Astrophys. J.* **535**, 385

Fragione, G. and Antonini, F.: 2019, *Mon. Not. R. Astron. Soc.* **488**, 728

Fragione, G. and Bromberg, O.: 2019, *Mon. Not. R. Astron. Soc.* **488**, 4370

Fragione, G. and Leigh, N.: 2018, *Monthly Notices of the Royal Astronomical Society* **479(3)**, 3181

Fragione, G. and Loeb, A.: 2019, *Monthly Notices of the Royal Astronomical Society* **486(3)**, 4443

Frewen, S. F. N. and Hansen, B. M. S.: 2015, *Monthly Notices of the Royal Astronomical Society* **455(2)**, 1538

Fujisawa, K., Okawa, H., Yamamoto, Y., and Yamada, S.: 2019, *Astrophys. J.* **872(2)**, 155

Ge, Y. C. and Alexander, D.: 1991, *Gen. Relativ. Gravit.* **23**, 335

Ge, Y. C. and Leng, X.: 1994, *Planet. Space. Sci.* **42**, 231

Gladman, B.: 1993, *Icarus* **106**, 247

Gopakumar, A., Bagchi, M., and Ray, A.: 2009, *Mon. Not. R. Astron. Soc.* **399**, L123

Grishin, E., Perets, H. B., and Fragione, G.: 2018, *Monthly Notices of the Royal Astronomical Society* **481(4)**, 4907

Grishin, E., Perets, H. B., Zenati, Y., and Michaely, E.: 2017, *Mon. Not. R. Astron. Soc.* **466**, 276

Gupta, P., Suzuki, H., Okawa, H., and Maeda, K.: 2020, *Phys. Rev. D* **101**, 104053

Hamers, A. S.: 2021, *Mon. Not. R. Astron. Soc.* **500**, 3481

Hamers, A. S. and Lai, D.: 2017, *Monthly Notices of the Royal Astronomical Society* **470(2)**, 1657

Hamers, A. S. and Safarzadeh, M.: 2020, *Astrophys. J.* **898**, 99

Harry, G. M., Fritschel, P., Shaddock, D. A., Folkner, W., and Phinney, E. S.: 2006, *Classical and Quantum Gravity* **23(15)**, 4887

Hénon, M.: 1970, *Astron. Astrophys.* **9**, 24

Hénon, M. and Petit, J. M.: 1986, *Celestial Mech.* **38**, 67

Hill, G. W.: 1878, *Amer. J. Math.* **1**, 129

Hoang, B.-M., Naoz, S., Kocsis, B., Rasio, F. A., and Dosopoulou, F.: 2018, *Astrophys. J.* **856**, 140

Hoang, B.-M., Naoz, S., Kocsis, B., Will, M. F., and Mclver, J.: 2019, *Astrophys. J. Lett.* **875**, L31

Hulse, R. A.: 1994, *Rev. Mod. Phys.* **66**, 699

Hulse, R. A. and Taylor, J. H.: 1975, *Astrophys. J.* **195**, L51

Ichita, T., Yamada, K., and Asada, H.: 2011, *Phys. Rev. D* **83**, 084026

Imai, T., Chiba, T., and Asada, H.: 2007, *Phys. Rev. Lett.* **98**, 201102

Ito, T. and Ohtsuka, K.: 2019, *Monographs on Environment, Earth and Planets* **7**, 1

Ito, T. and Tanikawa, K.: 1999, *Icarus* **139**, 336

Ivanov, P. B., Polnarev, A. G., and Saha, P.: 2005, *Mon. Not. R. Astron. Soc.* **358**, 136

Iwasa, M. and Seto, N.: 2017, *Monthly Notices of the Royal Astronomical Society* **472(2)**, 1600

Iwasaki, K. and Ohtsuki, K.: 2006, *Astron. J.* **131**, 3093

J, J. N. B. and Wegg, C.: 2014, *Mon. Not. R. Astron. Soc.* **438**, 573

Katz, B. and Dong, S.: 2012, preprint (arXiv:1211.4584)

Knispel, B. et al.: 2013, *Astrophys. J.* **774**, 93

Kozai, Y.: 1962, *Astron. J.* **67**, 591

Kulkarni, S., Hut, P., and McMillan, S.: 1993, *Nature* **364**, 421

Landau, L. and Lifschits, E.: 1975, *The Classical Theory of Fields*, Vol. Volume 2 of *Course of Theoretical Physics*, Pergamon Press, Oxford

Leigh, N. W. C., Geller, A. M., McKernan, B., Ford, K. E. S., Mac Low, M.-M., Bellovary, J., Haiman, Z., Lyra, W., Samsing, J., O'Dowd, M., Kocsis, B., and Endlich, S.: 2017, *Mon. Not. R. Astron. Soc.* **474(4)**, 5672

Leigh, N. W. C., Geller, A. M., and Toonen, S.: 2016, *Astrophys. J.* **818**, 21

Li, G., Naoz, S., Kocsis, B., and Loeb, A.: 2015, *Mon. Not. R. Astron. Soc.* **451**, 1341

Lidov, M. L.: 1962, *Planet. Space. Sci.* **9**, 719

Liu, B. and Lai, D.: 2017, *Astrophys. J. Lett.* **846**, L11

Liu, B. and Lai, D.: 2018, *Astrophys. J.* **863(1)**, 68

Liu, B., Lai, D., and Wang, Y.-H.: 2019, *Astrophys. J.* **883(1)**, L7

Lorentz, H. A. and Droste, J. V.: 1917, *K. Akad. Wet. Amsterdam* **26**, 392, 649

Luo, L., Katz, B., and Dong, S.: 2016, *Mon. Not. R. Astron. Soc.* **458**, 3060

Marchal, C. and Bozis, G.: 1982, *Celestial Mech.* **26**, 311

Mardling, R. A. and Aarseth, S. J.: 2001, *Mon. Not. R. Astron. Soc.* **321**, 398

Marzari, F.: 2014, *Mon. Not. R. Astron. Soc.* **442**, 1110

Marzari, F. and Weidenschilling, S. J.: 2002, *Icurus* **156**, 570

Migaszewski, C. and Goździewski, K.: 2011, *Mon. Not. R. Astron. Soc.* **411**, 565

Milani, A. and Nobili, A. M.: 1983, *Celestial Mech.* **31**, 213

Miller, M. C. and Hamilton, D. P.: 2002, *Astrophys. J.* **576**, 894

Misner, C. W., Thorne, K., and Wheeler, J.: 1973, *Gravitation*, W. H. Freeman, San Francisco

Moore, C.: 1993, *Phys. Rev. Lett.* **70**, 3675

Morbidelli, A.: 2011, *MODERN CELESTIAL MECHANICS Aspects of Solar System Dynamics*, London: Taylor & Francis

Morrison, S. J. and Kratter, K. M.: 2016, *Astrophys. J.* **823**, 118

Murray, C. D. and Dermott, S. F.: 2000, *Solar System Dynamics*, Cambridge Univ. Press

Naoz, S.: 2016, *Annual Review of Astronomy and Astrophysics* **54(1)**, 441

Naoz, S., Farr, W. M., Lithwick, Y., Rasio, F. A., and Teyssandier, J.: 2011, *Nature* **473**, 187

Naoz, S., Farr, W. M., Lithwick, Y., Rasio, F. A., and Teyssandier, J.: 2013a, *Mon. Not. R. Astron. Soc.* **431**, 2155

Naoz, S., Farr, W. M., and Rasio, F. A.: 2012, *Astrophys. J. Lett.* **754**, L36

Naoz, S., Kocsis, B., Loeb, A., and Yunes, N.: 2013b, *Astrophys. J.* **773**, 187

Naoz, S., Li, G., Zanardi, M., de Elía, G. C., and Sisto, R. P. D.: 2017, *Astron. J.* **154(1)**, 18

Nielsen, L. D. et al.: 2020, *Astron. Astrophys.* **639**, A76

Oberst, T. E. et al.: 2017, *Astron. J.* **153(3)**, 97

Okawa, H., Fujisawa, K., Yamamoto, Y., Hirai, R., Yasutake, N., Nagakura, H., and Yamada, S.: 2018, arXiv e-prints (arXiv:1809.04495)

O'Connor, C. E., Liu, B., and Lai, D.: 2020, *Monthly Notices of the Royal Astronomical Society* **501(1)**, 507

Peters, P. C.: 1964, *Phys. Rev.* **136**, B1224

Peters, P. C. and Mathews, J.: 1963, *Phys. Rev.* **131**, 435

Petrovich, C.: 2015, *Astrophys. J.* **799**, 27

Petrovich, C. and Tremaine, S.: 2016, *Astrophys. J.* **829**, 132

Poincaré, H.: 1890, *Acta Math.* **13(1-2)**, 5

Pu, B. and Wu, Y.: 2015, *Astrophys. J.* **807**, 44

Rafikov, R. R.: 2014, *Astrophys. J.* **794**, 76

Randall, L. and Xianyu, Z.-Z.: 2018, *Astrophys. J.* **864(2)**, 134

Randall, L. and Xianyu, Z.-Z.: 2019, *Astrophys. J.* **878(2)**, 75

Ransom, S. M., Stairs, I. H., Archibald, A. M., Hessels, J. W. T., Kaplan, D. L., van Kerkwijk, M. H., Boyles, J., Deller, A. T., Chatterjee, S., Schechtman-Rook, A., Berndsen, A., Lynch, R. S., Lorimer, D. R., Karako-Argaman, C., Kaspi, V. M., Kondratiev, V. I., McLaughlin, M. A., van Leeuwen, J., Rosen, R., Roberts, M. S. E., and Stovall, K.: 2014, *Nature* **505**, 520

Richardson, D. L. and Kelly, T. J.: 1988, *Celestial Mech.* **43**, 193

Roy, A. E., Walker, I. W., Carusi, A., and Valsecchi, G. B.: 1984, *Astron. Astrophys.* **141**, 25

Samsing, J., MacLeod, M., and Ramirez-Ruiz, E.: 2014, *The Astrophysical Journal* **784(1)**, 71

Sato, S. et al.: 2017, *Journal of Physics: Conference Series* **840**, 012010

Secunda, A., Bellovary, J., Low, M.-M. M., Ford, K. E. S., McKernan, B., Leigh, N. W. C., Lyra, W., and Sándor, Z.: 2019, *Astrophys. J.* **878**, 85

Seto, N.: 2012, *Phys. Rev. D* **85**, 064037

Seto, N.: 2013, *Monthly Notices of the Royal Astronomical Society* **430(1)**, 558

Shevchenko, I. I.: 2017, *The Lidov-Kozai Effect—Applications in Exoplanet Research and Dynamical Astronomy*, Springer International Publishing Switzerland

Silsbee, K. and Tremaine, S.: 2017, *Astrophys. J.* **836**, 39

Smarr, L. L. and Blandford, R.: 1976, *Astrophys. J.* **207**, 574

Smith, A. W. and Lissauer, J. J.: 2009, *Icurus* **201**, 381

Soffel, M. H.: 1989, *Relativity in Astrometry, Celestial Mechanics and Geodesy*, Springer-Verlag Berlin Heidelberg New York.

Suzuki, H., Gupta, P., Okawa, H., and Maeda, K.: 2019, *Mon. Not. R. Astron. Soc.* **486**, L52

Suzuki, H., Gupta, P., Okawa, H., and Maeda, K.: 2021, *Mon. Not. R. Astron. Soc.* **500**, 1645

Suzuki, H., Nakamura, Y., and Yamada, S.: 2020, *Phys. Rev. D* **102**, 124063

Szebehely, V.: 1967, *Theory of orbits. The restricted problem of three bodies*, Academic Press. New York.

Taylor, J. H., Hulse, R. A., Fowler, L. A., Gullahorn, G. E., and Rankin, J. M.: 1976, *Astrophys. J.* **226**, L53

Thompson, T. A.: 2011, *Astrophys. J.* **741**, 82

Trani, A. A., Fujii, M. S., and Spera, M.: 2019a, *Astrophys. J.* **875**, 42

Trani, A. A., Spera, M., Leigh, N. W. C., and Fujii, M. S.: 2019b, *Astrophys. J.* **885**, 135

VanLandingham, J. H., Miller, M. C., Hamilton, D. P., and Richardson, D. C.: 2016, *Astrophys. J.* **828**, 77

von Zeipel, H.: 1910, *Astronomische Nachrichten* **183**, 345

Wegg, C. and Bode, J. N.: 2011, *Astrophys. J. Lett.* **728**, L8

Weinberg, S.: 1972, *Gravitation and Cosmology: Principles and Applications of the General Theory of Relativity*, Wiley-VCH

Weisberg, J. M., Nice, D. J., and Taylor, J. H.: 2010, *Astrophys. J.* **772**, 1030

Weisberg, J. M. and Taylor, J. H.: 2005, *Binary Radio Pulsars ASP Conference Series* 328

Wen, L.: 2003, *Astrophys. J.* **598**, 419

Will, C. M.: 2006, *Living Rev. Relativ.* **9**, 3

Will, C. M.: 2014a, *Phys. Rev. D* **89**, 044043

Will, C. M.: 2014b, *Class. Quantum Gravity* **31**, 244001

Will, C. M.: 2017, *Phys. Rev. D* **96**, 023017

Wolszczan, A. and Frail, D.: 1992, *Nature* **355**, 145

Yamada, K. and Asada, H.: 2010, *Phys. Rev. D* **82**, 104019

Yang, H. and Casals, M.: 2017, *Phys. Rev. D* **96**, 083015

Zevin, M., Samsing, J., Rodriguez, C., Haster, C.-J., and Ramirez-Ruiz, E.: 2019, *The Astrophysical Journal* **871(1)**, 91

Zhou, J.-L., Lin, D. N. C., and Sun, Y.-S.: 2007, *Astrophys. J.* **666**, 423

Zwart, S. P., van den Heuvel, E. P. J., van Leeuwen, J., and Nelemans, G.: 2011, *Astrophys. J.* **734**, 55

早稲田大学　博士（理学）　学位申請　研究業績書

(List of research achievements for application of doctorate (Dr. of Science), Waseda University)

氏　名　　　　　鈴　木　遼　　　印

（As of December, 2020）

種 類 別 (By Type)	題名、　発表・発行掲載誌名、　発表・発行年月、　連名者（申請者含む）(theme, journal name, date & year of publication, name of authors inc. yourself)
論文	○Title: Post-Newtonian Kozai-Lidov Mechanism and its Effect on Cumulative Shift of Periastron Time of Binary Pulsar Journal: Monthly Notices of the Royal Astronomical Society, Volume 500, Issue 2, p.1645–1665 Publication date: January 2021 Authors: <u>Haruka Suzuki</u>, Priti Gupta, Hirotada Okawa, Kei-ichi Maeda ○Title: General Relativistic Effects on Hill Stability of Multi-Body Systems: Stability of Three-Body Systems Containing a Massive Black Hole Journal: Physical Review D, 102, 124063 Publication date: December 2020 Authors: <u>Haruka Suzuki</u>, Yusuke Nakamura, Shoichi Yamada Title: Gravitational Waves from Hierarchical Triple Systems with Kozai-Lidov Oscillation Journal: Physical Review D, 101, 104053 Publication date: May 2020 Authors: Priti Gupta, <u>Haruka Suzuki</u>, Hirotada Okawa, Kei-ichi Maeda, ○Title: Cumulative Shift of Periastron Time of Binary Pulsar with Kozai-Lidov Oscillation Journal: Monthly Notices of the Royal Astronomical Society: Letters, Volume 486, Issue 1, p.L52-L57 Publication date: April 2019 Authors: <u>Haruka Suzuki</u>, Priti Gupta, Hirotada Okawa, Kei-ichi Maeda
講演 （口頭）	Title: 3 体系の Hill 安定性に対する一般相対論的効果の影響 Conference: 第 33 回理論懇シンポジウム，D11 講演 Place: オンライン開催 Date: 2020 年 12 月 Authors: <u>鈴木遼</u>，中村友祐，山田章一 Title: General Relativistic Effects on Hill Stability of three-body systems Conference: The Evolution of Massive Stars and Formation of Compact Stars: from the Cradle to the Grave Place: 早稲田大学 Date: 2020 年 2 月 Authors: <u>Haruka Suzuki</u>, Yusuke Nakamura, Shoichi Yamada Title: 多体系の Hill 安定性に対する一般相対論的効果の影響 Conference: 日本物理学会 第 75 回年次大会 17pT21-1 講演 Place: 山形大学 Date: 2019 年 9 月 Authors: <u>鈴木遼</u>，山田章一

早稲田大学　博士（理学）　学位申請　研究業績書
(List of research achievements for application of doctorate (Dr. of Science), Waseda University)

種 類 別 By Type	題名、　　発表・発行掲載誌名、　　発表・発行年月、　　連名者（申請者含む）(theme, journal name, date & year of publication, name of authors inc. yourself)
	Title: GR effect on Hill Stability Conference: 22nd International Conference on General Relativity and Gravitation, Valencia, B1 Wednesday 2 Place: Valencia, Spain Date: July 2019 Authors: <u>Haruka Suzuki</u>, Shoichi Yamada Title: Cumulative Shift of Periastron Time of Binary Pulsar with Kozai-Lidov Oscillation Conference: 天体力学 N 体力学研究会(2019) Place: 北里大学 Date: 2019 年 7 月 Authors: <u>Haruka Suzuki</u>, Priti Gupta, Hirotada Okawa, Kei-ichi Maeda Title: 重力波放出に伴う連星中性子星周期減衰に対する古在機構の効果 Conference: 日本物理学会 第 74 回年次大会, 16pK407-12 講演 Place: 九州大学 Date: 2019 年 3 月 Authors: <u>鈴木遼</u>, Priti Gupta, 大川博督, 前田恵一 Title: The Effect of Kozai-Lidov Mechanism on the Period Shift of the Binary Neutron Stars by Gravitational Waves Conference: The 28th Workshop on General Relativity and Gravitation in Japan - JGRG28, T4, Place: 立教大学 Date: 2018 年 11 月 Authors: <u>Haruka Suzuki</u>, Priti Gupta, Hirotada Okawa, Kei-ichi Maeda Title: コンパクト天体を含む 4 体系の相対論的軌道安定性 Conference: 日本天文学会 2017 年秋季年会，W144a 講演， Place: 北海道大学 Date: 2017 年 9 月 Authors: <u>鈴木遼</u>，中村友祐，山田章一 Title: コンパクト天体を含む 4 体系の相対論的軌道安定性 Conference: 第 47 回天文・天体物理若手夏の学校，コン a3 講演 Place: 長野 Date: 2017 年 7 月 Authors: <u>鈴木遼</u>，中村友祐，山田章一 Title: コンパクト天体を含む 3 体系及び 4 体系の軌道長期安定性の解析 Conference: 日本天文学会 2017 年春季年会，W143a 講演， Place: 九州大学 Date: 2017 年 3 月 Authors: <u>鈴木遼</u>，中村友祐，山田章一

早稲田大学　博士（理学）　学位申請　研究業績書

(List of research achievements for application of doctorate (Dr. of Science), Waseda University)

種 類 別 By Type	題名、　　発表・発行掲載誌名、　　発表・発行年月、　　連名者（申請者含む）(theme, journal name, date & year of publication, name of authors inc. yourself)
講演 （ポスター）	Title: パルサーを中心とする少数多体系の相対論的軌道長期安定性 Conference: 第 46 回天文・天体物理若手夏の学校，コン a11 講演 Place: 長野 Date: 2016 年 7 月 Authors: <u>鈴木遼</u>，中村友祐，山田章一 Title: コンパクト天体を含む 4 体系の軌道安定性における相対論的効果 Conference: 第 49 回天文・天体物理若手夏の学校，コン b4 講演 Place: 愛知 Date: 2019 年 7 月 Authors: <u>鈴木遼</u>，中村友祐，山田章一， Title: 重力波放出に伴う連星中性子星周期減衰に対する古在機構の効果 Conference: 第 31 回理論懇シンポジウム，P36 講演 Place: 京都大学 Date: 2018 年 12 月 Authors: <u>鈴木遼</u>, Priti Gupta, 大川博督，前田恵一 Title: コンパクト天体を含む 4 体系の軌道安定性における相対論的効果 Conference: 第 48 回天文・天体物理若手夏の学校，コン c12 講演 Place: 愛知 Date: 2018 年 7 月 Authors: <u>鈴木遼</u>，中村友祐，山田章一 Title: Post-Newtonian Effects on the Orbital Stability of Four-Body Systems Containing Compact Objects Conference: 2018 SNe Workshop『Physics of Core-Collapse Supernovae and Compact Star Formations』, P15 Place: 早稲田大学 Date: 2018 年 3 月 Authors: <u>Haruka Suzuki</u>, Yusuke Nakamura, Shoichi Yamada Title: Post-Newtonian Effects on the Orbital Stability of Four-Body Systems Containing Compact Objects Conference: 天体力学 N 体力学研究会(2018) Place: 国立天文台 Date: 2018 年 3 月 Authors: <u>Haruka Suzuki</u>, Yusuke Nakamura, Shoichi Yamada